An Experimental Investigation Of Chemically-Reacting, Gas-Phase Turbulent Jets

Thesis by

Richard Joseph Gilbrech

In Partial Fulfillment of the Requirements

for the Degree of

Doctor of Philosophy

California Institute of Technology

Pasadena, California

1991

(submitted April 12, 1991)

Acknowledgements

This work was made possible through the support, guidance, and encouragement of many people. Chief among these was my advisor, Professor Paul Dimotakis, who provided scientific direction when needed, valuable suggestions, and much support throughout my graduate studies. Dr. J. E. Broadwell and Professor E. E. Zukoski also provided many useful discussions.

I would like to thank all the people who were involved in the design, construction, and operation of the High Pressure Combustion Facility. Among these were Dr. Godfrey Mungal who provided the initial design of the High Pressure Reactant Vessel; Dr. Dan Lang for providing his computer and electronics expertise with the data acquisition system and the the amplifier circuits; Cliff Frieler, David Dowling, Dr. Richard Miake-Lye, Jeff Hall, Paul Miller, and Dr. Henning Rosemann for their many helpful ideas in the experimental design and many fruitful scientific discussions. From the technical staff at GALCIT, I want to thank Earl Dahl for his invaluable help in constructing and operating the facility, George Lundgren and Phil Wood of the Aeronautics Machine Shop, Clarence Hemphill for his help in the electrical wiring of the facility, Harry Hamaguchi for his photographic work, and Betty Wood for her technical drawings. From Central Engineering Services, Lou Johnson and Norm Keidel provided many design ideas and their skilled machinists and Ralph Ortega (an exceptional welder) fabricated many of the parts for the facility.

Additionally, I would like to acknowledge the California Institute of Technology for both personal financial support and for funding the laboratory building exten-

sion. This work was jointly funded by the Gas Research Institute through Contracts No. 5083–260–0878 and No. 5087–260–1467, and the Air Force Office of Scientific Research through Grants No. 83–0213 and No. 88–0155.

I would also like to thank all the friends I've made here who gave much needed encouragement and support. Many thanks to Supper Club for providing weekly diversions. I especially want to thank my wonderful wife, Shelly, for her patience and support and my son, Ryan, for many happy moments. Finally, I want to thank God for seeing me through this difficult task.

Abstract

A new high pressure combustion facility was built to investigate mixing in axisymmetric, turbulent jets exiting into quiescent reservoirs. The facility uses fluorine and nitric oxide, diluted with nitrogen, for chemical product formation that is accompanied by heat release. The average temperature was measured by a set of long, thin, resistance wire thermometers stretched across the jet centerline at 16 downstream locations from $x/d_0 = 30$ to 240. Runs at several stoichiometric mixture ratios ϕ, for Reynolds numbers ranging from $10,000 \leq Re \leq 150,000$, were performed to determine any dependence of flame length on Reynolds number. The Reynolds number was varied through density, *i.e.*, pressure, while the jet exit velocity and exit diameter were held constant. The time-averaged line integral of temperature, measured along the transverse axis of the jet by the wires, displays a logarithmic dependence on x/d^* within the flame zone, and asymptotes to a constant value beyond the flame tip, as predicted from scaling and similarity arguments for a momentum-dominated, turbulent jet. The main result of the work is that the flame length, as estimated from the temperature measurements, varies with changes in Reynolds number, suggesting that the mixing process is not Reynolds number independent up to $Re = 150,000$. Specifically, the normalized flame length L_f/d^* displays a linear dependence on ϕ, with a slope that decreases from $Re = 10,000$ to 20,000, and then remains constant for $Re > 20,000$. Additionally, the measurements revealed a "mixing virtual origin," defined as the far-field flame length extrapolated to $\phi = 0$, that increases with increasing Re for $Re \leq 20,000$ and then decreases with increasing Re for $Re > 20,000$. A separate set of experiments indicated that the runs described above were momentum dominated to the farthest measuring station and that the kinetics of the chemical reactions were fast compared to the characteristic mixing time. The transition of the jet flow from a momentum-dominated to a buoyancy-dominated regime was identified in another set of experiments.

Table of Contents

List of Figures

List of Tables

List of Symbols

English

A	slope of the L_f/d^* versus ϕ curve, Eq. 4.3
c_w	specific heat of the cold wire
C	molar reactant concentration
d_0	nozzle exit diameter
d^*	jet nozzle momentum diameter, Eq. 2.1
d_w	cold wire diameter
D	species diffusivity
Da	Dahmköhler number, Eq. 4.19
f	fuel mass fraction
g	mean temperature profile function, Eqs. 3.2a and 4.4; acceleration of gravity
HPCF	High Pressure Combustion Facility
HPRV	High Pressure Reactant Vessel
I	constant current through the cold wire
J_0	jet nozzle exit momentum flux, Eq. 4.7
k	chemical reaction rate constant
k_g	thermal conductivity of the gas
L_f	average flame length
L_{f_o}	average flame length evaluated from the curve fits of Fig. 4.6
L_w	length of the cold wire
L_0	mixing virtual origin, defined as the far field flame length extrapolated to $\phi = 0$
m_i	mass of the i^{th} species
$\dot{m}_0$	jet nozzle exit mass flux
N	total number of species in a gas mixture
Nu	Nusselt number

o	oxidizer mass fraction
p	run pressure or jet pressure
p_∞	reservoir pressure
PDF	Probability Density Function
ΔQ	molar heat of reaction
R	cold wire hot resistance
R_0	cold wire cold resistance
R_u	universal gas constant
Re	Reynolds number of the jet, Eq. 1.1
Ri	Richardson number, Eq. 4.10
Ri_s	source flame-zone Richardson number, Eq. 4.12
Sc	Schmidt number, ν/D, ratio of kinematic viscosity to species diffusivity
t	time
$T(x,y)$	local temperature in the jet at (x,y)
T_g	gas temperature
T_0	jet exit gas temperature
T_∞	reservoir gas temperature
ΔT	cold wire temperature change
ΔT_f	adiabatic flame temperature, defined as the temperature rise achieved if all reactants burn to completion, adiabatically, at constant pressure
$\Delta T(x,y)$	$T(x,y) - T_\infty$, temperature rise in the jet at (x,y)
U_0	nozzle exit velocity
U_cl	jet average centerline velocity, Eq. 4.22
U_r	recirculation velocity
U_s	source velocity, Eq. 4.13
v'	instantaneous transverse velocity fluctuation
V	volume of the cold wire element
ΔV	cold wire voltage change

x	streamwise axial distance from the nozzle exit
x_0	virtual origin of the jet
x_t	value of x where the transition to buoyancy-dominated flow occurs
y	transverse distance from the jet centerline
Y_i	mass fraction of the i^{th} species, Eq. 4.2

Greek

α	cold wire temperature coefficient of resistance, Eq. 3.1
β	mean jet scalar decay constant, Eq. 4.4
$\delta(x)$	local jet diameter, Eq. 4.21
δ_P	product thickness, Eq. 3.5
η	normalized transverse coordinate, Eq. 3.2b
κ	mean jet scalar decay constant, Eq. 3.2a
μ_∞	reservoir fluid dynamic viscosity
ν	kinematic viscosity
ξ	non-dimensional streamwise buoyancy coordinate, Eq. 4.14a
ξ_t	value of ξ where the transition to buoyancy-dominated flow occurs
ρ_0	jet nozzle gas density
ρ_∞	reservoir gas density
$\overline{\rho}(x)$	mean flame density, averaged over the jet cone up to x
ρ_w	cold wire density
$\overline{\Delta\rho}$	$\rho_\infty - \overline{\rho}$, average density change due to heat release
τ_c	chemical reaction time
τ_δ	large-scale passage time, Eq. 4.20
τ_w	time constant of the cold wire
ϕ	stoichiometric mixture ratio, Eq. 4.1b

Other Symbols

$( )_{st}$	stoichiometric conditions
$( )_t$	transition to buoyancy-dominated flow
$( )_w$	cold wire property
$( )_\infty$	reservoir conditions

CHAPTER 1

Introduction

1.1 Background

The momentum-dominated, free turbulent jet is a classical shear flow that has been experimentally investigated by many researchers (*e.g.*, Ruden 1933; Kuthe 1935; Hawthorne *et al.* 1948; Hottel 1953; Thring & Newby 1953; Ricou & Spalding 1961; Wilson & Danckwerts 1964; Becker *et al.* 1967; Wygnanski & Fiedler 1969; Townsend 1976; Birch *et al.* 1978; Becker & Yamazaki 1978; Lockwood & Moneib 1980; Chen & Rodi 1980; Dahm & Dimotakis 1987, 1990; Dowling & Dimotakis 1990; Miller & Dimotakis 1991). Although it is perhaps one of the simplest of flow geometries, understanding the associated entrainment and mixing processes has been an ongoing effort that is still challenging both the experimentalist and the theorist.

In the context of combustion systems, such as in furnaces, gas turbine engines, and rocket engines, it is often desirable to have the mixing and combustion processes occur simultaneously rather than sequentially. The turbulent jet has seen widespread use in such systems, providing a practical and efficient means of mixing fuel and oxidizer in the combustion chamber. Much of the research in jet mixing has been motivated by the combustion community in the hope of finding faster, more efficient ways of mixing reactants to provide more useful energy per unit fuel and to reduce certain undesirable exhaust products through a better controlled combustion process (*e.g.*, NO_x in high temperature flames).

A common practice in dealing with turbulent flows has been to assume that above a suitably high Reynolds number, the properties of the flow become independent of Reynolds number. This assumption often extends to mixing and has led researchers to investigate turbulent flows in the laboratory at much lower Reynolds numbers than those of the actual devices utilizing the flow. The assumption, or hope, has been that the experiment accurately captures the flow dynamics of the practical device, even though the length scales, velocity, and fluid properties could be very different.

Recent experimental evidence has motivated a closer look into the assumption of Reynolds number independence. Mungal *et al.* (1985) found that the amount of product formation in a chemically reacting, two-dimensional shear layer decreased as Reynolds number increased. In their experiment, product formation was assumed to be equivalent to molecular mixing, and therefore, the amount of molecularly-mixed fluid changed with Reynolds number. For the current jet experiments, a measurable quantity that could be related to molecular mixing was desired. Flame length L_f has been shown to be related to the rate of molecular mixing in the jet (*e.g.*, Broadwell 1982) and can be measured experimentally. Therefore, L_f, considered to be the axial distance required to molecularly mix every part of jet fluid with reservoir fluid to at least the stoichiometric mixture ratio ϕ, was chosen as the quantity to measure in the current experiments.

1.2 Current experiments

The goal of the present research was to design and construct a High Pressure Combustion Facility (HPCF) and to conduct experiments in this facility to measure average flame lengths in an axisymmetric jet over a wide range of Reynolds numbers. It should be noted that there are several methods for measuring average flame lengths, as will be outlined in Ch. 3. The particular method for determining L_f in these experiments was chosen not because it is the definitive one but because it can accurately identify potentially small changes in L_f over the large Reynolds number range investigated. That is, we are primarily interested in determining if the flame lengths change with Reynolds number. If there were no Reynolds number effects, as conventional wisdom would proclaim, we would expect a null result, *i.e.*, all the measurements should collapse on a single curve for the entire Reynolds number range investigated.

The jet coordinate system is shown in Fig. 1.1. The Reynolds number of the jet is defined as

$$Re \equiv \frac{\rho_\infty U_0 d_0}{\mu_\infty} \ , \tag{1.1}$$

where ρ_∞ is the reservoir gas density, U_0 is the jet exit mass flux velocity (equal to the exit velocity for the current nozzle), d_0 is the nozzle exit diameter, and μ_∞ is the reservoir gas dynamic viscosity.

In an effort to isolate Reynolds number effects from other effects (buoyancy, kinetics, *etc.*), the jet experiment is enclosed in a pressure vessel. Since μ_∞ is essentially only a function of temperature (*e.g.*, Thompson 1984), the jet Reynolds number can be varied by changing the reservoir gas density, which is directly proportional to the reservoir pressure. In this way, the nozzle exit diameter and exit velocity can be held fixed, with the jet in a momentum-dominated regime, while the Reynolds number is varied via pressure.

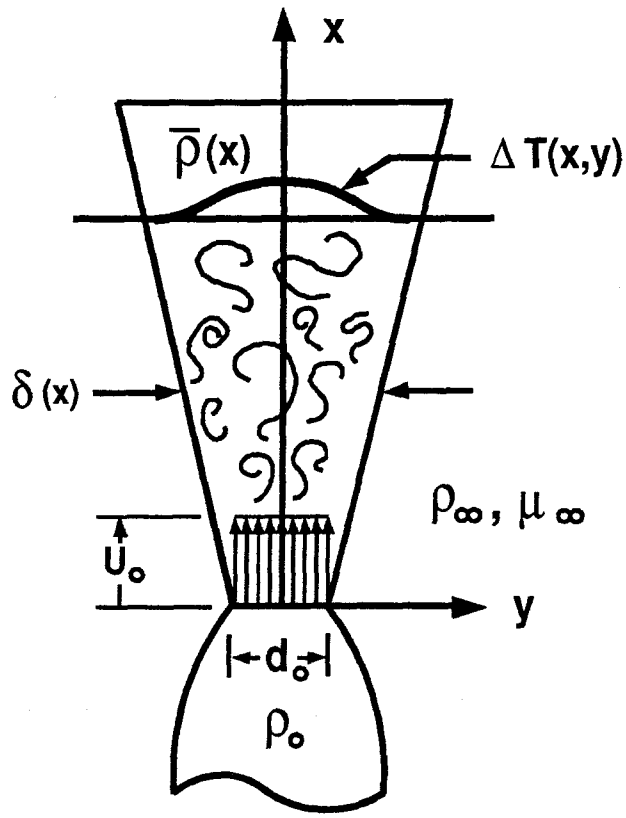

FIG. 1.1 Schematic of the jet coordinate system.

The facility is designed to span 2.2 decades of pressure, providing a large range of Reynolds numbers for investigation. Buoyancy effects scale as

$$\frac{\overline{\Delta\rho}(x)}{\rho_0} = \frac{\rho_\infty - \overline{\rho}(x)}{\rho_0} , \tag{1.2}$$

where $\overline{\Delta\rho}(x)$ is the average change in density owing to heat release, ρ_0 is the jet exit density, and $\overline{\rho}(x)$ is the average density of the jet cone up to that x location. These effects remain constant as the pressure is varied, because both $\overline{\Delta\rho}$ and ρ_0 are linearly proportional to the pressure. The chemical kinetic rate is proportional to molecular number density and, therefore, for a given concentration of reactants, the chemical reaction rate gets faster as pressure (Re) is increased.

Combustion can only occur when fuel and oxidizer mix at the molecular level. Therefore, it is of interest in the present experiments to distinguish molecularly-mixed fluid from pure jet and reservoir fluid. This is done with the chemical reaction method that was used in water (acid-base reaction) by Weddell (in Hottel 1953), Brown & Dimotakis (1976), Breidenthal (1981), Dahm *et al.* (1984), and Koochesfahani & Dimotakis (1986), and in gases by Mungal & Dimotakis (1984), Hermanson & Dimotakis (1989), and Frieler & Dimotakis (1988). See Dimotakis (1989) for a review of these experiments. The method relies on molecular mixing to form a chemical product that can be detected on a macroscopic scale, *e.g.*, heat release or temperature rise. For the present experiments, the reactions are exothermic, which means that chemical product formation is accompanied by heat release. If the adiabatic flame temperature rise ΔT_f is kept low enough, then the heat release can be expected to have little effect on the flow dynamics. The adiabatic flame temperature rise ΔT_f is defined as the temperature rise achieved if all reactants burn to completion, adiabatically, at constant pressure. For a fast chemical reaction, *i.e.*, one in which the time lag between molecular mixing and product formation is negligible, there is a one-to-one correspondence between product formation and molecular mixing. In this way, the heat release is a tracer for molecularly-mixed fluid.

The advantages of the F_2/NO chemical system (described in Mungal & Dimotakis 1984) made it a logical choice for the current experiments. This chemical system is completely hypergolic, *i.e.*, the reactants burn on contact since they cannot coexist at the molecular level. This obviates the need for an ignition source, flameholders, or other flow disturbing devices. Unlike hydrocarbon reactions involving hundreds of complicated reactions, the simple F_2/NO chemistry involves only three intermediate reactions, allowing the chemical kinetics and the fluid mechanics to remain tractable. The high kinetic rate of this system ensures that the rate of product formation is limited by the turbulent mixing process and not by the

chemical kinetics. This system also has the capability of producing very low adiabatic flame temperatures while maintaining fast chemistry. This is desirable in the design of the diagnostics, for the reduction of buoyancy effects, and in eliminating the influence of finite kinetic rate effects.

The F_2/NO chemistry that was employed in this experiment can be described by the "effective" reaction:

$$2\,NO + F_2 \rightarrow 2\,NOF\,, \qquad \Delta Q = -75\,\frac{\text{kcal}}{\text{mole}\,F_2}\,. \tag{1.3}$$

The reaction actually consists of two chain reactions with different rates and heats of reaction, as described in Sec. 4.3. The reactants provide a wide range of heat release while retaining an overall reaction rate in the turbulent jet that is kinetically fast even at the lower concentrations.

1.3 Outline

Constant current resistance thermometers were used to measure the average heat release in a steady, axisymmetric, chemically-reacting, gas-phase, momentum-dominated jet discharging into a quiescent reservoir. The measurements span the downstream range from 30 to 240 jet exit diameters, at Reynolds numbers from 10,000 to 150,000. Experiments at several stoichiometric mixture ratios ϕ were performed at each Reynolds number to identify possible Reynolds number effects on flame length. Chapter 2 describes the experimental facility and Ch. 3 describes the measurement technique. The experimental results are discussed in Ch. 4, which covers the effects of Reynolds number on flame length and addresses the issues of buoyancy and chemical kinetic rate.

CHAPTER 2

Experimental Facility

2.1 The main apparatus

These experiments were conducted in the newly constructed High Pressure Combustion Facility (HPCF), shown schematically in Fig. 2.1 and pictured in Fig. 2.2. This blowdown facility was designed to study turbulent, reacting jets at both reduced and elevated pressures. In addition to the capability of using conventional gaseous fuels, the facility was designed to handle more exotic reactants like fluorine, nitric oxide, and hydrogen. Designing a facility to safely use these exotic gases presented many unique problems. Fluorine is a highly reactive and toxic gas that requires special handling techniques. Much of the gas delivery design was based on the work of Mungal (1983). Since the current experiments involved higher concentrations and pressures of these gases than used by Mungal, fluorine compatability tests at high pressure and high concentration were performed. These materials tests were conducted with the help of TRW at their facility in Redondo Beach.

The main apparatus is the High Pressure Reactant Vessel (HPRV), designed by Godfrey Mungal in collaboration with Paul Dimotakis. The HPRV is a 107 cm (42 in.) internal diameter by 183 cm (72 in.) length pressure vessel with an interior volume of 1.43 m^3 (50.5 ft^3). The HPRV, shown in Fig. 2.3, is capable of operating at pressures from 0.1 atm to 15 atm and is internally coated with pinhole-free PFA teflon for corrosion resistance. The vessel consists of a shell with removable heads

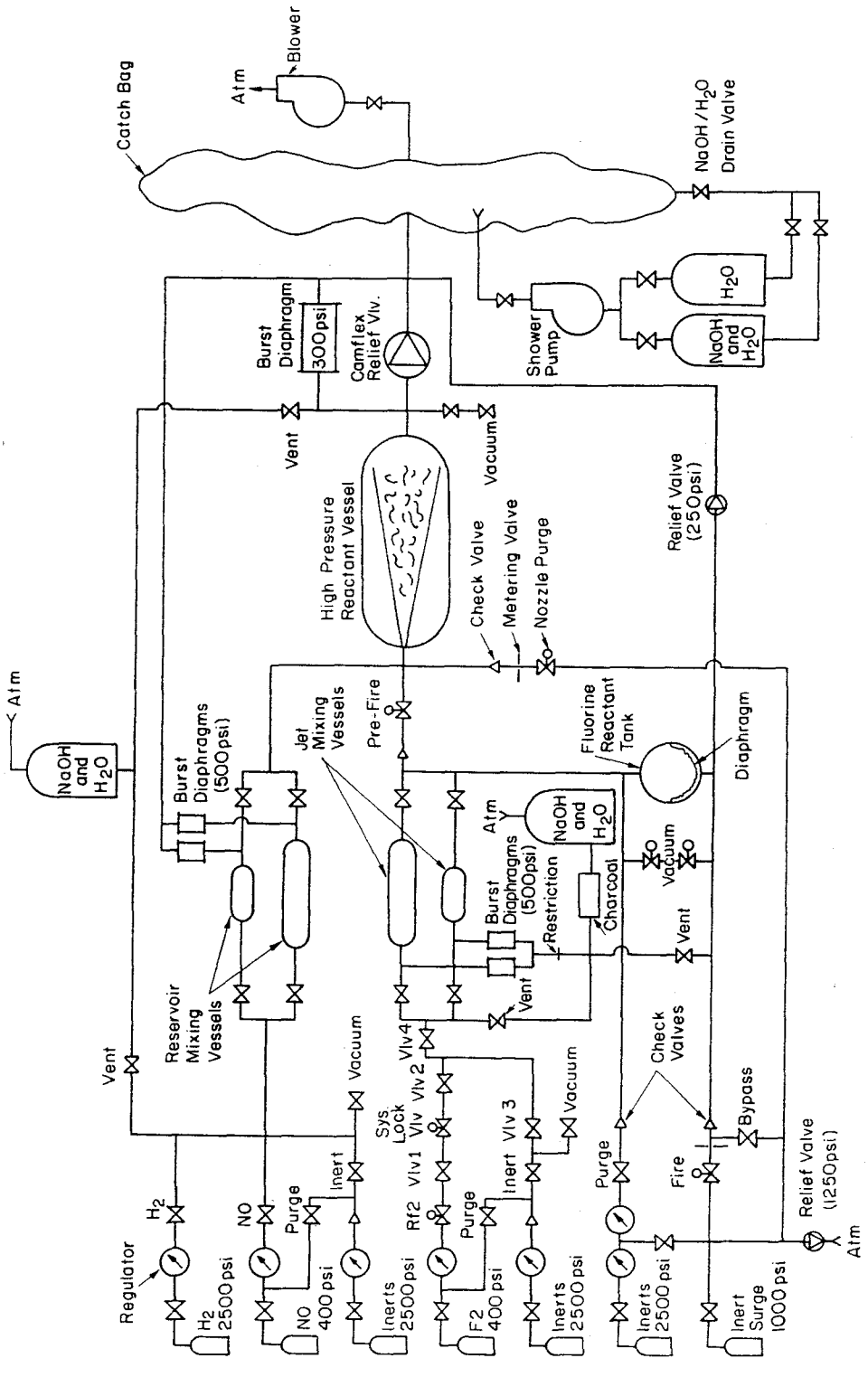

FIG. 2.1 Schematic of the High Pressure Combustion Facility.

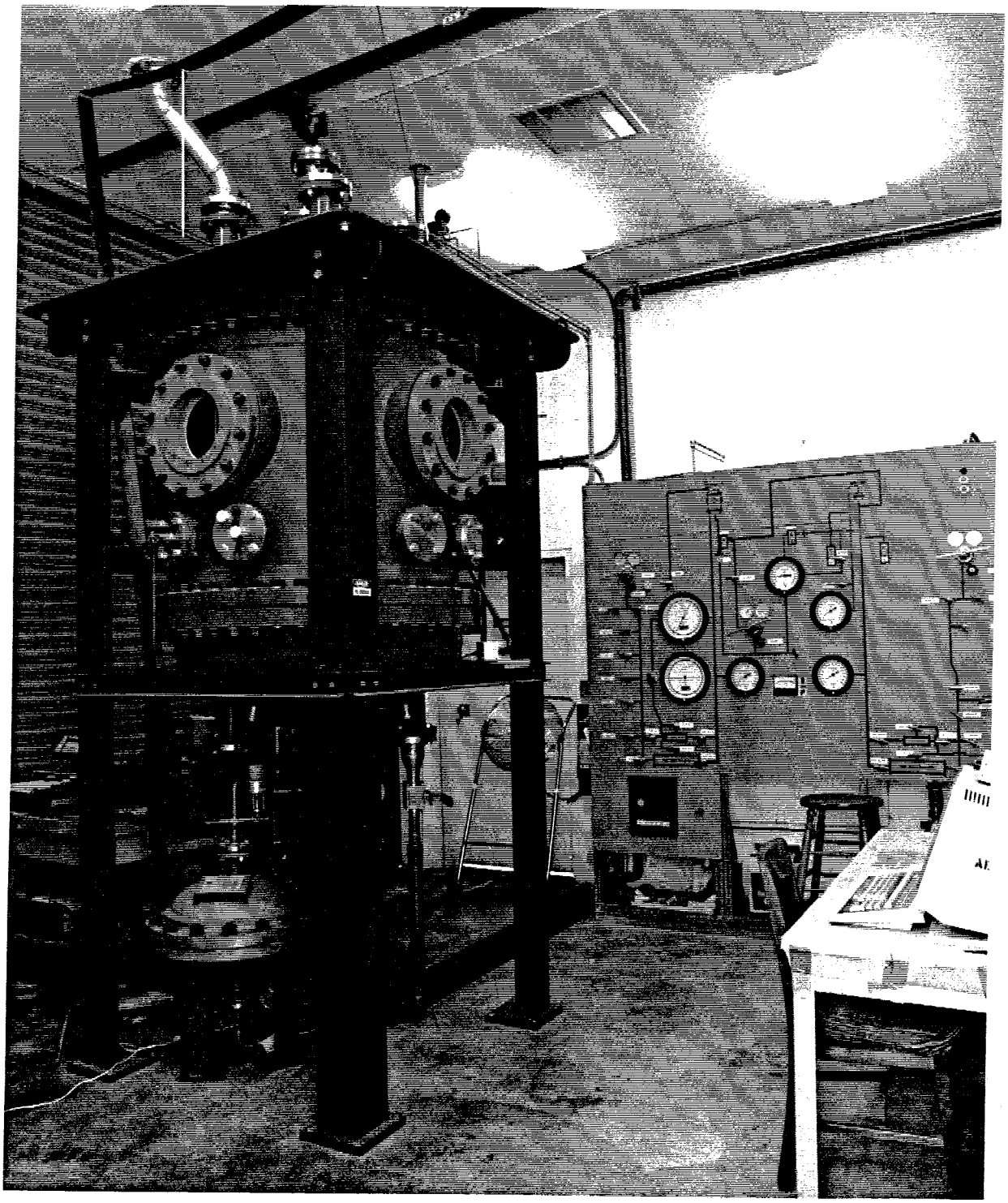

FIG. 2.2 Photograph of the High Pressure Combustion Facility. The HPRV is in the upper left foreground, with the fluorine reactant tank directly beneath it. The control panel used for loading the jet and reservoir gases is in the right background, and the computer terminal used for data acquisition and run sequencing is in the right foreground.

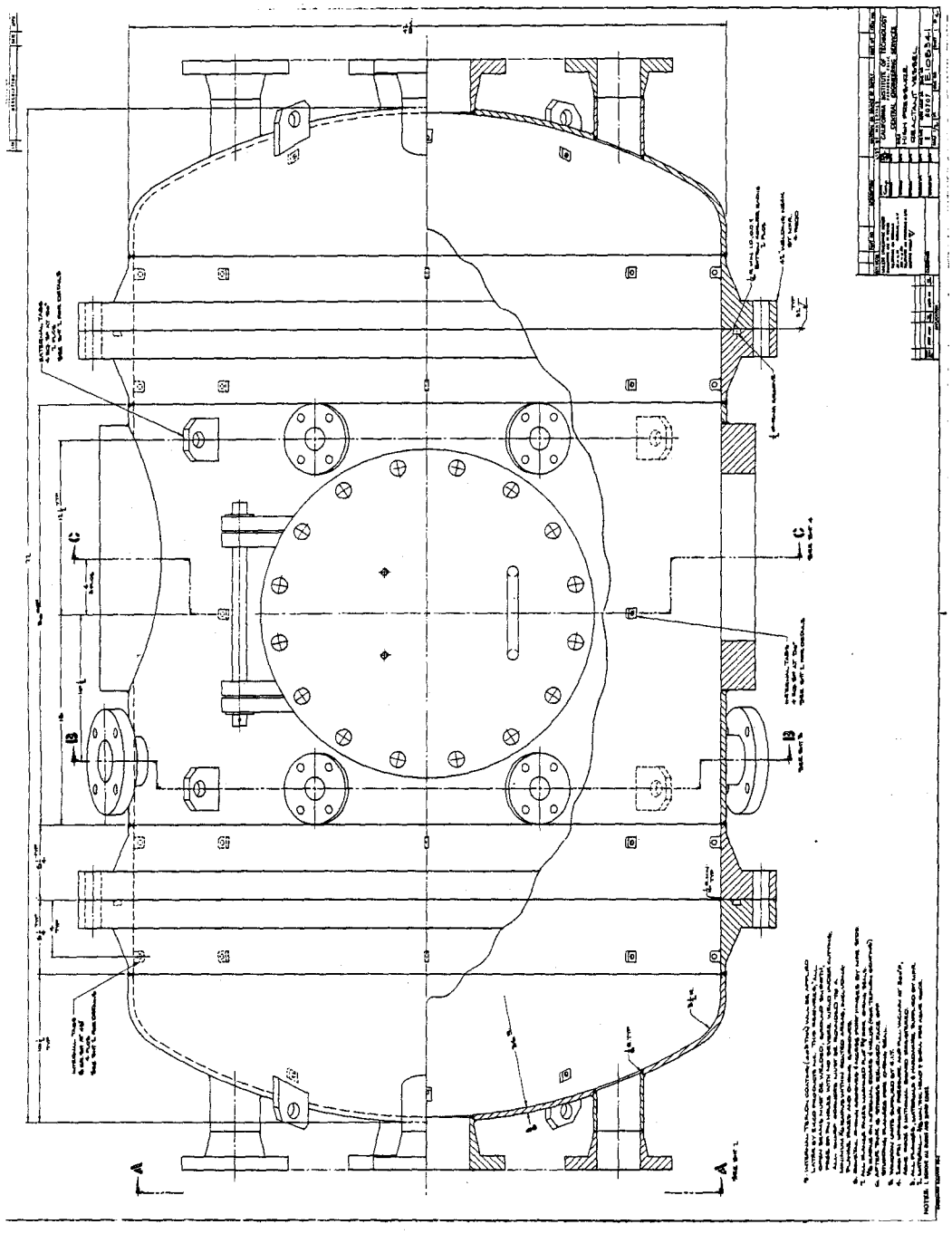

FIG. 2.3 High Pressure Reactant Vessel schematic. Height = 183 cm (6 ft), internal diameter = 107 cm (3.5 ft).

at each end for full interior access. The heads contain four 7.62 cm (3 in.) flanges for possible coflow and one 15.24 cm (6 in.) flange for jet nozzles or exhaust/optical access. The shell contains six 7.62 cm (3 in.), diametrically opposed flanges for possible line-of-sight absorption or ignition capabilities, four 3.81 cm (1.5 in.) flanges, and one 40.64 cm (16 in.) manhole for internal access. Optical access is via three 25.4 cm (10 in.) diameter by 6.35 cm (2.5 in.) thick pyrex windows held in specially designed, teflon-coated window units manufactured by Pressure Products. The tank specifications are given in Appendix A.

2.2 The gas delivery system

The reservoir (HPRV) is typically loaded to the desired concentration of NO, in a N_2 diluent, via intermediate mixing vessels of known volume, utilizing partial pressure techniques. The jet gas is contained in a fluorine reactant tank with an internal teflon expulsion diaphragm separating the jet charge from the inert driver gas. A given concentration of F_2 in a N_2 diluent is loaded into the reactant tank using the partial pressure technique. Accuracy with the NO and F_2 loading is maintained over the large range of pressures and concentrations by staging the mixing vessels, *i.e.*, a small volume vessel is used for sub-atmospheric conditions and a larger volume vessel is used for atmospheric and high pressure runs. The driver side of the expulsion diaphragm is connected to a nitrogen surge tank, comprised of four size 1A cylinders for a combined internal volume of $0.176\,m^3$ ($6.2\,ft^3$) of driver gas. The surge tank is pressurized (typically 35 atm) to provide a nearly constant stagnation pressure to three parallel sonic metering valves of various flow rates. The metered sonic N_2 stream supplies a fixed mass flow rate to the driver side of the expulsion diaphragm, resulting in a constant mass flow rate of jet gas through the nozzle in the HPRV.

The jet issues from the bottom of the HPRV upwards through a 2.54 mm (0.1 in.) exit diameter, anodized aluminum nozzle. The nozzle contraction section is described by a 6^{th} order polynomial, optimized to avoid Taylor-Görtler vortices in the concave parts and for minimum exit boundary layer thickness. The nozzle design method was developed by Dimotakis and is described in Dowling (1988). A turbulence management section is located upstream of the contraction section. This consists of a 3.81 cm (1.5 in.) diameter by 5.08 cm (2 in.) length of 0.318 cm (0.125 in.) core stainless steel honeycomb, followed by four stainless steel screens of mesh sizes from 15 to 100 wires per inch. This results in an exit turbulence level measured to be less than 0.3% over the velocity range investigated. The dynamic pressure is set prior to a run and monitored during the run with a Barocel differential pressure transducer connected across the nozzle plenum and the nozzle exit. The nozzle is mounted on a stainless steel base plate with three adjusting screws to provide angular alignment. The nozzle geometric axis was aligned once with a laser to within a few tenths of a degree of the geometric centerline of the HPRV and secured to prevent any subsequent movement. Upon periodic inspections, the nozzle alignment was found to remain unchanged.

The momentum diameter of the jet d^*, rather than the nozzle exit diameter d_0, is used to normalize the downstream coordinate x. It is defined by

$$d^* \equiv \frac{2\,\dot{m}_0}{\sqrt{\pi \rho_\infty J_0}} \quad , \tag{2.1}$$

where $\dot{m}_0$ is the nozzle exit mass flux, ρ_∞ is the density of the reservoir fluid, and J_0 is the nozzle exit momentum flux. This definition was introduced in a limited way by Thring & Newby (1953), used by Avery & Faeth (1974), and modified to its present form by Dahm & Dimotakis (1987). The momentum diameter can be used to collapse the results of many different jet experiments (see Dahm & Dimotakis 1987) and is considered to be the proper length scale for normalizing the downstream distance in the jet. The factor of 2 and the $\sqrt{\pi}$ in Eq. 2.1 were chosen so that d^*

reduces to the nozzle exit diameter d_0 for density-matched jet and reservoir fluids and a perfect "top-hat" exit velocity profile. Using the jet and reservoir mixture densities and assuming a uniform exit density profile, an axisymmetric Thwaites calculation was used to estimate the boundary layer corrections to the velocity profile at each run condition. For the experiments of Sec. 4.1, the calculations give $d^* = 0.960\, d_0$ for the $Re = 10,000$ runs and $d^* = 0.991\, d_0$ for the $Re = 150,000$ runs.

It is also common practice to allow for a virtual origin x_0 in defining the effective downstream coordinate x. The virtual origin is determined by the far-field behavior of the jet and is a correction for the influence of the near field of the jet. The external shape of the nozzle, the jet exit turbulence level, and the exit velocity profile are a few parameters that affect x_0. Dowling (1988) found a virtual origin of $x_0 = 0.5\, d_0$ for his nozzle at $Re = 16,000$. The virtual origin for the current nozzle was not measured. However, since the nozzle was designed with the same method as Dowling's, and operates at $Re \geq 10,000$, x_0 is assumed to be comparable, *i.e.*, $x_0 \sim O(d_0)$. It is therefore considered negligible and will be ignored throughout this study.

2.3 The pressure relief and exhaust systems

The facility operates in a blowdown mode under constant pressure conditions. Pressure relief for the HPRV is provided by a 3.81 cm (1.5 in.) Camflex relief valve equipped with a Taylor Microscan 500 Controller. The Controller uses a feedback control system that monitors the pressure in the HPRV, compares it to a set-point pressure, and opens the Camflex in a preprogrammed manner to maintain the set-point pressure. The Camflex is used only for run pressures $\geq$ 1 atm, while for sub-atmospheric runs, the Camflex remains shut and an acceptable pressure rise occurs in the HPRV. The exhaust from the Camflex is plumbed into a downstream

catch bag that is shared with the HF Shear Layer Combustion Facility. The catch bag (described in Hall 1991) is equipped with NaOH and water showers to neutralize the exhaust products.

No commercially available pressure transducer had the dynamic range to sense the pressure rise in the HPRV over the entire relief range (1 atm to 15 atm) with the resolution required. It was therefore necessary to create a "sliding" pressure measurement that had very high resolution over a small dynamic range, but whose range could be centered anywhere within the operating pressure of the HPRV. This was achieved by storing the HPRV starting pressure in a thermally-insulated volume that was large compared to the internal volume of a Barocel differential pressure transducer. This volume was ported to one side of the differential transducer and isolated via a valve before the run began. The other side of the transducer was connected to the HPRV resulting in a highly accurate (0.006 psi resolution) pressure measurement that could "slide" anywhere within the pressure range of the HPRV. This arrangement performed well, with the Camflex providing constant pressure in the HPRV to within 0.5%, or better, of the run pressures investigated (1 atm to 15 atm).

2.4 Diagnostics

The diagnostics utilized in these experiments were designed to give an accurate measure of average flame length. Temperature measurements were performed with a set of 16 long cold wires operated as constant current resistance thermometers. Each wire consists of a 25 μm (0.001 in.) diameter by 57.8 cm (22.75 in.) length of Pt-10%Rh wire welded to a pair of 356 μm (0.014 in.) diameter by 5 cm (2 in.) long inconel prongs. Platinum was chosen for its high coefficient of resistivity and rhodium was chosen to increase the strength. The prongs serve as cantilever springs to maintain tension in the wires and also to provide the electrical connection to the

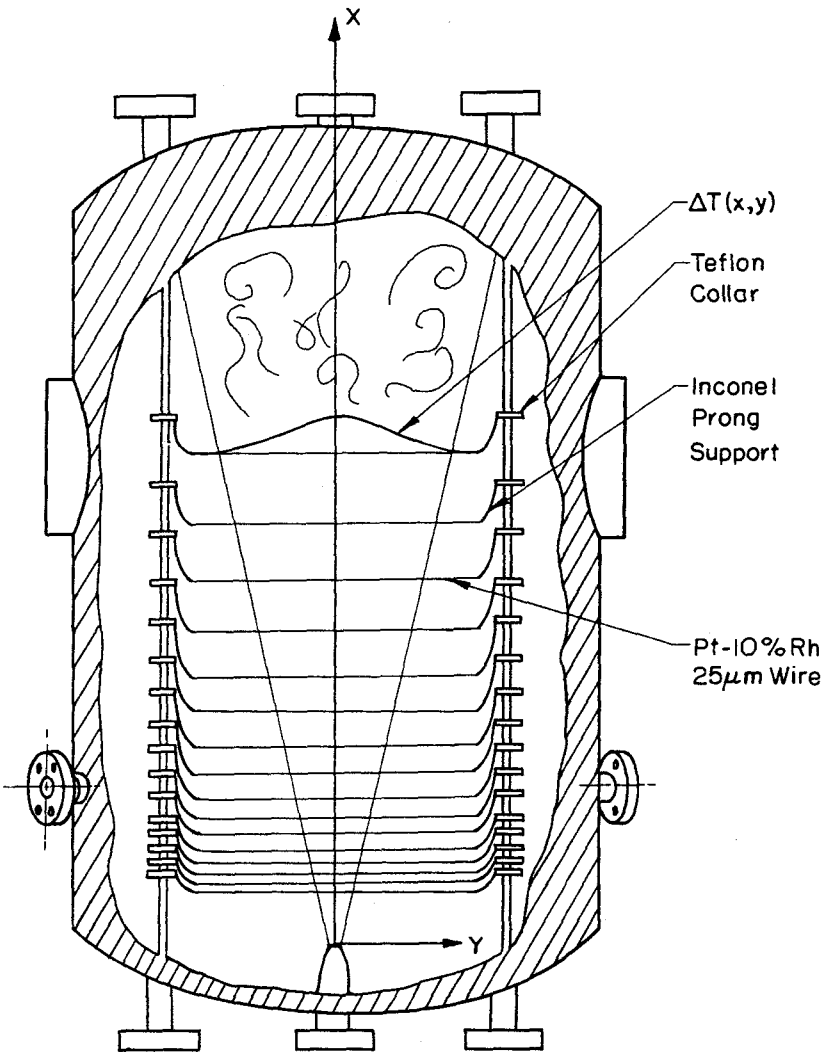

FIG. 2.4 Schematic of the diagnostics with the coordinate axes indicated.

leads going to the amplifier circuits. The prongs are attached to circular teflon collars mounted on two vertical stainless steel rods located inside the HPRV. The wires are stretched across the jet centerline from $x/d_0 = 30$ to 240 and are spaced at axial locations selected to give equal spacing on a $\log_{10}(x/d_0)$ axis. This spacing was suggested by Paul Dimotakis in view of his conjecture of a logarithmic behavior of the temperature measurements in the flame region (private communication). Figure 2.4 shows a schematic of the wires with the coordinate axes indicated.

Each wire has a typical resistance of 230 ohms and is provided with a constant current of 0.2 mA by an amplifier circuit originally designed by Dan Lang and Paul Dimotakis, and modified by Cliff Frieler. Under natural convection, a worst case, this yields an ohmic resistance heating temperature rise of 0.0006 K. Therefore, the ohmic heating is negligible when compared to the temperatures measured in the experiments and the wire sensitivity is velocity independent. Because of the extremely large aspect ratio of the wires (22,750) and the fact that the prongs are located well outside of the jet cone, end effects are also negligible.

The circuit measures wire resistance changes due to heating by the reacting jet flow, and then amplifies the signal via a variable gain stage. The signal is then filtered with a third-order low-pass Butterworth filter with the knee frequency set at 200 Hz (see Table A.3 for estimates of the wire frequency response). The rms noise without flow was measured at ~ 0.015 K and, with the long averaging times involved, did not affect the mean temperature measurements. The measurement technique is further described in Ch. 3.

2.5 Data acquisition

Data acquisition was handled by a DEC LSI-11/73 CPU-based, RT–11 computer system together with a Data Translation DT3362 12-bit, 32 differential input channel A/D converter with a maximum data rate of 250 kHz. The system also has an Andromeda Systems DAC-11 D/A converter, used for operating the remote valves, and a Wavetek Model 278 function generator, which provided the clock signal for the A/D board.

The 16 cold wires, two reference cold wires, the nozzle dynamic pressure, and the HPRV pressure were sampled at 500 Hz each for a combined data rate of 10 kHz. A typical run time of 20 seconds resulted in 200,000 individual measurements. The

computer also performed the valve sequencing during a run. This consisted of starting the A/D data acquisition, opening a firing valve to initiate the sonic N_2 stream, waiting a preset amount of time, and then opening the nozzle valve to start the experiment. After a designated run time elapsed, the computer simultaneously closed all valves and stopped the A/D data acquisition. After a run, the data were transferred via Ethernet to the HYDRA VAX/VMS cluster for processing (described in Appendix B).

CHAPTER 3

Measurement technique and jet scaling

Various methods have been used to measure flame lengths. For example, Dahm *et al.* (1984) used planar laser-induced fluorescence with an acid-base reaction in water. They seeded the basic jet fluid with a dye that would fluoresce when excited by a laser sheet until the jet dye was mixed to a chosen stoichiometric mixture ratio with acidic reservoir fluid, whereupon the fluorescence would "turn off". By slicing the jet centerline with a laser sheet oriented parallel to the jet axis, they were able to visualize a two-dimensional plane containing the axis of the jet. They measured the farthest downstream location where fluorescing dye could be seen in the laser sheet and called this the instantaneous flame length. They then ensemble-averaged many of these instantaneous measurements to define an average flame length.

A second method is to locate the farthest downstream location where the radiated light from high temperature soot formed in hydrocarbon flames can be seen (*e.g.*, Zukoski *et al.* 1984; Toner 1987). Soot is formed as a by-product of the combustion process, and radiates light only when sufficiently hot. It is assumed that the soot radiates light only within the flame zone, where the highest temperatures exist, and that beyond the flame tip, the soot cools to a temperature where visible radiation ceases. Therefore, the last occurrence of visible soot should mark the end of the flame tip. There is some concern over whether the soot cools immediately beyond the flame tip, or whether it continues to radiate light for some distance beyond the flame tip as it is cooling. The latter condition could result in overestimated flame lengths. Additionally, high heat release flames are also typically buoyancy-dominated.

Others have judged visual average flame lengths from the radiated light of a flame by eye or used long exposure photographs of the flame against a black background (*e.g.*, Hawthorne *et al.* 1948; Becker & Liang 1978).

In the current experiments, we accurately measured the low heat release of the chemical reaction to estimate flame lengths. The diagnostics utilized in the present experiments are designed to give a sensible, accurate, and consistent measure of flame length using constant current resistance thermometers.

As noted in Sec. 2.4, the thermometers are long, thin Pt-10%Rh cold wires stretched across the jet centerline at 16 axial locations. If ohmic heating of the wires and the slight nonlinearities in the temperature coefficient of resistance are neglected, then the wire voltage change ΔV for a given temperature change ΔT can be given as

$$\Delta V = I R_0 \alpha \Delta T \ , \tag{3.1}$$

where

I = current through the wire,

α = temperature coefficient of resistance,

R_0 = probe cold resistance.

The wire resistance R is well represented as a linear function of temperature, given by $R = R_0(1 + \alpha\Delta T)$. See Sandborn (1972). This assumption is valid for the temperature range of the current experiments, and the voltage increase is therefore linear with temperature.

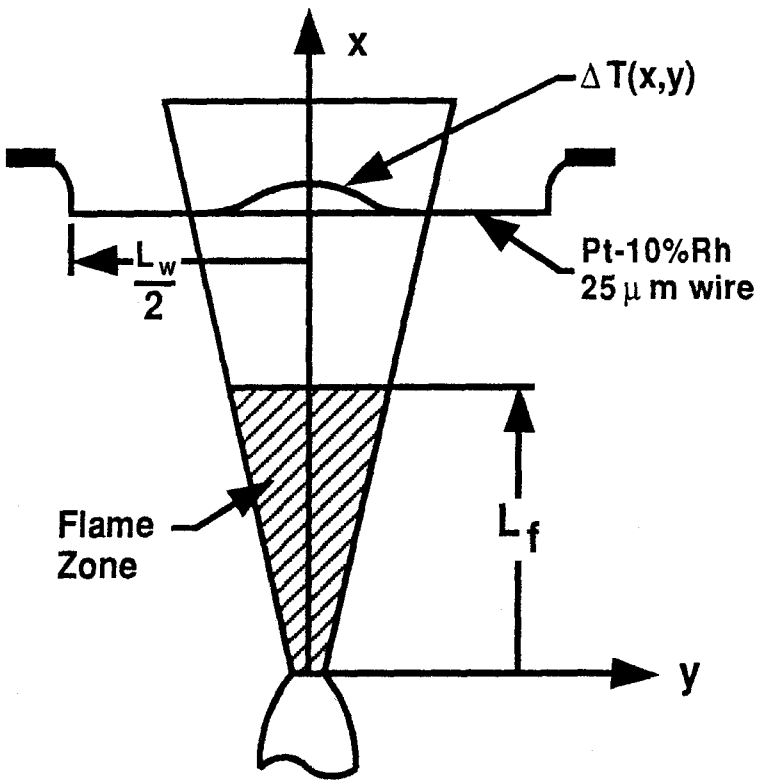

FIG. 3.1 Schematic of the jet flame zone.

3.1 Jet Scaling

The reason for choosing this particular measurement technique was motivated by the scaling laws for an axisymmetric free jet. The resistance of the cold wires, when stretched across the flame, yields an accurate estimate of the line-integrated heat release, *i.e.*, temperature rise, resulting from the chemical reaction. At the end of the flame zone, shown schematically in Fig. 3.1, the fuel has been completely consumed, so no heat release occurs downstream of this location. Beyond the flame tip, the existing heat is simply diluted by the subsequently entrained reservoir fluid. Therefore, for $x > L_f$ (where x is the streamwise (jet axis) coordinate and L_f is

the average flame length), the temperature excess is a conserved scalar. Assuming that the flow achieves a self-similar temperature profile beyond the flame tip (as observed by Becker & Yamazaki 1978), the temperature excess for $x > L_f$ should obey the jet similarity law for a scalar quantity in a momentum-dominated jet. This similarity law can be derived from dimensional arguments (*e.g.*, Chen & Rodi 1980), has been verified experimentally (*e.g.*, Dowling & Dimotakis 1990), and is given by

$$\frac{\Delta T(x,y)}{\Delta T_f} = \kappa \frac{d^*}{x - x_0} g(\eta) \ , \tag{3.2a}$$

where $\Delta T(x,y)$ is the temperature rise at (x,y), y is the transverse coordinate, ΔT_f is the adiabatic flame temperature rise, κ is a constant (determined by experiment), d^* is the momentum diameter of the jet (see Eq. 2.1), $g(\eta)$ is the similarity mean profile function (determined by experiment), η is the similarity variable defined as

$$\eta \equiv \frac{y}{x - x_0} \ , \tag{3.2b}$$

with x_0 the virtual origin. The function $g(\eta)$ has a maximum value of 1 at $\eta = 0$ and goes to zero outside the jet edges ($\eta > 0.25$).

Taking the line integral of Eq. 3.2a along y, at constant x (along a wire), and realizing that $g(\eta)$ goes to zero before $y = \pm L_w/2$, yields

$$\begin{aligned} \frac{1}{L_w} \int_{-L_w/2}^{L_w/2} \frac{\Delta T(x,y)}{\Delta T_f} dy &= \kappa \frac{d^*/L_w}{x - x_0} \int_{-L_w/2}^{L_w/2} g(\eta)\, dy \\ &= \kappa \frac{d^*/L_w}{x - x_0} \int_{-\infty}^{\infty} g(\eta)\, dy \\ &= \kappa \left(\frac{d^*}{L_w} \right) \int_{-\infty}^{\infty} g(\eta)\, d\eta \\ &\neq \mathrm{fn}(x) \ , \end{aligned} \tag{3.3}$$

where L_w is the span (length) of the wire. The temperature measurement performed by each wire is the line integral at constant x given by

$$\frac{1}{L_w}\int_{-L_w/2}^{L_w/2}\Delta T(x,y)\,dy\ . \tag{3.4}$$

This measurement is analogous to the product thickness used for the shear layer (*e.g.*, Dimotakis 1989). The product thickness $\delta_P(x)$, normalized by L_w, will be defined as

$$\frac{\delta_P(x)}{L_w} \equiv \frac{1}{L_w}\int_{-\infty}^{\infty}\frac{\Delta T(x,y)}{\Delta T_f}\,dy\ . \tag{3.5}$$

The product thickness $\delta_P(x)$ can be thought of as the width of a top-hat temperature profile of height ΔT_f that results in the same area as that found under the $\Delta T(x,y)$ profile for that x location. Equations 3.5 and 3.3 are equivalent to Eq. 3.4 divided by ΔT_f. Therefore, the time-averaged, line-integrated mean temperature rise measured at each wire beyond the flame tip at L_f is expected to asymptote to a constant value. Accordingly, the line integral will rise to that asymptotic value as dictated by the cumulative mixing and chemical product formation up to that location for values of $x < L_f$.

Figure 3.2 shows a sample of the raw data from the 16 wires spanning $x/d_0 =$ 30 to 240, along with two reference wires placed outside of the jet cone at $x/d_0 = 0$ and 240, and the scaled velocity trace. Starting with the bottom trace and working up, the lowest trace is the reference wire at $x/d_0 = 0$ (partially obscured by the x-axis), then the 16 measurements from $x/d_0 = 30$ to 240, the other reference wire at $x/d_0 = 240$, and, finally, the scaled velocity trace. The reference wire at $x/d_0 = 0$ measures the temperature of the ambient reservoir fluid and the reference wire trace at $x/d_0 = 240$ indicates the arrival of hot recirculated products at the last measuring station, thus determining the temporal extent of uncontaminated data. The scaled velocity trace indicates the time required to establish steady state flow.

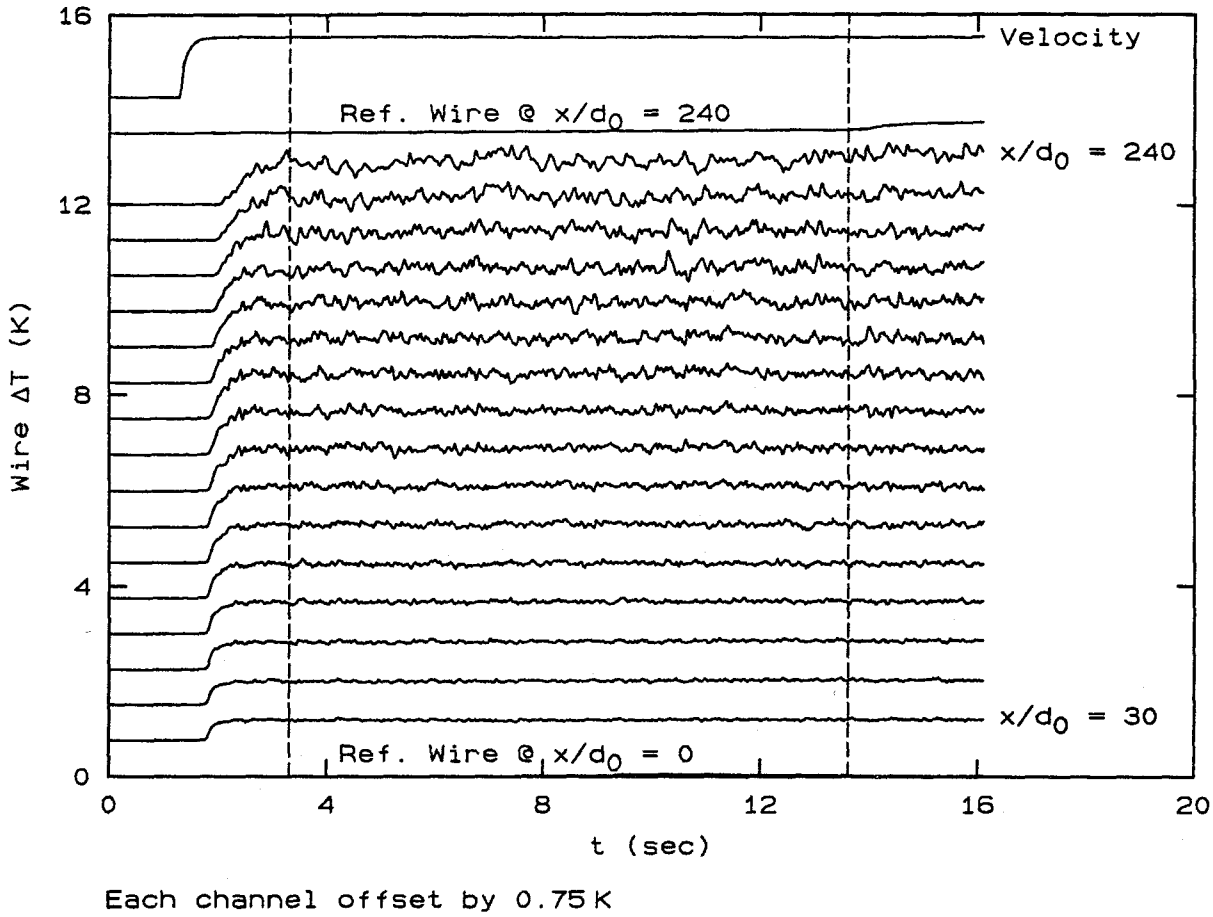

FIG. 3.2 Sample traces of cold wire raw data (see text for description of plot). The dashed lines mark the averaging interval used for Fig. 3.3.

These data were processed to produce Fig. 3.3. It plots the nondimensional product thickness, given by Eq. 3.5, versus $\log_{10}(x/d^*)$ for four different ϕ's at $\Delta T_f = 7\,\mathrm{K}$. The solid line for each set of data is a compound curve fit with a linear least squares fit to the ramp region and a cubic spline fit to the knee region, with the appropriate matching of slope and curvature at the crossover. The flame length L_f will be defined as the 99% of maximum δ_p/L_w point, in the same spirit as the definition of a 99% boundary layer thickness. The expected increase in the integrated temperature rise is observed, as well as the asymptotic value at the end

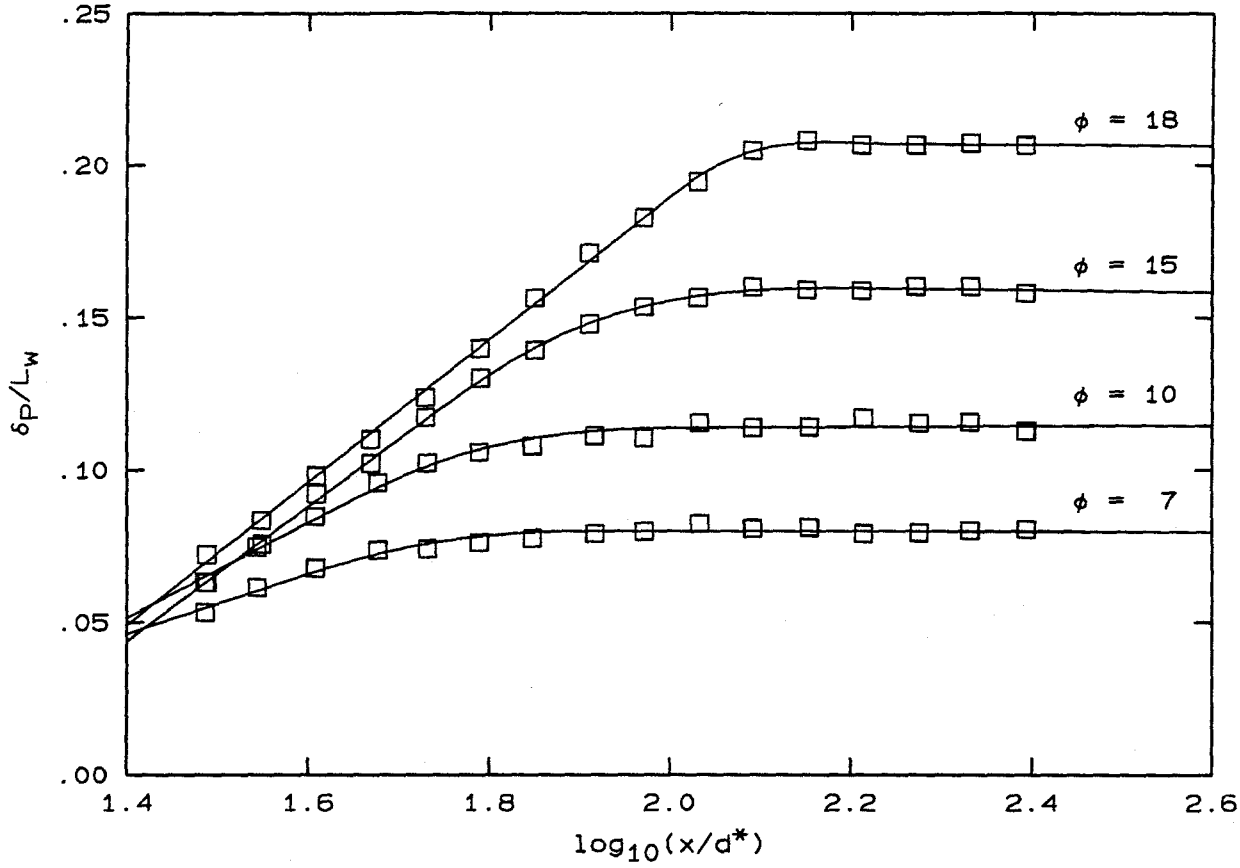

FIG. 3.3 Sample plot of product thickness versus $\log_{10}(x/d^*)$ for several ϕ's.

of the flame tip. The measurements display a linear behavior in the ramp region when plotted in the semi-logarithmic coordinates suggested by the choice of wire spacing, and corroborate the conjecture by Dimotakis mentioned in Sec. 2.4.

The fact that the measurements achieve a constant level as predicted suggests that the assumption of a self-similar temperature profile beyond the flame tip is valid. It should be noted that based on the current definition of L_f, 1% of the heat release occurs beyond $x = L_f$. It is possible that this additional heat release could conspire with a non-similar temperature profile that is developing into the self-similar one to result in a constant temperature measurement. This might cause us to

underestimate, or overestimate, the flame length, as defined by some other criterion. However, we are mainly interested in *changes* in L_f with Reynolds number, and therefore, regardless of the definition chosen, it is the change in L_f with increasing Reynolds number that is important here.

It should also be noted that the constant level achieved by the temperature measurements beyond the flame tip in Fig. 3.3 only applies to a momentum-dominated jet. The entrainment rate of a buoyant jet is higher than that of a momentum-dominated jet (*e.g.*, Becker & Yamazaki 1978). This additional entrainment of cold reservoir fluid will typically cause the temperature measurements in the buoyancy-dominated region to decrease rather than remain constant. The fact that the measurements in Fig. 3.3 achieve a constant level demonstrates that this choice of flame temperature places the jet in the momentum-dominated regime out to the farthest measuring station for all the ϕ's investigated. This will be discussed further in Sec. 4.2.

CHAPTER 4

Results and Discussion

The present experiments investigate a steady, effectively unconfined, turbulent jet issuing into a quiescent reservoir. One jet nozzle with an exit diameter of $d_0 = 2.5\,\mathrm{mm}$ (0.1 in.) was used for all of the experiments reported here. For reasons discussed in Sec. 4.3, all runs were performed at pressures between $1\,\mathrm{atm} \leq p \leq 15\,\mathrm{atm}$. The jet gas was always F_2 in a N_2 diluent and the reservoir gas was always NO in a N_2 diluent.

4.1 Reynolds Number Effects

Experiments at four stoichiometric mixture ratios ϕ were performed at each Reynolds number to produce four different flame lengths. The standard diffusion flame convention (*e.g.*, Kuo 1986) defines ϕ as the fuel to oxidizer ratio, divided by the fuel to oxidizer stoichiometric ratio, *i.e.*,

$$\phi \equiv \frac{(f/o)}{(f/o)_{\mathrm{st}}} \ , \tag{4.1a}$$

where f and o are mass or mole fractions. There is no need to distinguish which species is fuel and which is oxidizer for this study. But, in an effort to be consistent with diffusion flame theory in which the fuel is typically carried by the jet gas and the quiescent reservoir contains the oxidizer, this work will follow the same convention. Therefore, ϕ will be defined as the mass fraction of F_2 in N_2, divided by the mass fraction of NO in N_2, normalized by the corresponding stoichiometric mass fraction ratio, or

$$\phi \equiv \frac{(Y_{F_2}/Y_{NO})}{(Y_{F_2}/Y_{NO})_{\mathrm{st}}} \ , \tag{4.1b}$$

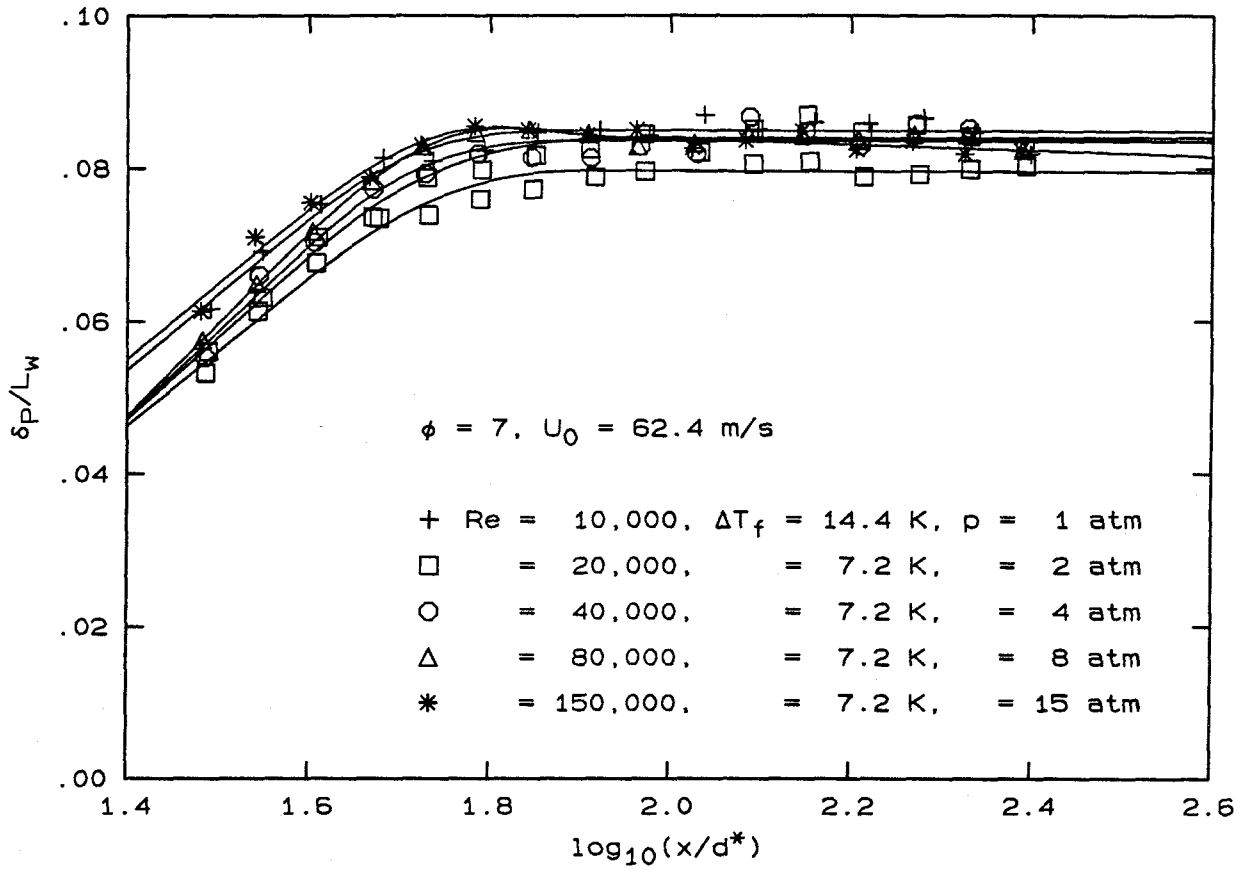

FIG. 4.1 Normalized product thickness versus $\log_{10}(x/d^*)$, $\phi = 7$.

where the mass fraction, Y_i, is defined for a mixture of N species as

$$Y_i \equiv \frac{m_i}{\sum_{i=1}^{N} m_i} \quad , \tag{4.2}$$

and

$$m_i = \text{mass of the } i^{\text{th}} \text{ species} \ .$$

The adiabatic flame temperature rise ΔT_f for each ϕ was computed using the CHEMKIN chemical kinetics program (Kee *et al.* 1980). The four values of ϕ with the corresponding mass fractions and ΔT_f's are given in Table 4.1.

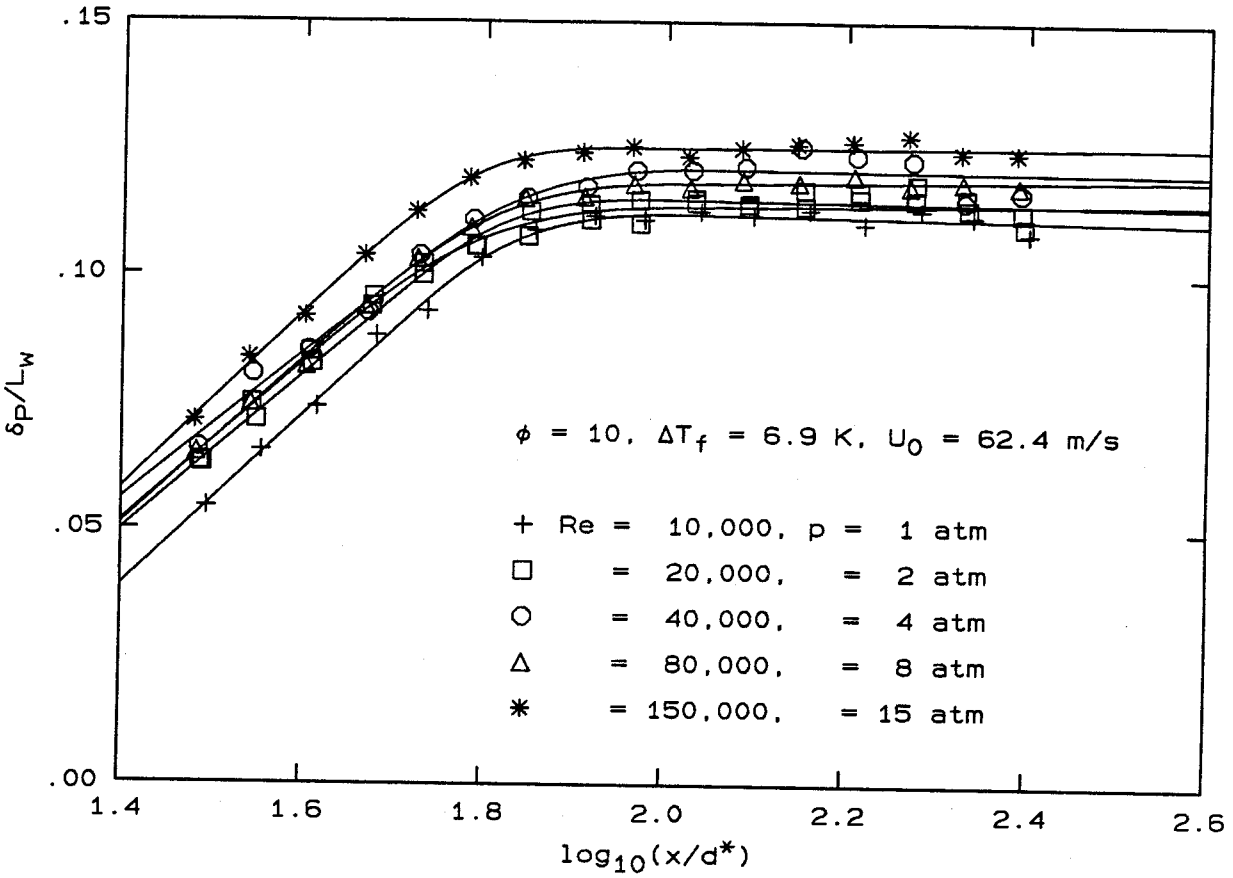

FIG. 4.2 Normalized product thickness versus $\log_{10}(x/d^*)$, $\phi = 10$.

Table 4.1: Stoichiometric mixture ratios, mass fractions, and adiabatic flame temperature rises used in Sec. 4.1.

ϕ	Y_{F_2}	Y_{NO}	ΔT_f (K)
7.0	0.0127	0.0029	7.2
10.0	0.0174	0.0028	6.9
14.0	0.0237	0.0027	6.9
17.9	0.0300	0.0027	6.7

The choice of ΔT_f was determined from several preliminary experiments. The lowest value of ΔT_f that could be measured accurately and with repeatability was

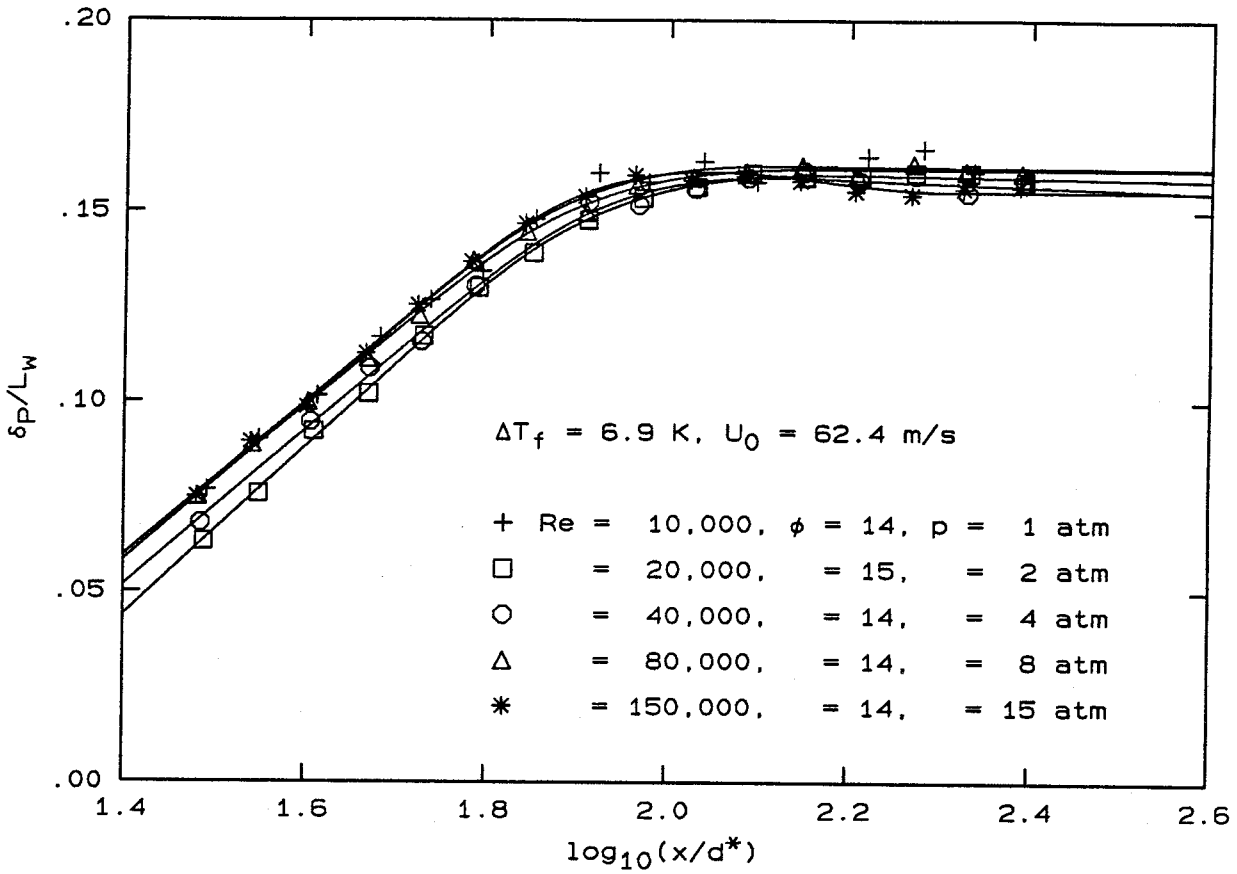

FIG. 4.3 Normalized product thickness versus $\log_{10}(x/d^*)$, $\phi = 14$ and 15.

sought to reduce both buoyancy effects and heat release effects on the flow dynamics. Section 4.2 describes the choice of $\Delta T_f \approx 7\,\mathrm{K}$ on the basis of buoyancy concerns and Sec. 4.3 demonstrates that this low flame temperature is characterized by a fast kinetic rate.

Figure 4.1 shows the data for the $\phi = 7$ runs. The solid line is a compound curve fit with a linear least squares fit in the ramp region and a cubic spline fit to the knee region. The run at $Re = 10,000$ required a higher adiabatic flame temperature because of fluorine depletion in the nozzle (described further in Sec. 4.3). Similar results, for the runs at $\phi = 10$, 14, and 18, are given in Figs. 4.2, 4.3, and

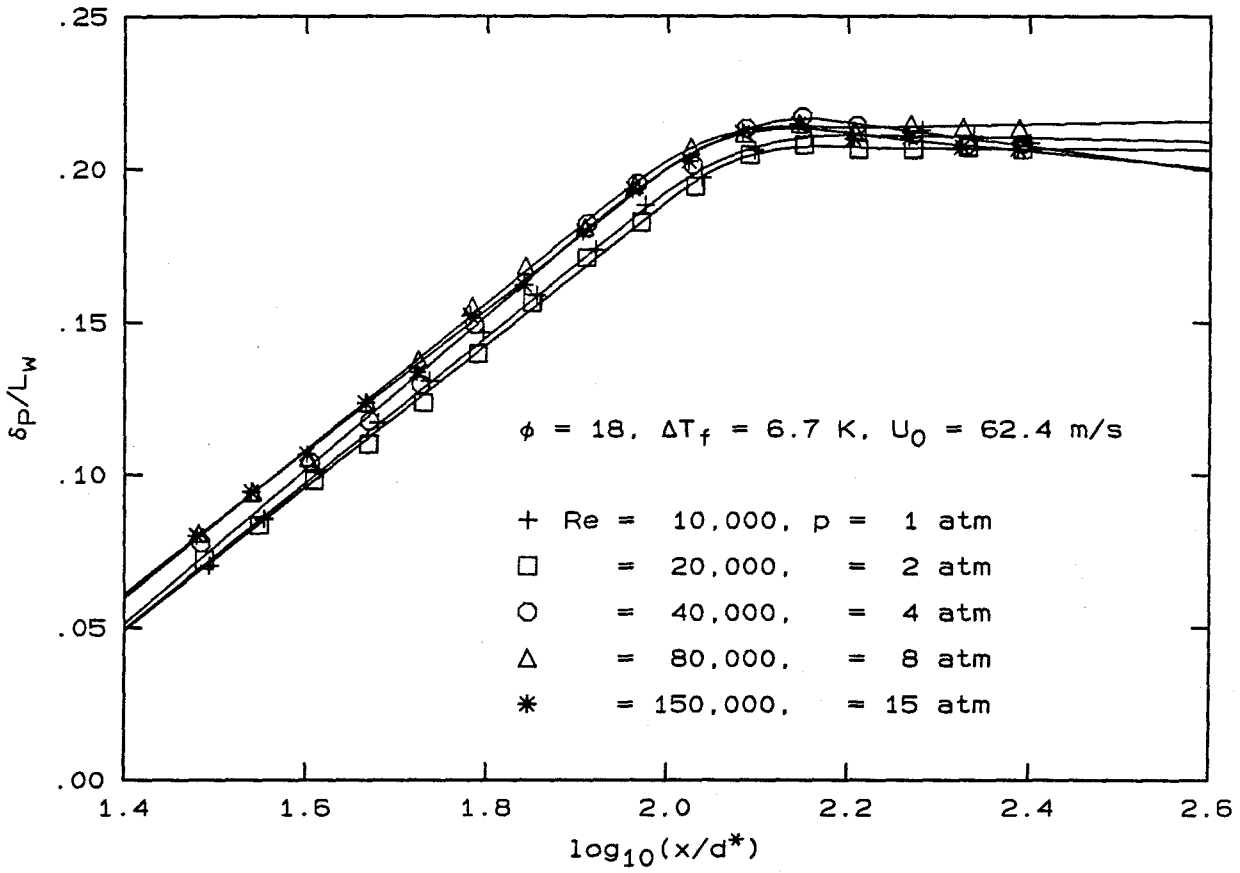

FIG. 4.4 Normalized product thickness versus $\log_{10}(x/d^*)$, $\phi = 18$.

4.4, respectively. The runs were fairly repeatable as shown by the good agreement of the repeated runs at $Re = 20,000$ (squares) in Fig. 4.2. All of the runs exhibit a linear ramp region when plotted in semi-logarithmic coordinates and a nearly constant asymptotic level after the knee or flame tip region. Figure 4.5 shows the entire set of data from Figs. 4.1, 4.2, 4.3, and 4.4, plotted on the same scale.

The average flame lengths were estimated from these curves by determining the 99% of maximum δ_P/L_w point. These flame lengths are plotted versus ϕ for the various Reynolds numbers in Fig. 4.6. The straight lines are linear least-squares

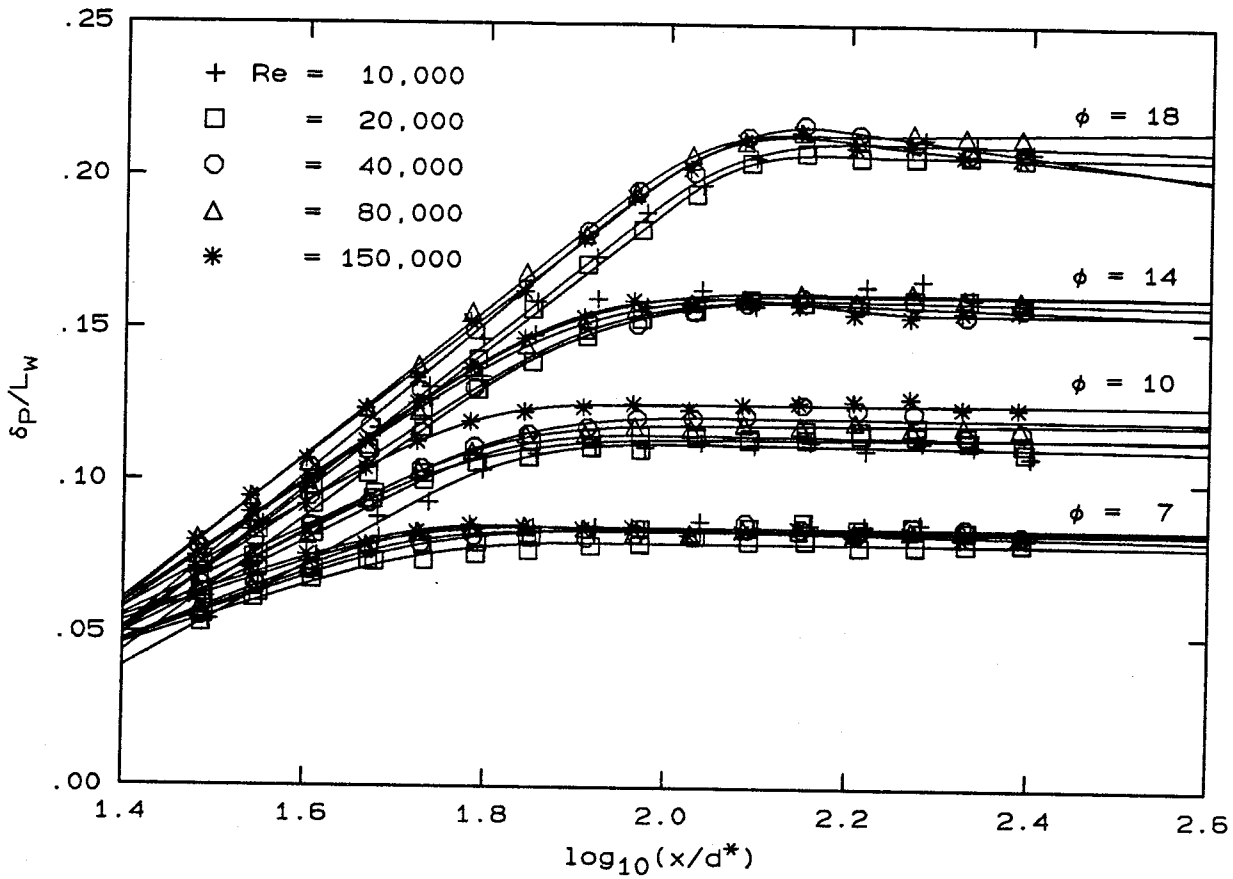

FIG. 4.5 Normalized product thickness versus $\log_{10}(x/d^*)$ for the various ϕs.

fits to the data of the form

$$\frac{L_f}{d^*} = A\,\phi + L_0 \ , \tag{4.3}$$

where A and L_0 are functions of Re with A being the slope and L_0 being defined as the "mixing virtual origin." This mixing virtual origin is a new observation and corresponds to the abscissa-intercept in Fig. 4.6, *i.e.*, the flame length extrapolated to $\phi = 0$. If the flow could be described by its far-field behavior at the nozzle exit, then L_0 would be the flame length measured in the limit of $\phi \to 0$. The variation of L_0 in Fig. 4.6 indicates that this mixing virtual origin systematically decreases with increasing Reynolds number for $Re \geq 20,000$. Some of the variation in L_0

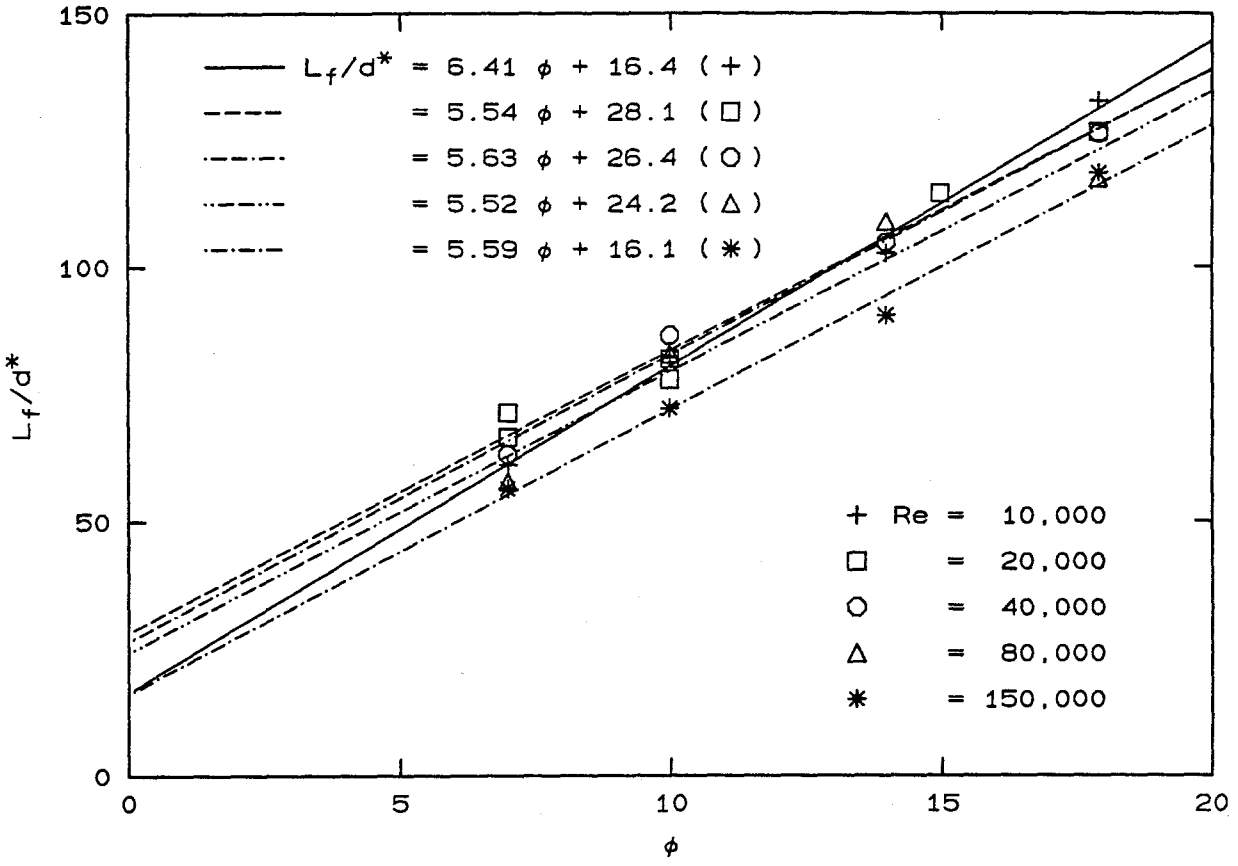

FIG. 4.6 Normalized flame length versus ϕ.

could be attributable to the uncertainty in the curve fits used for the flame length determination. Another possibility could be a variation in x_0 with increasing Re. However, even combined, these effects would not be large enough to explain such a large variation in L_0. A nonzero intercept in itself is not surprising, if one realizes that the potential core extends roughly six diameters from the nozzle exit and the self-similar region of the jet typically begins around $x/d_0 = 20$ (*e.g.*, Dowling & Dimotakis 1990). Therefore, fully developed turbulent mixing on a molecular scale requires some distance downstream of the nozzle exit to develop, hence the streamwise delay in molecular mixing. The fact that L_0 has such a large value and that it varies with Re, however, is a new observation.

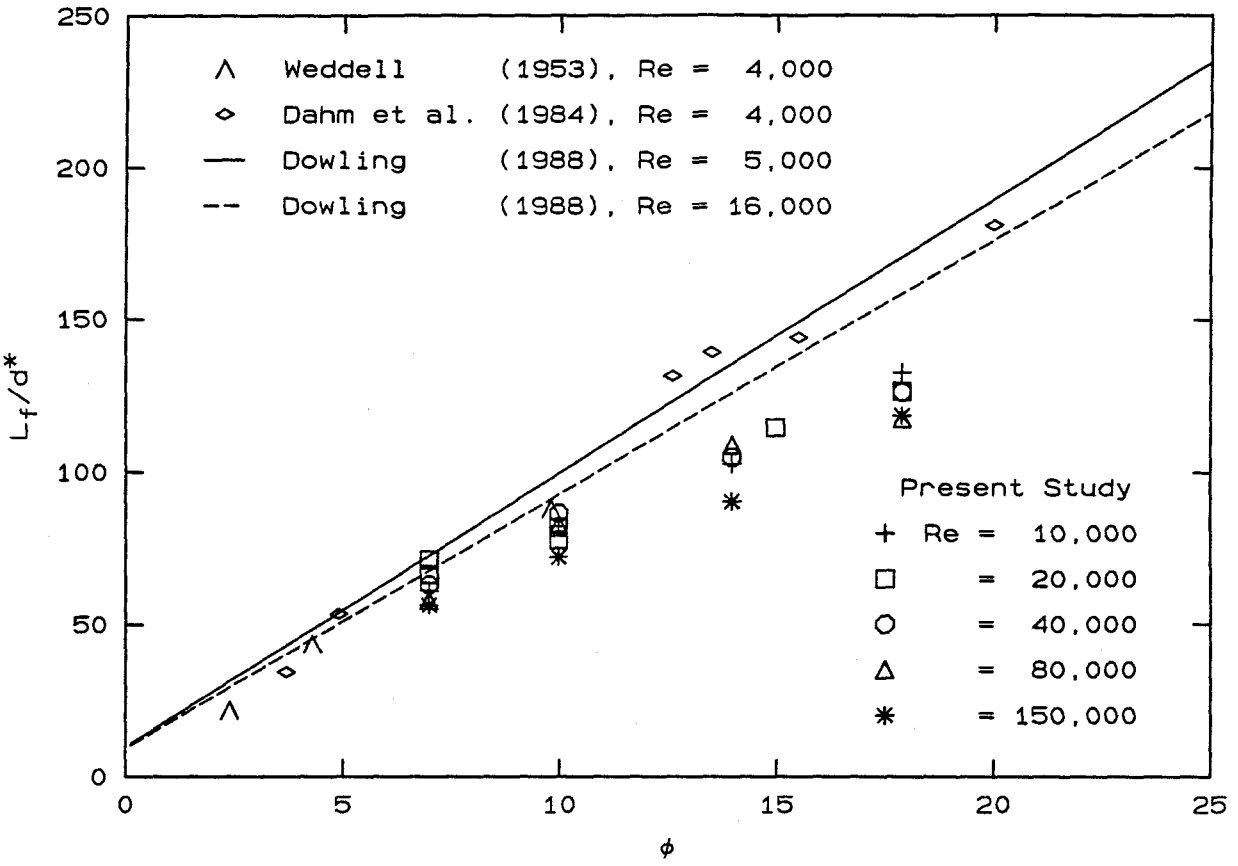

FIG. 4.7 Comparison of normalized flame lengths versus ϕ.

The data of Fig. 4.6 are compared with the average flame length measurements of Weddell (in Hottel 1953), Dahm *et al.* (1984), and Dowling (1988) in Fig. 4.7. The measurements of Weddell and Dahm *et al.* were performed in water with acid-base reactions, utilizing methods where the jet fluid could be seen until mixed to the stoichiometric mixture ratio with acidic reservoir fluid. Their data indicate the farthest downstream location where unreacted jet fluid could be seen. Dowling worked in gas phase and inferred maximum flame lengths from the probability density functions (PDFs) of his Rayleigh scattering concentration measurements. He assumed a 99% complete reaction in his calculations of the flame lengths presented in Fig. 4.7.

The current results yield mean flame lengths that are roughly 25% shorter than those of Dahm *et al.* and Dowling at the higher ϕ's. This discrepancy could be attributed to two possibilities. The first is the difference in Schmidt number, since, for water, $Sc \approx 10^3$, and for a gas, $Sc \approx 1$. However, the data of Dahm *et al.* in water agree with the inferred gas-phase flame lengths of Dowling, implying that there is no Sc effect. The other possibility could be the different methods used for estimating the flame length. Dahm *et al.* ensemble-averaged the farthest downstream location where fluorescing dye could be seen to define an average flame length, and Dowling estimated maximum flame lengths.

An important feature of Dowling's data is the reduction in the slope A of the L_f/d^* curve from $A \approx 9$ for $Re = 5,000$ to $A \approx 8.35$ for $Re = 16,000$. Although this change is not as large as in the current experiments, within a similar Reynolds number range, the behavior is qualitatively similar.

The main result of this investigation is that there are Reynolds number effects on flame length as illustrated in Figs. 4.8 and 4.9. The values of the slope A are plotted in Fig. 4.8. A least-squares fit to the data of Weddell and Dahm *et al.* in Fig. 4.7 results in a value of $A \approx 9$ for both sets of data. The bars on the data indicate the statistical confidence in the linear least-squares fit. The slope for the data of Dowling changes roughly 7% for a change in Reynolds number from 5,000 to 16,000. The data of the current experiments display a larger change in A, *i.e.*, roughly 13% from $Re = 10,000$ to $Re = 20,000$. The slope for the data of the current experiments reaches a constant value of $A \approx 5.6$ for $Re \geq 20,000$. The entrainment studies of Ricou & Spalding (1961) found that the entrainment rate of their gas jet became constant for $Re \geq 25,000$. This Reynolds number is similar to the one where A becomes constant, as described above. However, the behavior of the mixing virtual origin does not seem to have reached an asymptotic behavior at this Reynolds number or even up to $Re = 150,000$. Whether or not the threshold

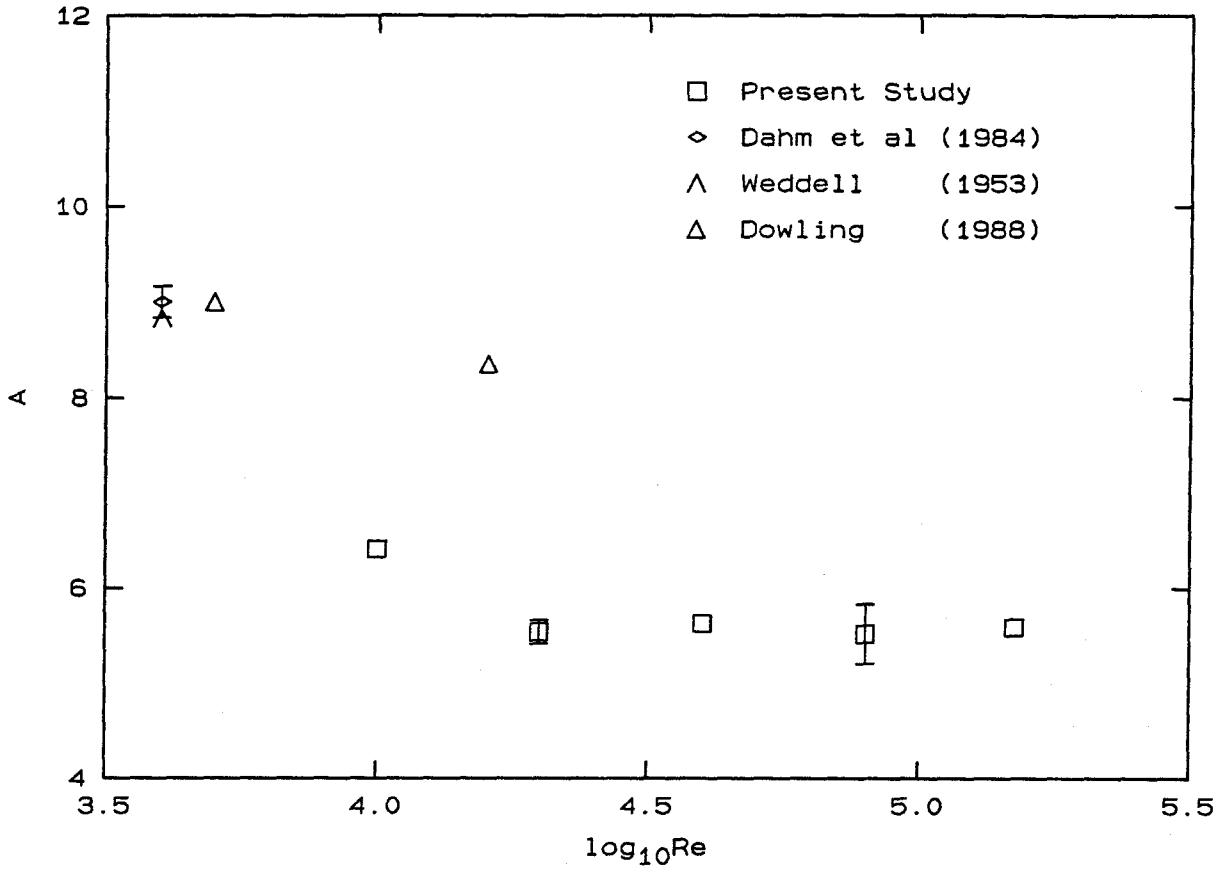

FIG. 4.8 The slope A of the curve fits to the data of Fig. 4.7 versus $\log_{10} Re$. Bars represent the statistical confidence in the linear least-squares fit and are omitted if smaller than the plotted symbol.

Reynolds number of Ricou & Spalding can be correlated to the asymptotic behavior of A is unclear.

The variation in L_0 is plotted in Fig. 4.9. All of the experiments have a nonzero mixing virtual origin. The trend seems to be for this quantity to increase with increasing Reynolds number up to $Re = 20,000$, and then to decrease. Unfortunately, runs at higher Reynolds numbers are required to determine if this quantity asymptotes to some constant level with increasing Reynolds number. It is interesting to note that L_0 accounts for an increasingly larger fraction of the flame length

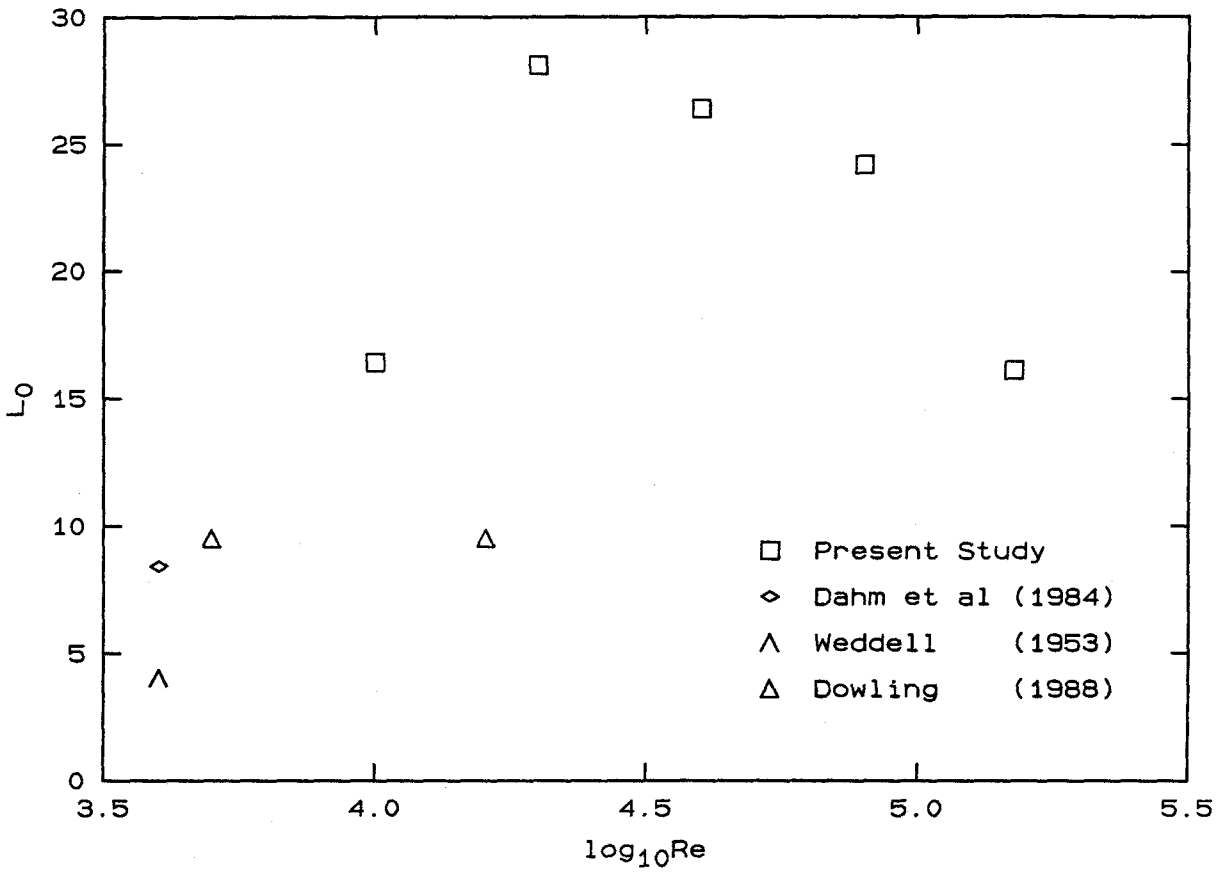

FIG. 4.9 Mixing virtual origin L_0 of the curve fits to the data of Fig. 4.7 versus $\log_{10} Re$.

as the flame length decreases, *i.e.*, as ϕ decreases. Therefore, changes in L_0 with Reynolds number have a proportionally larger effect on L_f at smaller ϕ's.

4.2 Buoyancy Effects

Buoyancy is an issue that was explicitly addressed in these experiments. The similarity law of Eq. 3.2a is valid only for the momentum-dominated region of the jet. The positively buoyant jet (*i.e.*, a jet in which the momentum flux increases with x) entrains at a higher rate than the momentum-dominated jet (*e.g.*, Becker & Yamazaki 1978). Therefore, the similarity law that results in a constant average temperature measurement beyond the flame tip will change. This can be understood by revisiting the scaling arguments of Sec. 3.1.

Recall that the temperature excess beyond the flame tip is a conserved scalar obeying the similarity law for a momentum-dominated jet given by Eq. 3.2a. The temperature excess beyond the flame tip for a buoyancy-dominated jet is also a conserved scalar and obeys the similarity law (*e.g.*, Chen & Rodi 1980) given by

$$\frac{\Delta T(x,y)}{\Delta T_{\mathrm{f}}} = \beta \frac{d^*}{(x-x_0)^{5/3}}\, g(\eta) \ , \tag{4.4}$$

where β for the buoyant jet is different from the κ of the momentum-dominated jet in Eq. 3.2a and the mean temperature profile function $g(\eta)$ is also different. The similarity variable η is the same as for the momentum-dominated jet, given by $\eta = y/(x-x_0)$. Integrating Eq. 4.4 along y, at constant x, and again realizing that $g(\eta)$ goes to zero before $y = \pm L_{\mathrm{w}}/2$, yields

$$\begin{aligned}
\frac{1}{L_{\mathrm{w}}} \int_{-L_{\mathrm{w}}/2}^{L_{\mathrm{w}}/2} \frac{\Delta T(x,y)}{\Delta T_{\mathrm{f}}}\, dy &= \frac{\beta d^*}{L_{\mathrm{w}}(x-x_0)^{5/3}} \int_{-L_{\mathrm{w}}/2}^{L_{\mathrm{w}}/2} g(\eta)\, dy \\
&= \frac{\beta d^*}{L_{\mathrm{w}}(x-x_0)^{5/3}} \int_{-\infty}^{\infty} g(\eta)\, dy \\
&= \frac{\beta d^*}{L_{\mathrm{w}}(x-x_0)^{2/3}} \int_{-\infty}^{\infty} g(\eta)\, d\eta \\
&\sim x^{-2/3} \ .
\end{aligned} \tag{4.5}$$

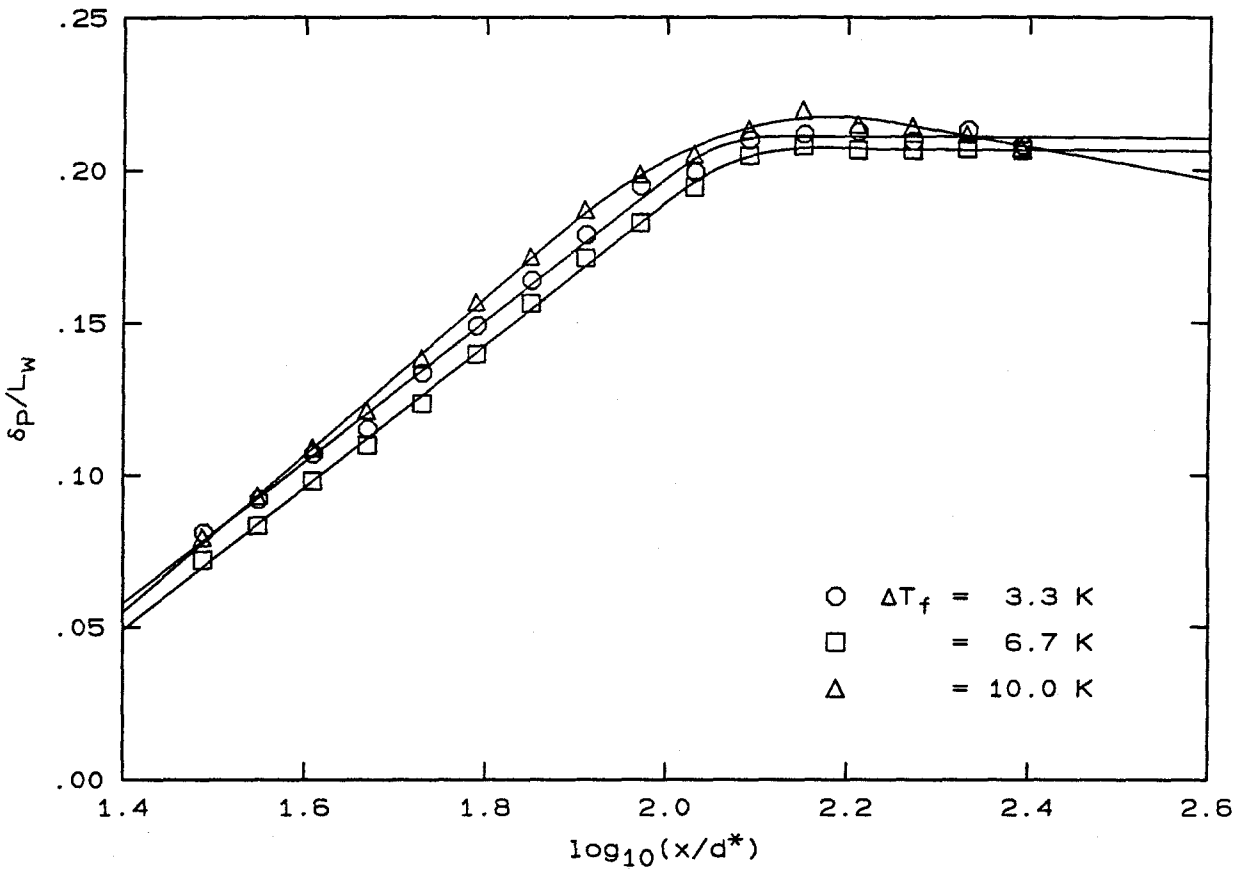

FIG. 4.10 Scan of ΔT_f for $\phi = 17.9$, $Re = 20,000$, $U_0 = 62.4\,\mathrm{m/s}$, $p = 2\,\mathrm{atm}$.

Therefore, the average temperature measurement will decay beyond the flame tip at some point when buoyancy forces become comparable to the jet source momentum flux.

For the experiments of Sec. 4.1, ΔT_f was chosen by the requirement that the jet remain momentum-dominated up to the last measuring station at $x/d_0 = 240$ for the ϕ's investigated. This was done by performing a set of preliminary experiments at several ϕ's. The longest flame length occurs at $\phi = 17.9$. This case was examined by systematically increasing ΔT_f until the temperature measurement beyond

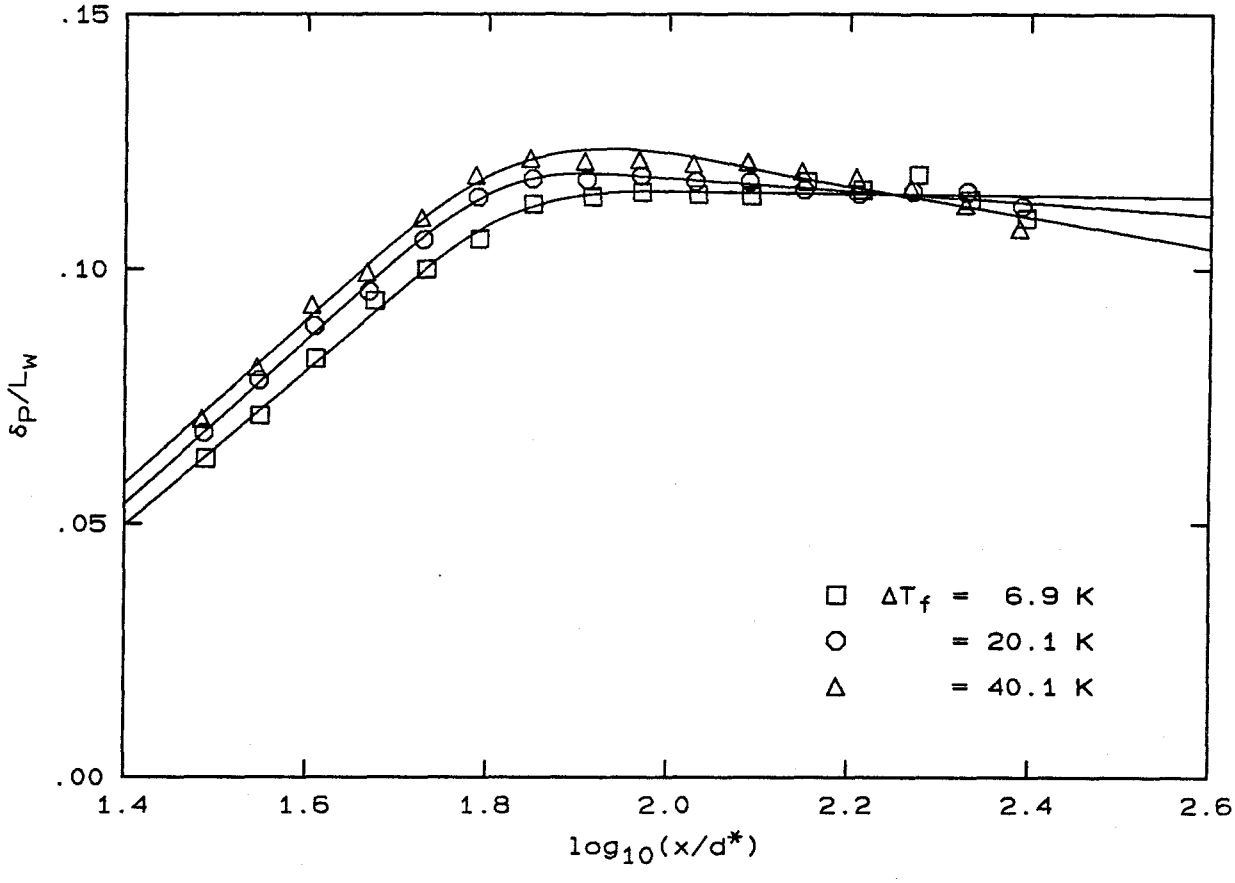

FIG. 4.11 Scan of ΔT_f for $\phi = 10$, $Re = 20{,}000$, $U_0 = 62.4\,\mathrm{m/s}$, $p = 2\,\mathrm{atm}$.

the flame tip was no longer constant, but was observed to decrease. Figure 4.10 shows these $\phi = 17.9$ runs. For the run with $\Delta T_f = 10\,\mathrm{K}$, the temperature measurement after the flame tip never attains a constant value but decreases with increasing x/d^*.

Figures 4.11 and 4.12 show similar flame temperature scans at $\phi = 10$ and 7, respectively. These shorter flames are not affected by buoyancy until much higher flame temperatures. As expected, the longest flame length is the most sensitive to buoyancy effects from temperature.

The effect of buoyancy on the jet is determined by the ratio of the buoyancy

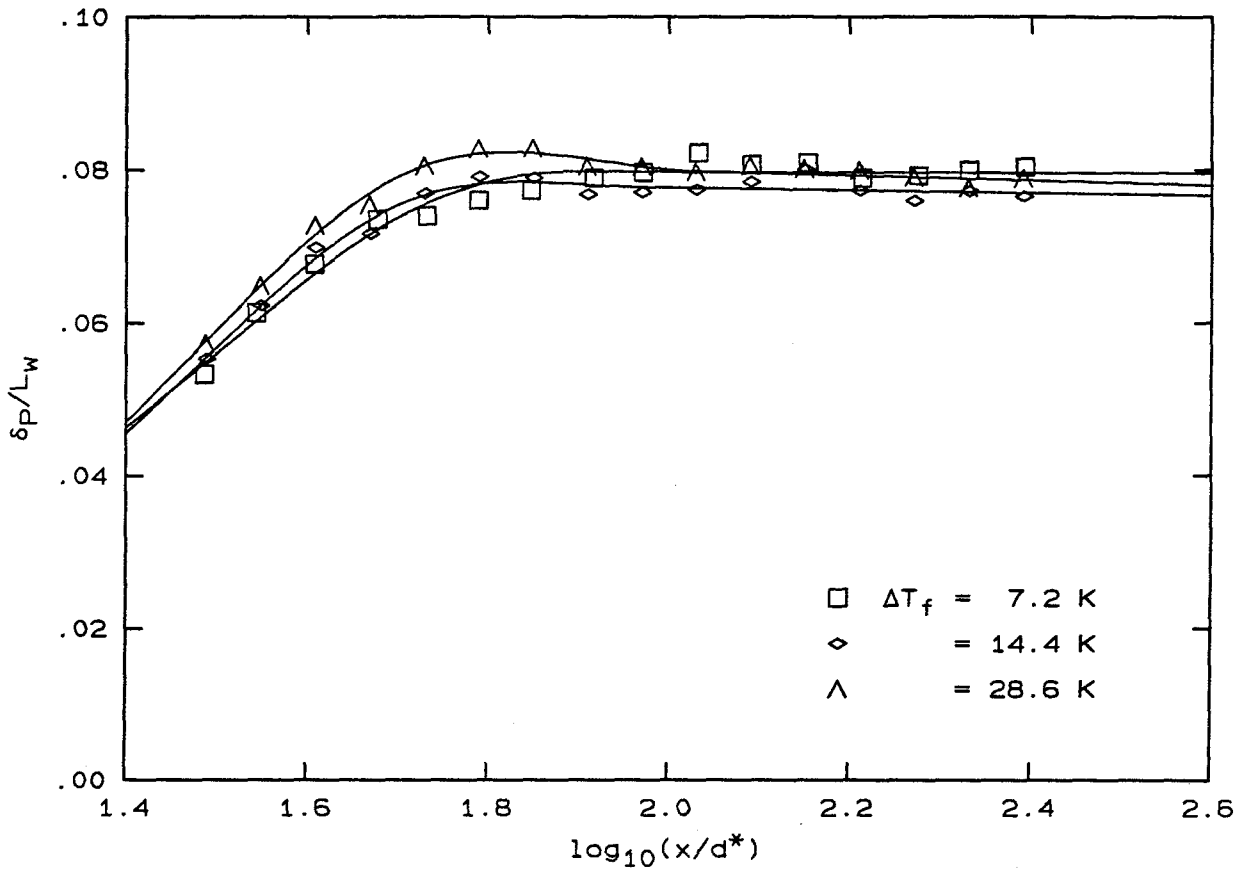

FIG. 4.12 Scan of ΔT_f for $\phi = 7$, $Re = 20,000$, $U_0 = 62.4\,\mathrm{m/s}$, $p = 2\,\mathrm{atm}$.

force on the jet cone to the nozzle exit momentum flux. Recalling the flame geometry of Fig. 3.1, the buoyancy force B on the jet can be expressed as

$$B = g\,\overline{\Delta\rho}\,V \ , \tag{4.6}$$

where g is the acceleration of gravity, $\overline{\Delta\rho}$ is the average change in density owing to heat release given by $\overline{\Delta\rho} = \rho_\infty - \overline{\rho}$, and V is the volume of the jet cone. The inertial strength of a jet source is normally characterized by the nozzle exit momentum flux J_0, given for top-hat exit velocity and density profiles by

$$J_0 = \rho_0 {U_0}^2 \frac{\pi}{4} {d_0}^2 \ . \tag{4.7}$$

Becker & Yamazaki (1978) attempted to identify when the jet is momentum-dominated and where the transition to buoyancy occurs by comparing the buoyancy force on the jet cone to the exit momentum flux. The jet grows linearly with x (*e.g.*, Eq. 4.21) so they assumed that $V \sim x^3$. They worked with high heat release flames and made the further assumption that

$$\overline{\Delta\rho} = \rho_\infty - \overline{\rho} \approx \rho_\infty \ . \tag{4.8}$$

Thus, they give a characteristic measure of the buoyancy force B as

$$B = g\,\overline{\Delta\rho}\,V \approx g\,\rho_\infty\,x^3 \ . \tag{4.9}$$

Their resulting ratio of buoyancy to momentum force, typically called the Richardson number Ri is given by

$$Ri \equiv \frac{\pi g \rho_\infty x^3}{4J_0} \ . \tag{4.10}$$

They work with the cube root of the Richardson number by defining a nondimensional streamwise coordinate ξ as

$$\xi \equiv \left(\frac{\pi g \rho_\infty}{4J_0}\right)^{1/3} x = {Ri_s}^{1/3}\frac{x}{d^*} \ , \tag{4.11}$$

where

$$Ri_s \equiv \frac{\pi g \rho_\infty d^{*3}}{4J_0} = \frac{g d^*}{{U_s}^2} \tag{4.12}$$

is the source flame-zone Richardson number. The source velocity U_s is given by

$$U_s \equiv \frac{J_0}{\dot{m}_0} \ . \tag{4.13}$$

From Eq. 4.11, $\xi \to 0$ corresponds to the momentum-dominated regime and $\xi \to \infty$ to the buoyancy-dominated regime. Becker & Yamazaki used a pitot probe and an uncorrected thermocouple to infer point measurements of density and velocity. The mass flux in their measurements was evaluated numerically from the product of

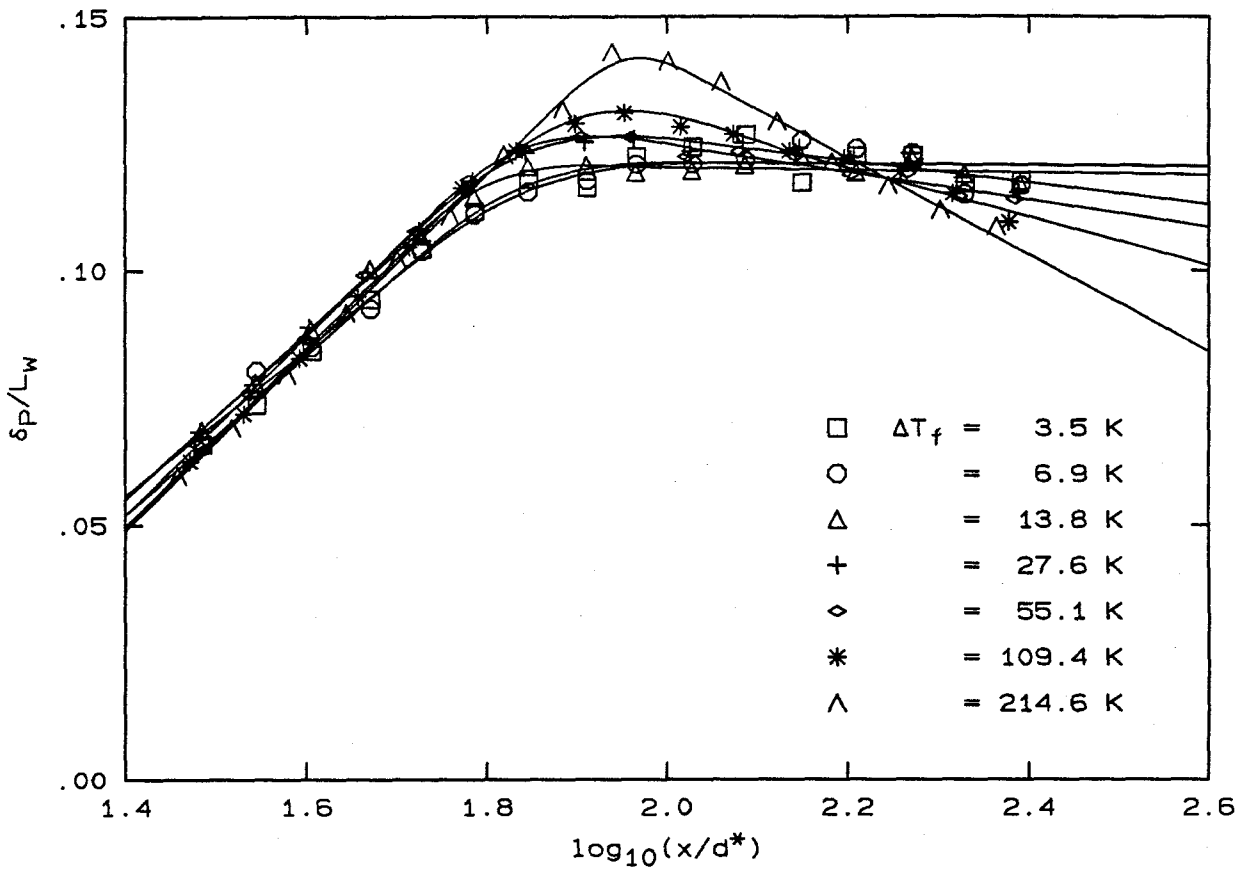

FIG. 4.13 Normalized product thickness versus $\log_{10}(x/d^*)$ for several adiabatic flame temperatures, $Re = 40{,}000$, $\phi = 10$, $U_0 = 62.4\,\mathrm{m/s}$, $p = 4\,\mathrm{atm}$.

these measurements. Although they express some concern over the errors inherent with their technique, they find that for $\xi < 1$, the mass flux of the jet is linear with x, the result expected from the similarity analysis for a momentum-dominated jet (*e.g.*, Ricou & Spalding 1961). For $\xi > 2.5$, their measurements indicated that the mass flux varies as $x^{5/2}$, which agrees with the similarity result for a buoyant jet with $\overline{\Delta\rho} \approx \rho_\infty$ (*e.g.*, Delichatsios & Orloff 1984). Toner (1987) performed more direct entrainment measurements utilizing gas chromatography and found similar behavior.

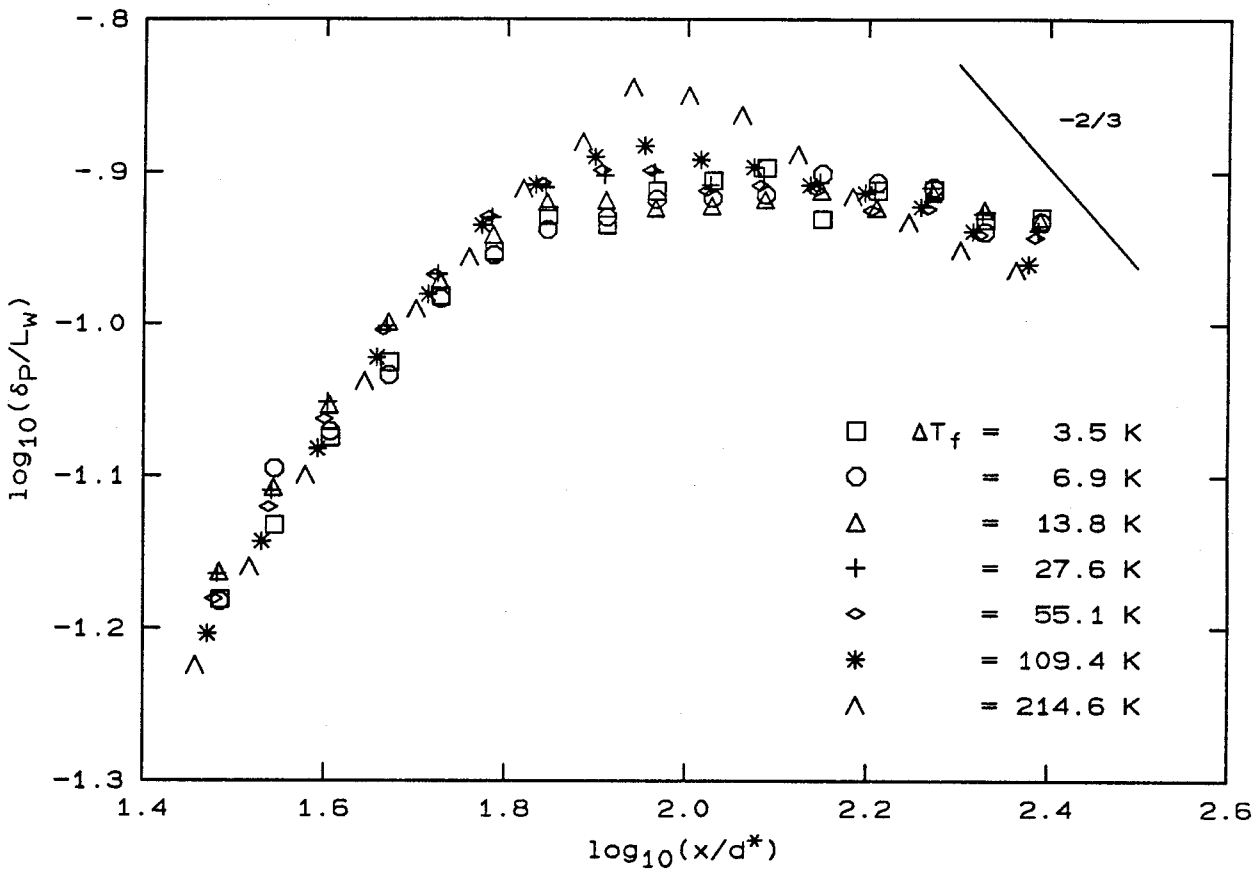

FIG. 4.14 The data of Fig. 4.13 in log-log coordinates. The -2/3 slope is included for reference.

Becker & Yamazaki and Toner used high heat release flames so their assumption of $\overline{\Delta\rho} \approx \rho_\infty$ is probably valid. However, for the present experiments, $\overline{\Delta\rho} \ll \rho_\infty$ so this assumption is not valid and $\overline{\Delta\rho}$ is retained in the buoyancy expression B of Eq. 4.9. Assuming $\rho_\infty \approx \rho_0$, $T_\infty \approx T_0$, that the temperature of the entire jet cone is scaled by $T_\infty + \Delta T_f$ (a conservative estimate), and ideal gas behavior with constant pressure yields the version of Eq. 4.11 used in the current analysis, *i.e.*,

$$\xi = \left[\frac{\pi g(\rho_\infty - \overline{\rho})}{4J_0}\right]^{1/3} x$$

$$= \left[\left(\frac{\rho_\infty - \overline{\rho}}{\rho_0}\right)\frac{g}{{U_0}^2 {d_0}^2}\right]^{1/3} x$$

$$= \left[\left(\frac{\Delta T_f}{\Delta T_f + T_\infty}\right)\frac{g}{{U_0}^2 {d_0}^2}\right]^{1/3} x \ . \qquad (4.14a)$$

The assumption of constant pressure in the jet cone is not strictly true. Townsend (1976), for example, notes that $p + \overline{v'^2} \simeq p_\infty$ where p is the jet pressure, v' is the instantaneous transverse velocity fluctuation, and p_∞ is the reservoir pressure. However, typically $\overline{v'^2} \ll p$ for these experiments, so the assumption of constant pressure is certainly valid.

Experiments to test the buoyancy scaling ξ on such parameters as flame temperature and exit velocity were performed. Figure 4.13 shows a set of experiments spanning adiabatic flame temperatures ΔT_f from 3.5 K to 215 K. A Reynolds number of 40,000 was chosen for this scan. A ϕ of 10 placed the flame tip in the center of the $\log_{10}(x/d_0)$ range, thus giving an equal number of points on each side of the knee. The temperature measurements beyond the flame tip reach a constant value for the low heat release runs, indicating that they are momentum-dominated. As the flame temperature increases, however, the temperature measurements no longer attain a constant level but begin to decrease with increasing x/d^*. This is evidence of the jet beginning to feel the effects of buoyancy.

To compare the temperature decay after the flame tip in Fig. 4.13 with the $x^{-2/3}$ scaling discussed above, the data were plotted in log-log coordinates in Fig. 4.14. In these coordinates, a power law behavior shows up as a linear region with the power of x given by the slope. The -2/3 slope is included for reference.

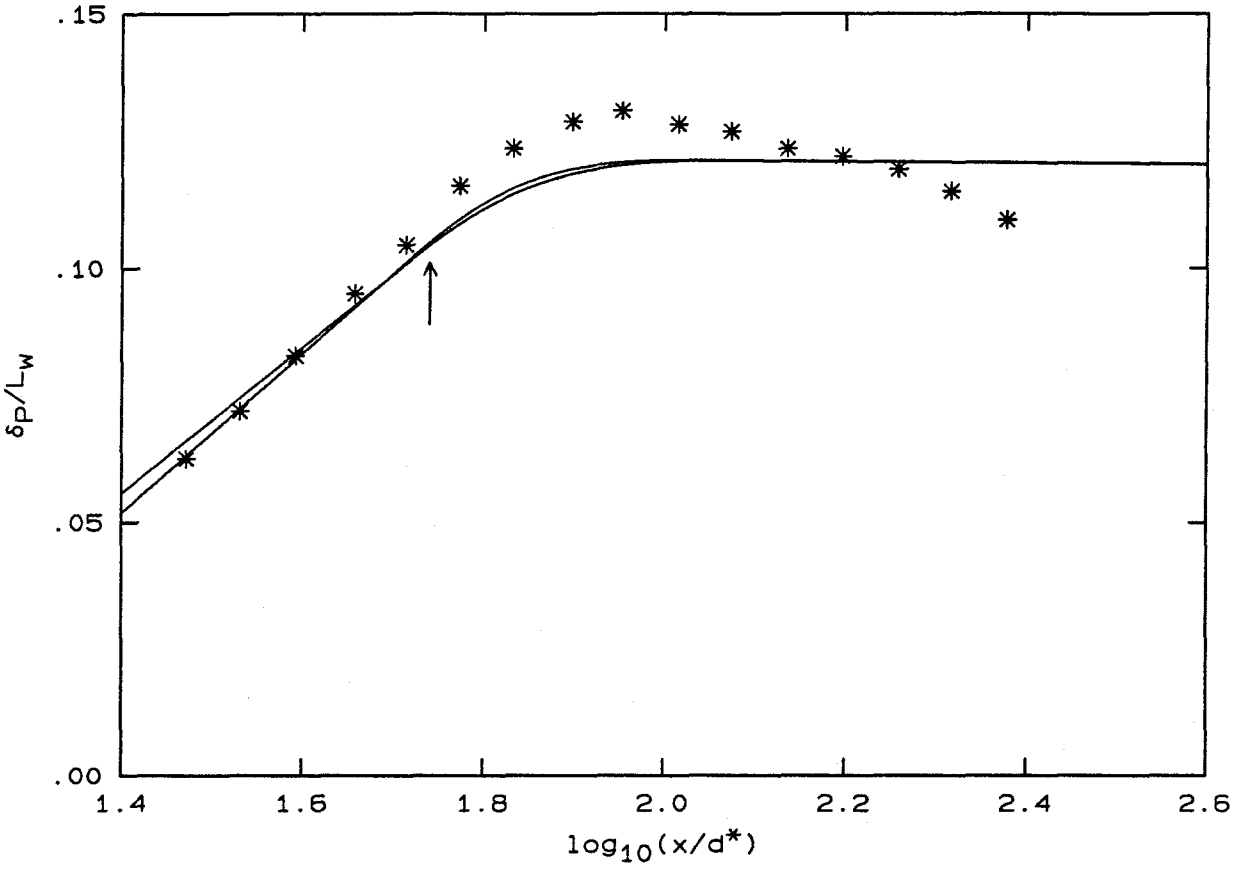

FIG. 4.15 Plot used to determine x_t for the $\Delta T_f = 109.4\,\mathrm{K}$ run of Fig. 4.13. Arrow indicates the estimated location of x_t.

The measured temperatures after the flame tip decrease at an increasing rate with increasing ΔT_f. The variation in the slope of the data in Fig. 4.14 beyond the flame tip from the lowest ΔT_f to the highest is roughly 0 to $-1/3$. This indicates that the jet is in transition between the momentum-dominated and the buoyancy-dominated regime with increasing ΔT_f. This allows us to conclude that the experiments of Sec. 4.1 were free of buoyancy effects; the measurements are free of this temperature decay.

The transition to the buoyancy-dominated regime in Fig. 4.13 was identified

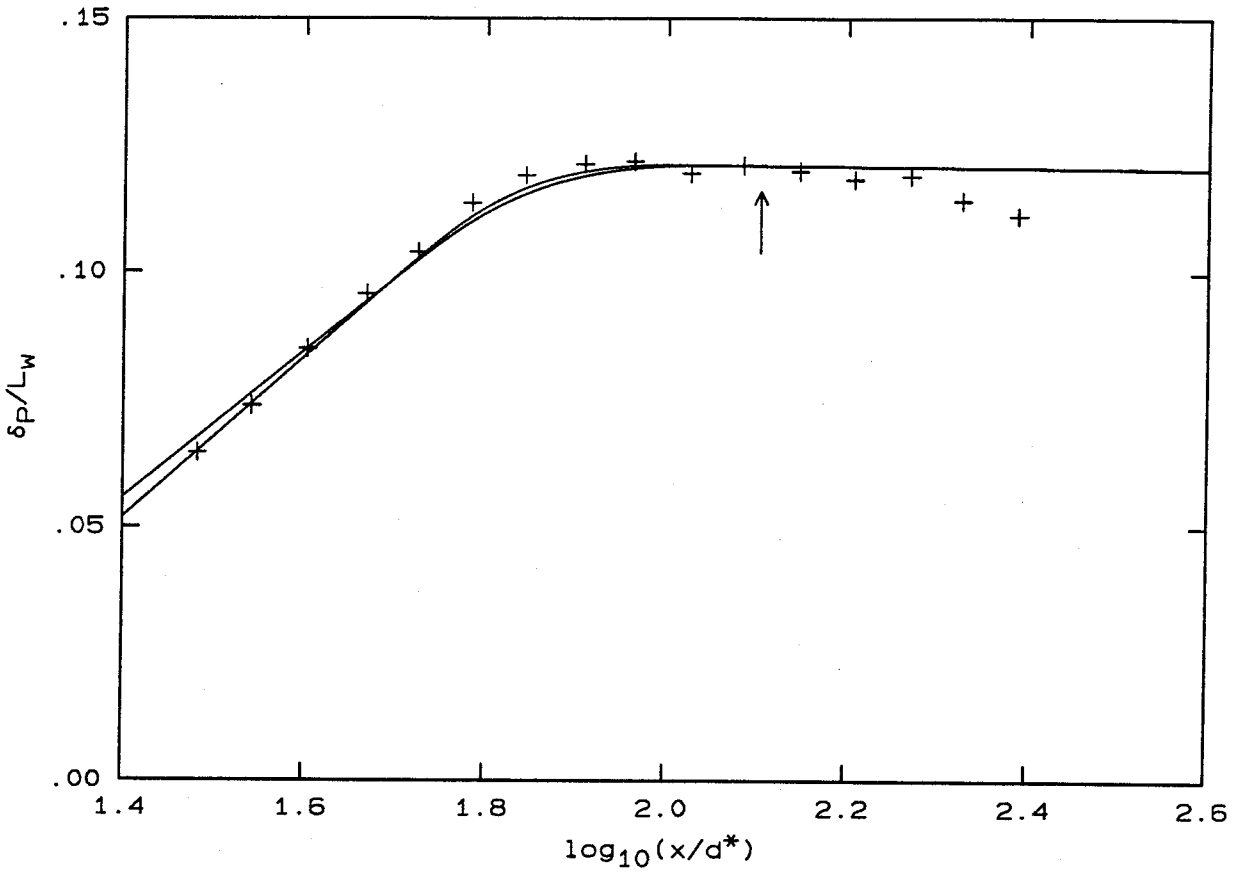

FIG. 4.16 Plot used to determine x_t for the $\Delta T_f = 27.6\,\mathrm{K}$ run of Fig. 4.13. Arrow indicates the estimated location of x_t.

as the point where the temperature measurements departed from the lowest ΔT_f runs that were momentum-dominated. By plotting the curve fits of the two runs with $\Delta T_f = 3.5$ and $6.9\,\mathrm{K}$ with the data of the other ΔT_f runs individually, the transition location x_t for each ΔT_f was determined. Figures 4.15 and 4.16 demonstrate the method with the transition value indicated. The error of this determination of x_t was estimated by considering the location of the closest wire and the character of the departure. Some of the runs showed a more distinct departure from the reference curves than others. The reader is invited to sight along these curves to assess the choices for x_t.

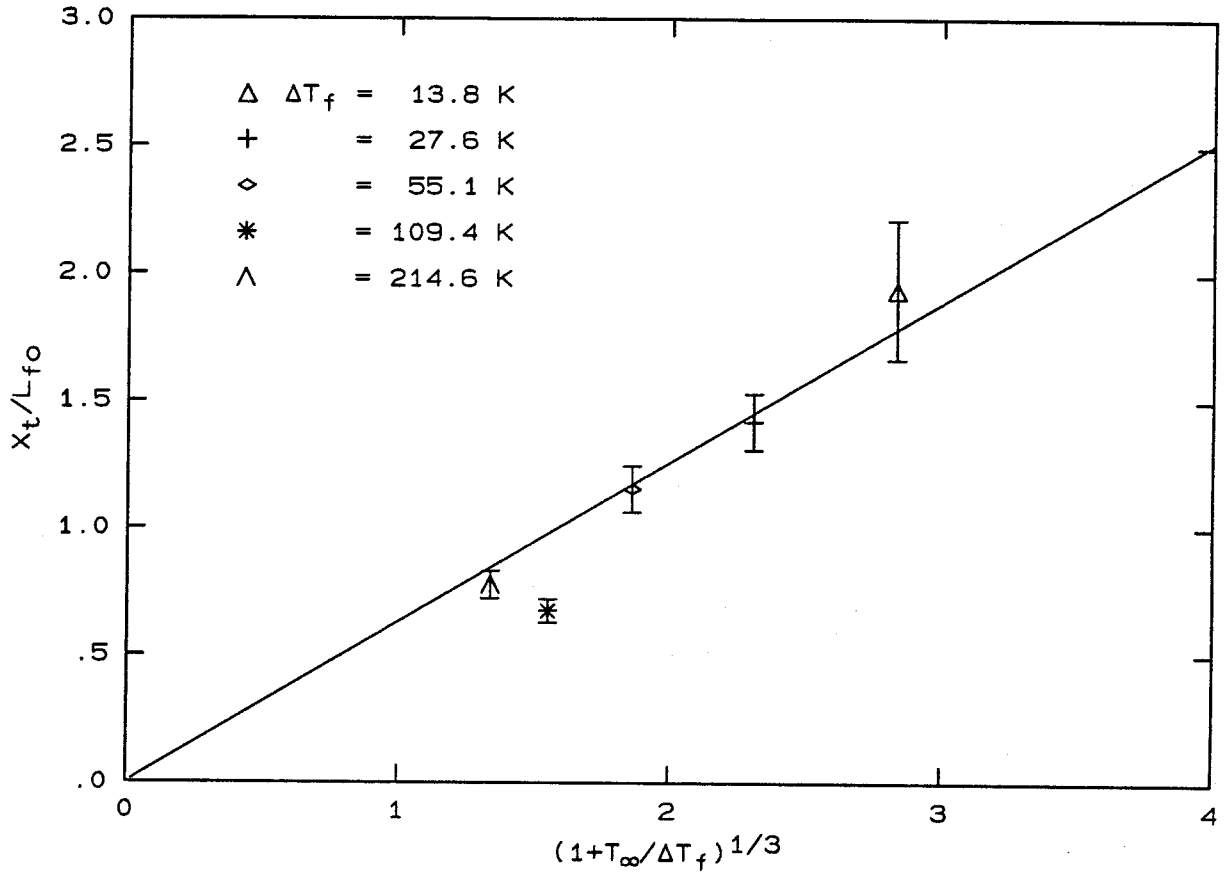

FIG. 4.17 Values of x_t, determined from Fig. 4.13, normalized by L_{f_o} for several adiabatic flame temperatures, $\phi = 10$, $U_0 = 62.4\,\mathrm{m/s}$, $p = 4\,\mathrm{atm}$. Bars represent the uncertainty of the x_t estimate.

To determine the value of ξ that corresponds to x_t, which we will call ξ_t, Eq. 4.14a will be rewritten as the product of three nondimensional groups, *i.e.*,

$$\xi = \left(\frac{\Delta T_f}{\Delta T_f + T_\infty}\right)^{1/3} \left(\frac{g d_0}{U_0{}^2}\right)^{1/3} \left(\frac{x}{d_0}\right) \quad . \tag{4.14b}$$

Therefore, for constant T_∞, U_0, and d_0, $\xi = \mathrm{fn}(\Delta T_f, x)$. Note that there is no distinction in ξ as to whether x_t is in the flame zone, or beyond the flame tip. The flame length was incorporated in Eq. 4.14b to investigate whether the functional dependence of ξ on ΔT_f and U_0 changes depending on whether x_t is less than or

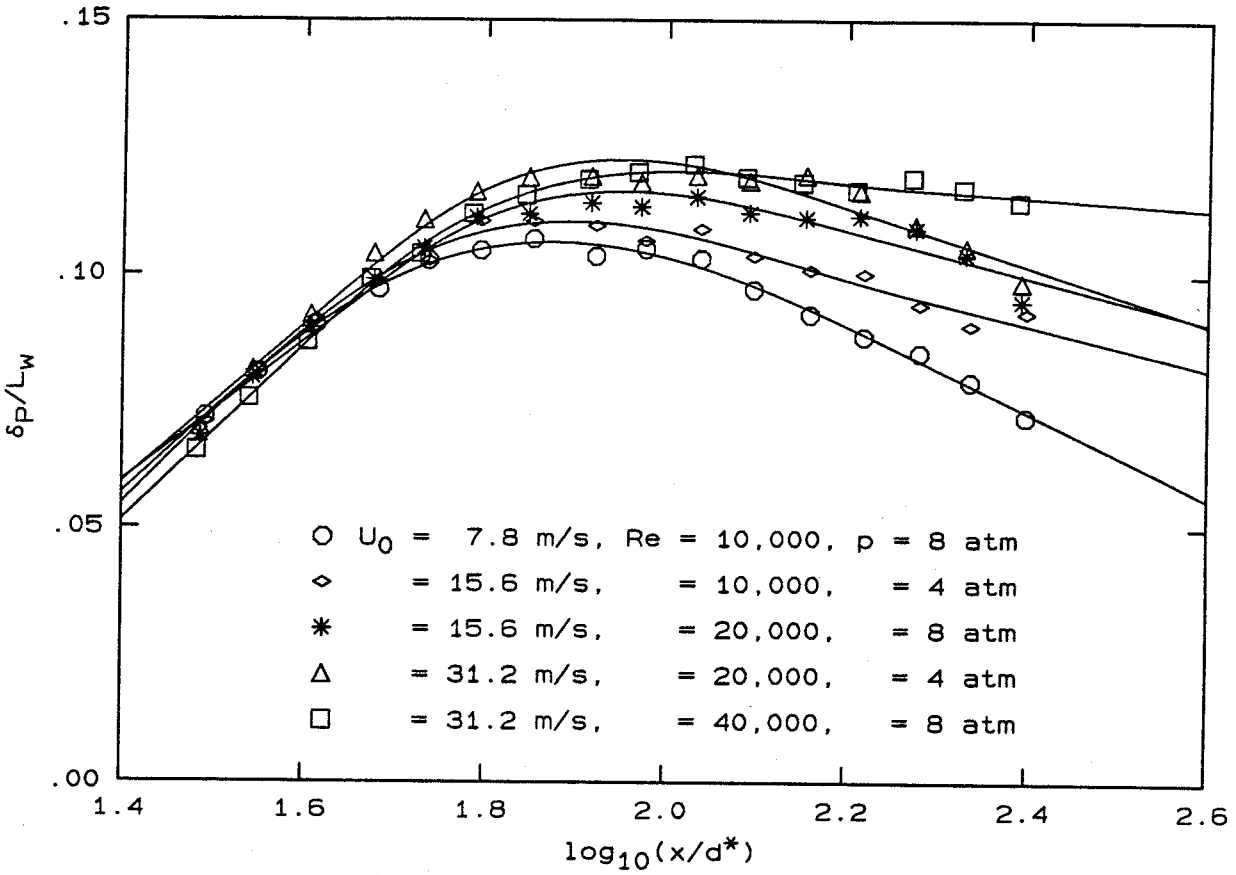

FIG. 4.18 Normalized product thickness versus $\log_{10}(x/d^*)$ for several exit velocities, $\phi = 10$, $\Delta T_f = 6.9\,\mathrm{K}$.

greater than L_f. The new formulation is

$$\xi = \left(\frac{\Delta T_f}{\Delta T_f + T_\infty}\right)^{1/3} \left(\frac{g d_0}{{U_0}^2}\right)^{1/3} \left(\frac{x}{L_f}\right) \left(\frac{L_f}{d_0}\right) . \tag{4.14c}$$

Solving for x/L_f gives

$$\frac{x}{L_f} = \xi \left(1 + \frac{T_\infty}{\Delta T_f}\right)^{1/3} \left(\frac{{U_0}^2}{g d_0}\right)^{1/3} \left(\frac{d_0}{L_f}\right) . \tag{4.15}$$

If ξ represents the correct scaling to describe the transition from the momentum-dominated to the buoyancy-dominated regime, one should be able to vary ΔT_f,

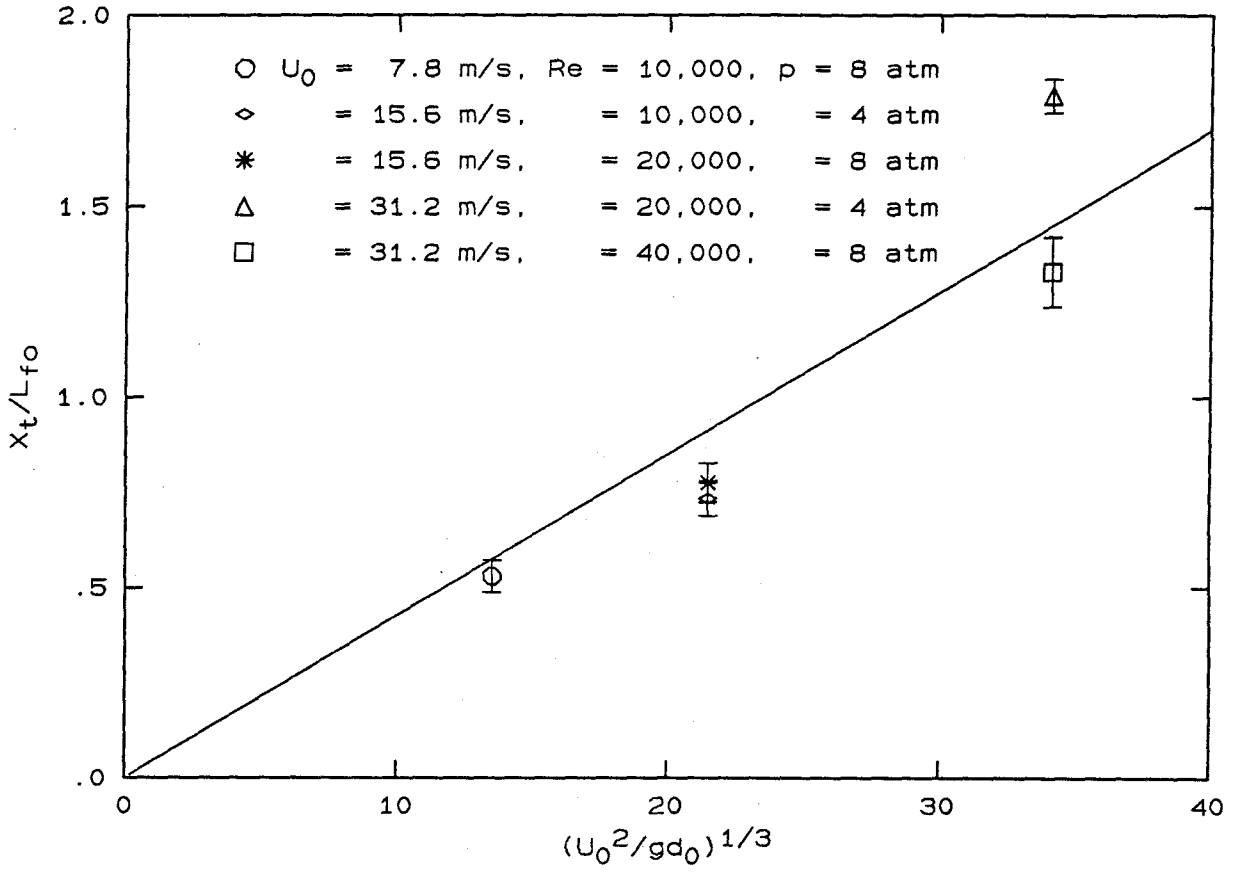

FIG. 4.19 Values of x_t, determined from Fig. 4.18, normalized by L_{f_o} for several exit velocities, $\phi = 10$, $\Delta T_f = 6.9\,\mathrm{K}$. Bars represent the uncertainty of the x_t estimate.

holding T_∞, U_0, and d_0 constant, and calculate a single transition value of ξ_t by substituting the x_t's into Eq. 4.15.

The values of x_t that were estimated from the data plotted in Fig. 4.13 were normalized by L_{f_o}, where L_{f_o} is the value of L_f determined from the curve fit in Fig. 4.6 for each particular Re and ϕ. We can plot x_t/L_{f_o} versus $(1 + T_\infty/\Delta T_f)^{1/3}$ and fit a line though the data, forcing the fit to go through the origin. The slope from the fit represents the coefficient of $(1 + T_\infty/\Delta T_f)^{1/3}$ in Eq. 4.15. Using the known values of U_0, g, d_0, and L_{f_o}, the value of ξ_t can be computed. The x_t data

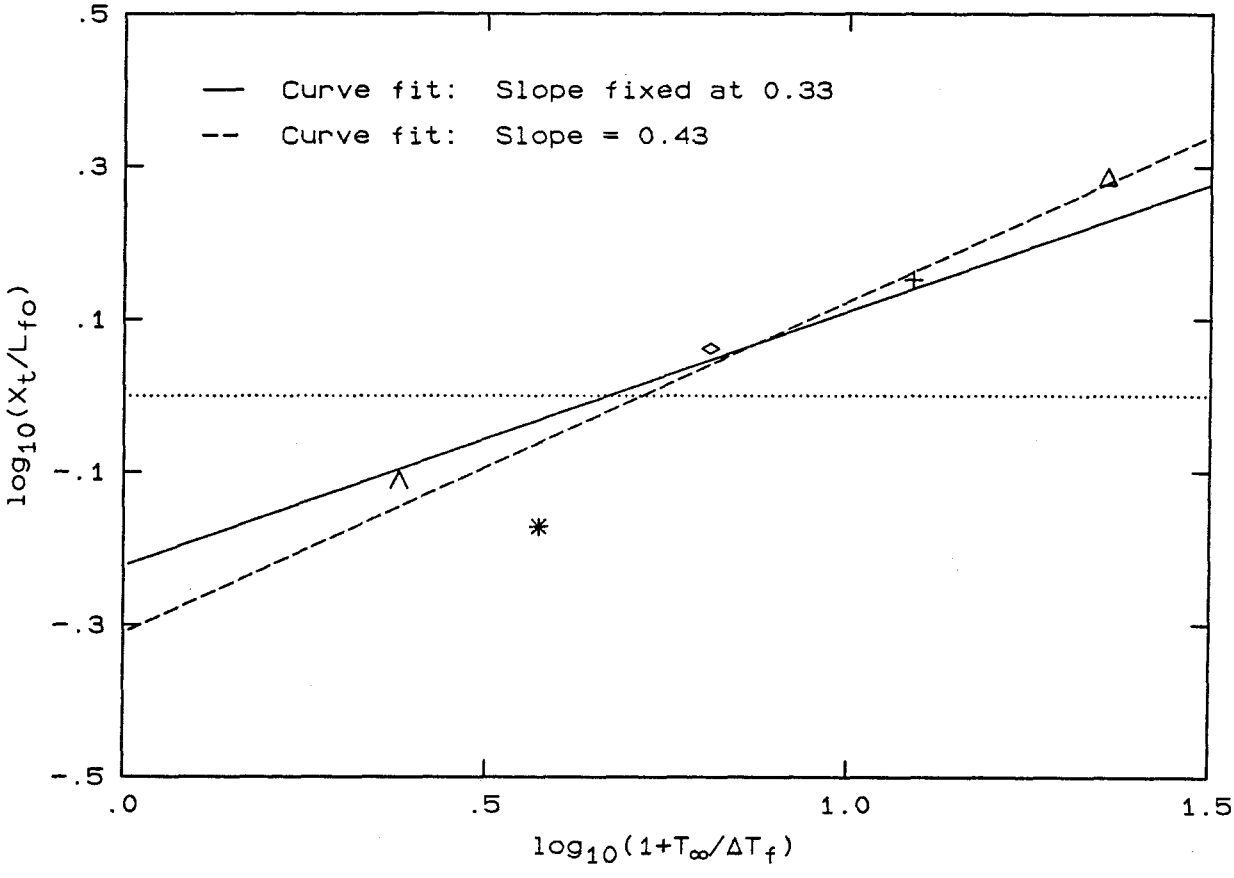

FIG. 4.20 The data of Fig. 4.17 in logarithmic coordinates. The 1/3 slope is included for reference. See Fig. 4.17 for symbol legend.

and the curve fit are shown in Fig. 4.17. The bars indicate the uncertainty of the x_t estimate. The curve fit suggests value of $\xi_t = 0.96 \pm 0.06$.

A similar scan of U_0 was performed holding T_∞, ΔT_f, and d_0 constant. These data are plotted in Fig. 4.18. The collapse for the runs at the same velocity is good in the ramp region, but the data diverge after the flame tip.

The transition locations x_t in Fig. 4.18 were estimated as described above, normalized by L_{f_o}, and plotted versus $(U_0{}^2/gd_0)^{1/3}$ in Fig. 4.19. The curve fit results in a value of $\xi_t = 0.99 \pm 0.13$. This value coincides with the value from

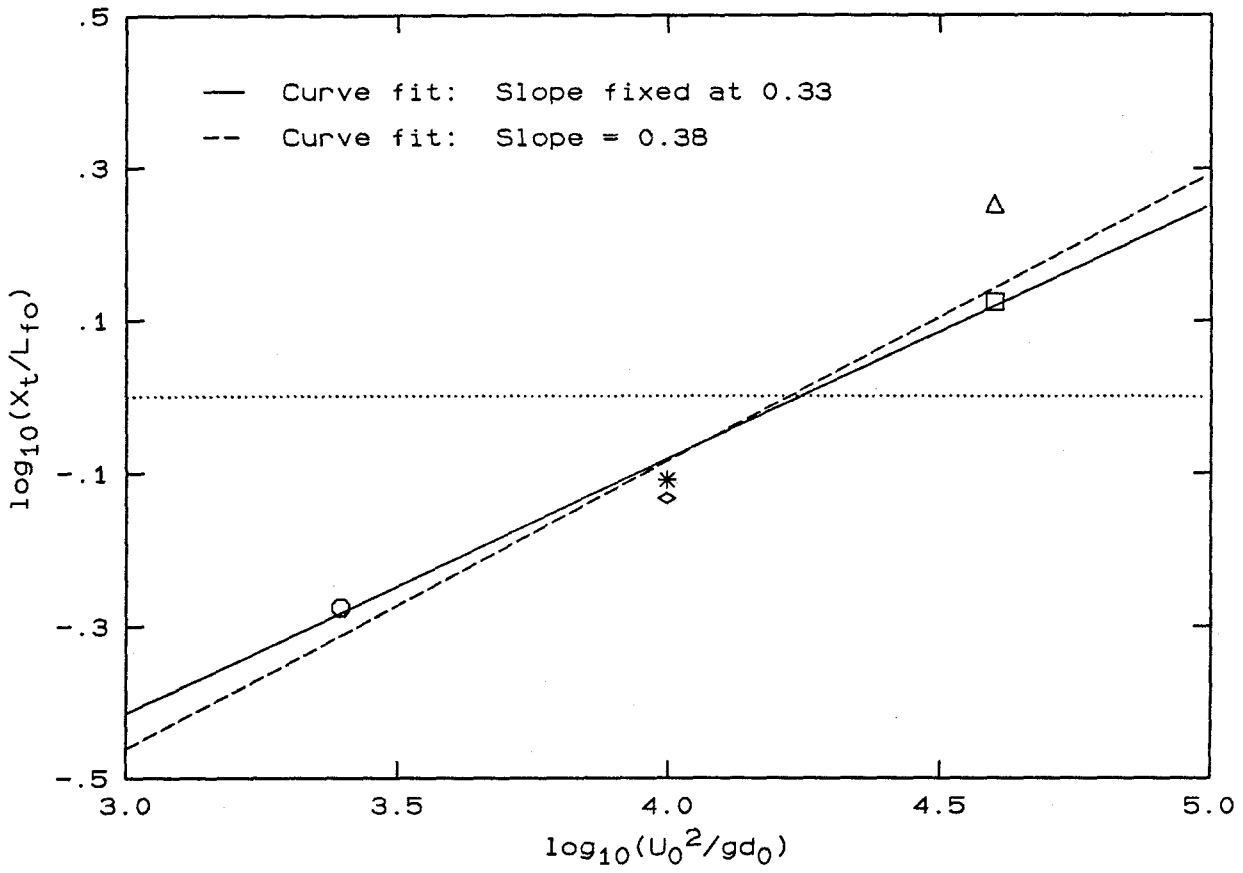

FIG. 4.21 The data of Fig. 4.19 in logarithmic coordinates. The 1/3 slope is included for reference. See Fig. 4.19 for symbol legend.

the ΔT_f scan and also with the observed values reported by Becker & Yamazaki and Toner, discussed above.

Finally, the normalized x_t's were plotted in the appropriate log-log coordinates in Figs. 4.20 and 4.21 to check the power law scaling of Eq. 4.15, and to see if there is any change in the power law for $x_t < L_{f_o}$. The slope of the curve fits for both are close to the 1/3 power law of Eq. 4.15. The reference line is the curve fit with the slope fixed at 1/3. In these coordinates, $x_t < L_{f_o}$ corresponds to negative values of $\log_{10}(x_t/L_{f_o})$.

We appreciate that the ξ-scaling described above cannot be expected to serve as the correct description for $x_t < L_f$. These data were presented here as a first effort to ascertain that the Reynolds number study was conducted in the momentum-dominated flow regime, to provide a direct assessment of buoyancy effects, and to investigate the role of the various nondimensional groups. The issue of buoyancy in turbulent jet flows is not closed, by any means, and more experiments designed for this purpose are needed for a complete documentation of this important phenomenon.

4.3 Kinetics

As noted earlier, the F_2/NO chemistry in this study can be described by the "effective" reaction:

$$2\,NO + F_2 \rightarrow 2\,NOF, \qquad \Delta Q = -75\,\frac{\text{kcal}}{\text{mole}\,F_2}. \tag{4.16}$$

The reaction actually consists of two chain reactions of differing rates and heats of reaction given by

$$NO + F_2 \xrightarrow{k_1} NOF + F, \qquad \Delta Q = -18\,\frac{\text{kcal}}{\text{mole}}, \tag{4.17a}$$

with

$$k_1 \approx 4.2 \times 10^{11} \exp\left(\frac{-2285}{R_u T}\right) \frac{\text{cc}}{\text{mole} \cdot \text{sec}},$$

where R_u is the universal gas constant and T is the temperature of the reaction. The second reaction is given by

$$F + NO + M \xrightarrow{k_2} NOF + M, \qquad \Delta Q = -57\,\frac{\text{kcal}}{\text{mole}}, \tag{4.17b}$$

with

$$k_2 \approx 3 \times 10^{16}\,\frac{\text{cm}^6}{\text{mole}^2 \cdot \text{sec}}.$$

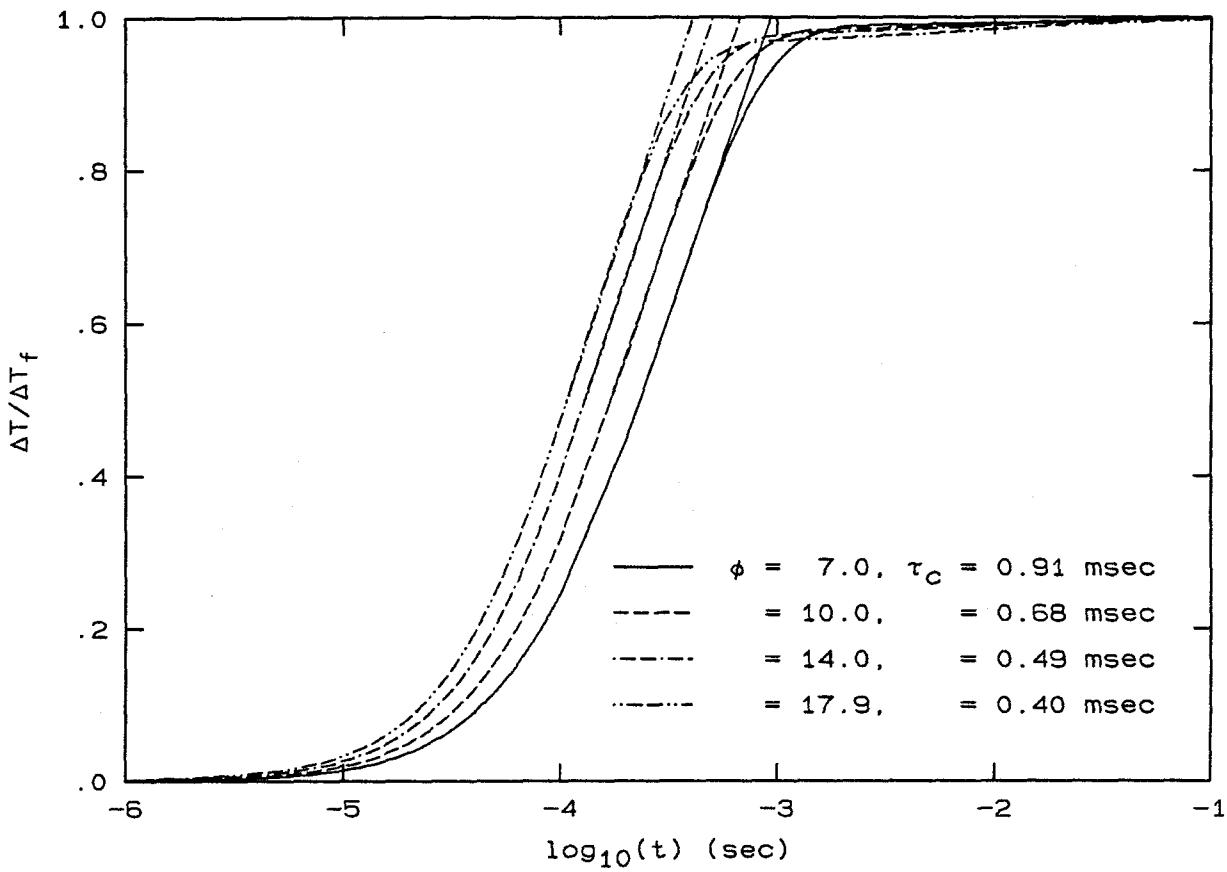

FIG. 4.22 Chemical reaction times for some of the runs of Sec. 4.1, $p = 1\,\mathrm{atm}$, $T = 293\,\mathrm{K}$. See Table 4.1 for corresponding mass fractions.

There is also one recombination reaction given by

$$\mathrm{F} + \mathrm{F} + \mathrm{M} \overset{k_3}{\rightarrow} \mathrm{F}_2 + \mathrm{M}, \qquad \Delta Q = -38\,\frac{\mathrm{kcal}}{\mathrm{mole}}\,, \tag{4.18}$$

with

$$k_3 \approx 3.2 \times 10^{14}\,\frac{\mathrm{cm}^6}{\mathrm{mole}^2 \cdot \mathrm{sec}}\,.$$

The third body M in the reactions denotes any chemical species present in the reacting mixture. The reaction rates k_i and the heats of reaction ΔQ were taken from Baulch *et al.* (1981).

To estimate the chemical reaction time τ_c, these reactions were investigated using the CHEMKIN chemical kinetics software package (Kee *et al.* 1980) with a constant mass, constant pressure reactor. Figure 4.22 shows a sample result from the program for the mass fractions corresponding to the four ϕ's used in Sec. 4.1. The reaction time τ_c was determined by drawing a tangent to the curve at its steepest point and using the intersection of this tangent line with the adiabatic flame temperature as the chemical time. The slowest rate is for $\phi = 7$, $p = 1\,\mathrm{atm}$ with $\tau_c = 0.91\,\mathrm{msec}$.

As mentioned earlier, it was required that the time lag between molecular mixing and chemical product formation be negligible. For this mixing-limited condition, which we will designate as the fast chemistry regime, there is a one-to-one correspondence between molecular mixing and product formation. The ratio of the local large-scale passage time to the chemical reaction time is one way of estimating when the reacting flow is in the fast chemistry regime. This ratio is the Dahmköhler number given by

$$Da = \frac{\tau_\delta}{\tau_c} \quad , \tag{4.19}$$

where τ_δ is the local large-scale passage time, estimated by dividing the local jet diameter $\delta(x)$ by the mean centerline velocity U_{cl}

$$\tau_\delta = \frac{\delta(x)}{U_{cl}} \quad , \tag{4.20}$$

and τ_c is the chemical reaction time, computed as described above. The local jet diameter $\delta(x)$ for a turbulent jet has been measured by many experimenters (*e.g.*, White 1974; Dowling 1988) and can be approximated by

$$\delta(x) \approx 0.44\,x \ . \tag{4.21}$$

An estimate of U_{cl} is given for a momentum-dominated, density-matched jet by

Chen & Rodi (1980) as

$$U_{\rm cl} = 6.2\,U_0 \left(\frac{x - x_0}{d_0}\right)^{-1} \quad . \tag{4.22}$$

The jet exit diameter d_0 in the above formula should actually be replaced by d^*, the momentum diameter of the jet, but for a properly designed nozzle with density-matched jet and reservoir gases, $d^* \approx d_0$ (see Sec. 2.2). In the limit of fast chemistry ($Da \gg 1$), chemical product formation is equivalent to molecular mixing. The lowest Da of the runs in Sec. 4.1 occurs at $x/d^* = 30$ for the $\phi = 7$ run of Fig. 4.22, with a corresponding Dahmköhler number of $Da = 2.8$.

Since U_0 is constant for the Reynolds number experiments described in Sec. 4.1, and the spreading rate of the jet is assumed to be constant, τ_δ for a given x/d^* is the same for all of the current experiments in Sec. 4.1. The chemical time $\tau_{\rm c}$ decreases with reactant number density (*i.e.*, pressure). This means that, for the experiments described in Sec. 4.1, the numerator in Eq. 4.19 remains constant and the denominator is decreasing with increasing Reynolds number. Therefore, demonstrating fast chemistry for the lowest Reynolds number runs guarantees that the higher Reynolds number experiments of Sec. 4.1 are in the fast chemistry regime.

One way of determining if a run is in the fast chemistry regime is to repeat the experiment, doubling the concentrations of both jet and reservoir fluids. This doubles the adiabatic flame temperature. The kinetic rate is proportional to reactant number density and also exponentially dependent on the reaction temperature. Therefore, a concentration doubling increases the kinetic rate through higher reactant concentrations and by increasing the reaction temperature. The temperature rise for the higher concentration run should double, if the chemical product formation is already mixing-limited. If the chemistry was not fast before the concentration doubling, the faster kinetic rate after the doubling should result in more than double the chemical product and, correspondingly, more than double the temperature

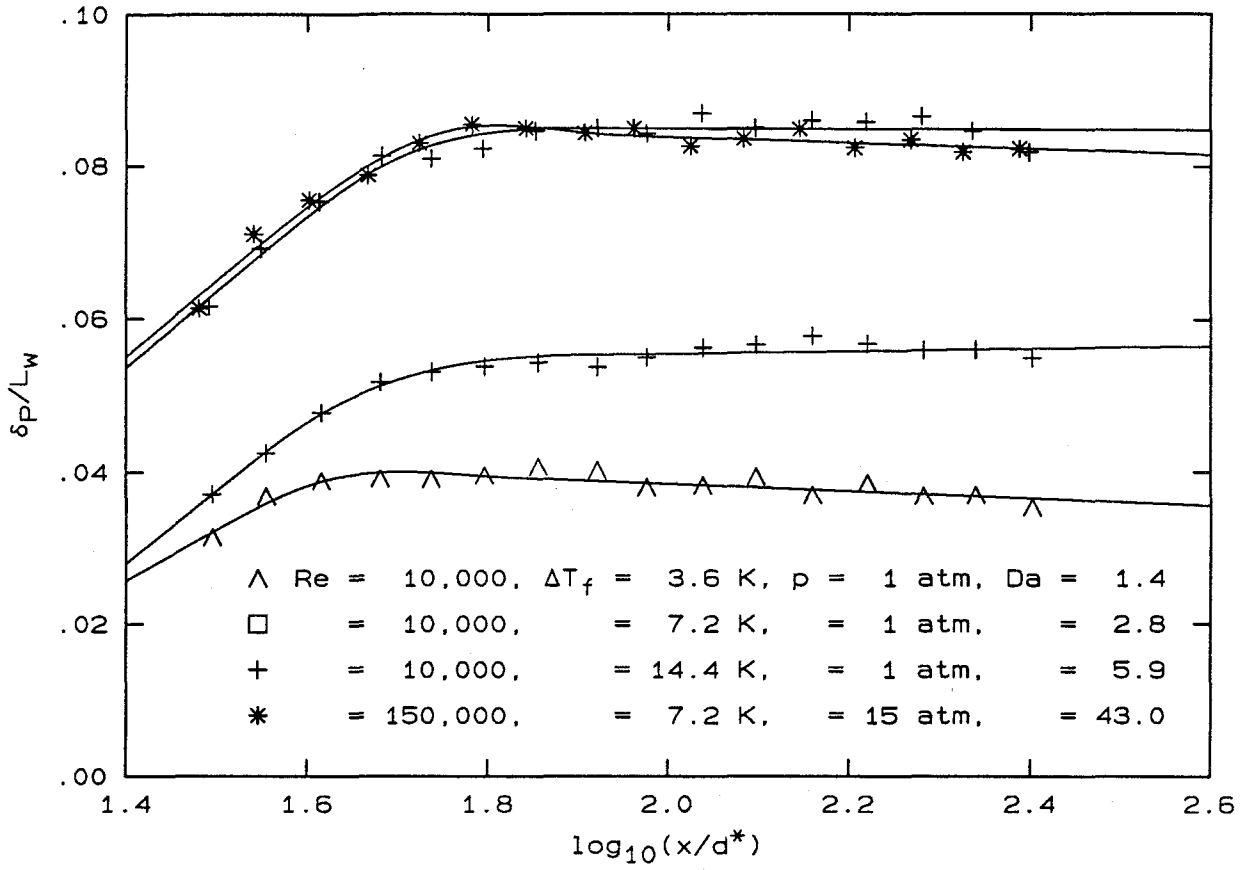

FIG. 4.23 Temperature doubling to check kinetic rate, $\phi = 7$, $U_0 = 62.4\,\mathrm{m/s}$. Dahmköhler number is given for $x/d^* = 30$.

rise. Note that the Dahmköhler numbers at $x/d^* = 30$ in Fig. 4.13 are in the range of $7.8 \leq Da \leq 1.1x10^3$, yet the collapse of the data within the ramp region is excellent, indicating that $Da \geq 7.8$ is in the fast chemistry regime.

A similar temperature doubling was performed for the run in Sec. 4.1 with the lowest Dahmköhler number, shown in Fig. 4.23. These data do not collapse. Slow chemistry should only affect the ramp region of the curve and possibly result in a longer flame length. The asymptotic level, however, should eventually agree at some downstream location because all of the F_2 should react if one goes far enough

downstream. The asymptotic level does not agree for the various ΔT_f's. This raised the suspicion that the reactant concentrations were somehow affected.

Conceivable inaccuracies in the loading procedures could not account for such a large drop in the asymptotic level. Some other mechanism for affecting the concentrations had to be responsible. The fact that the asymptotic level nearly doubles for each temperature doubling lead to the hypothesis that some of the F_2 was being depleted by passivation of the nozzle plenum screens and honeycomb during each run. Passivation is a term commonly used in fluorine systems. It refers to the process of admitting low concentrations of F_2 into the previously unexposed metal surfaces in a new flow system to allow oxidation of the metal by the fluorine. The oxidation layer provides a protective coating on the metal surface which resists further corrosion by subsequent exposure of fluorine. The $\phi = 7$, $\Delta T_f = 7.2\,\mathrm{K}$ run at 1 atm has the lowest concentrations of F_2 and NO of all the runs in Sec. 4.1. This, along with the fact that this run is also at the lowest pressure, results in the lowest reactant partial pressures and therefore the least absolute number of moles of each reactant. The nozzle is inside the HPRV and therefore sees NO during the loading process before the run. The NO reacts with the F_2 passivation layer in the plenum requiring re-passivation from the F_2 in the jet gas during the run. Assuming the depletion rate is constant, the effect would be most pronounced when the absolute molar amount of F_2 is lowest, as is the case for the runs in question. At low concentrations, doubling the absolute number of moles of F_2 by doubling the concentrations should cut the passivation effect in half. This appears to be what is happening in Fig. 4.23, supporting the passivation hypothesis.

The kinetics and the passivation problems disappear for the run with $\Delta T_f = 14.4\,\mathrm{K}$ in Fig. 4.23, as demonstrated by the collapse of the data with the higher Reynolds number run that should be in the fast chemistry regime. For this reason, the run in Fig. 4.1 at 1 atm was done at double the adiabatic flame temperature.

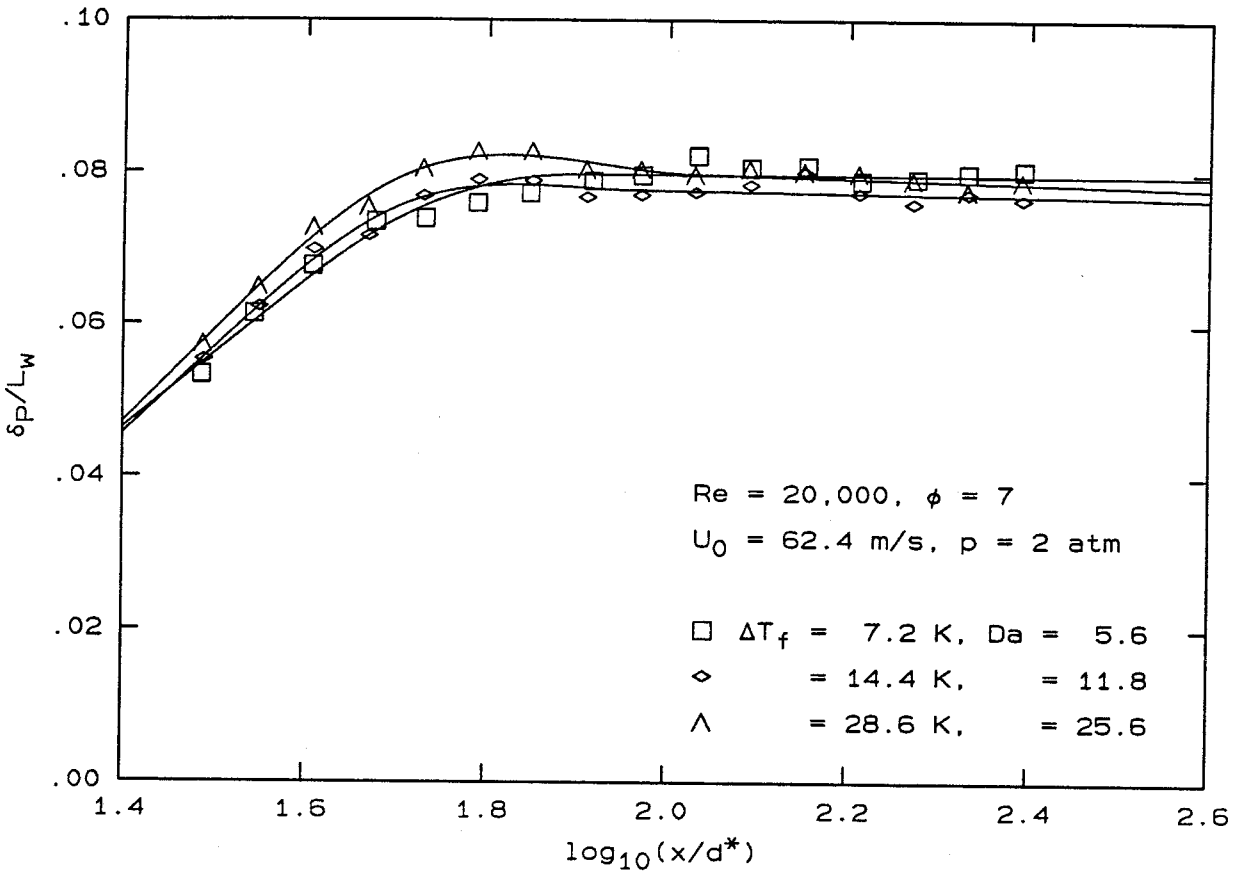

FIG. 4.24 Temperature doubling to check kinetic rate. Dahmköhler number is given for $x/d^* = 30$.

The collapse of the data in Figs. 4.1, 4.2, 4.3, and 4.4 indicate that all the runs of Sec. 4.1 are in the fast chemistry regime and free of passivation problems. Figure 4.12 also proves that the run at the higher $\Delta T_f = 14.4\,\mathrm{K}$ was still momentum-dominated because the temperature measurement beyond the flame tip remains nearly constant.

Figure 4.24 shows the result of a similar experiment at $p = 2\,\mathrm{atm}$ with two temperature doublings. The collapse is good and this condition appears to be in the fast chemistry regime with the $\Delta T_f = 7.2\,\mathrm{K}$ run having a $Da = 5.6$.

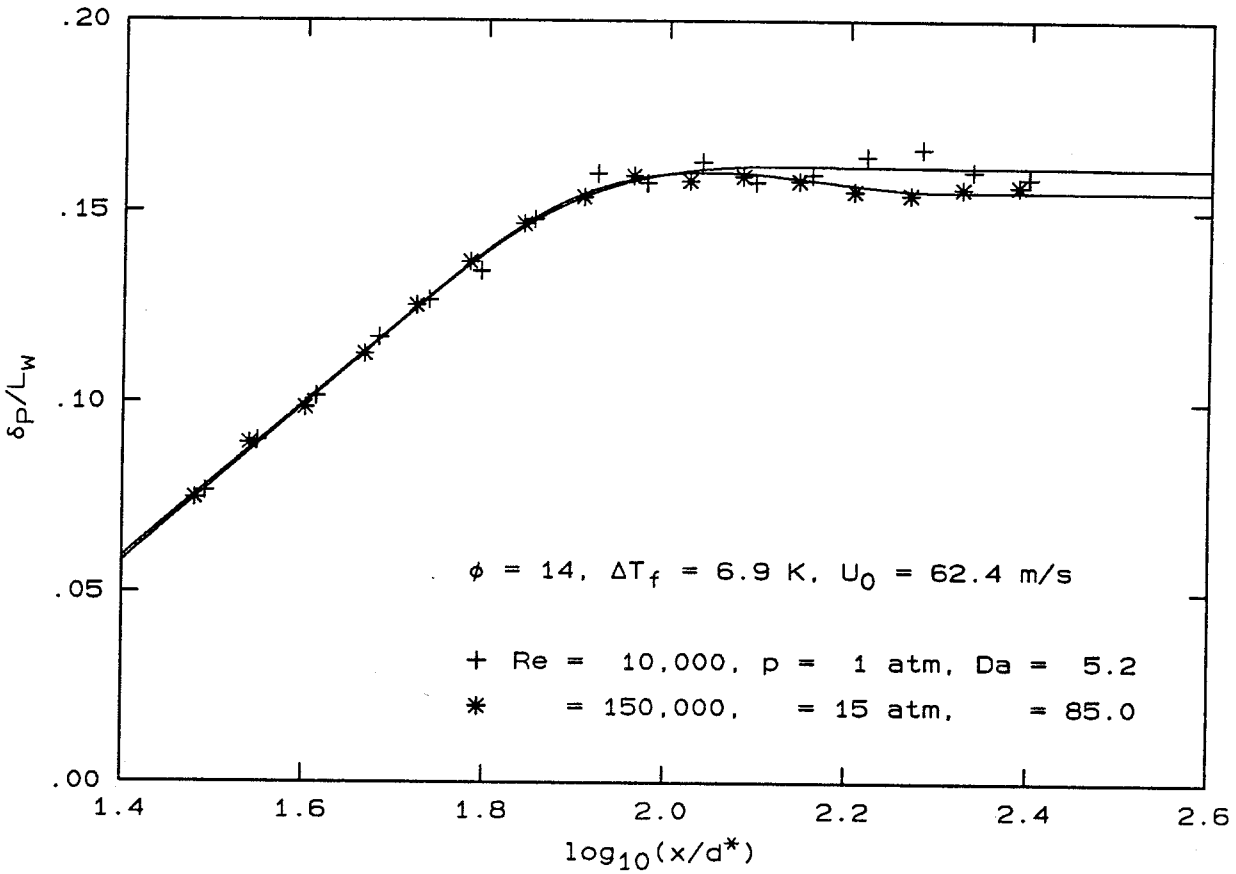

FIG. 4.25 Runs showing the lowest Dahmköhler number that still demonstrates fast chemistry. Da is given for $x/d^* = 30$.

Figure 4.25 compares the run at 1 atm, $\phi = 14$, to the run at 15 atm and the same ϕ and flame temperature. This is the lowest value of the Dahmköhler number in all of the experiments which still collapses well with an experiment at a much larger Dahmköhler number. The lower limit of Dahmköhler number in these experiments, in which the flow can be considered to be in the fast chemistry regime, is therefore $Da \simeq 5.2$.

In the runs described thus far, the Dahmköler number was changed by varying the chemical time, but changing the large-scale passage time τ_δ is another way of

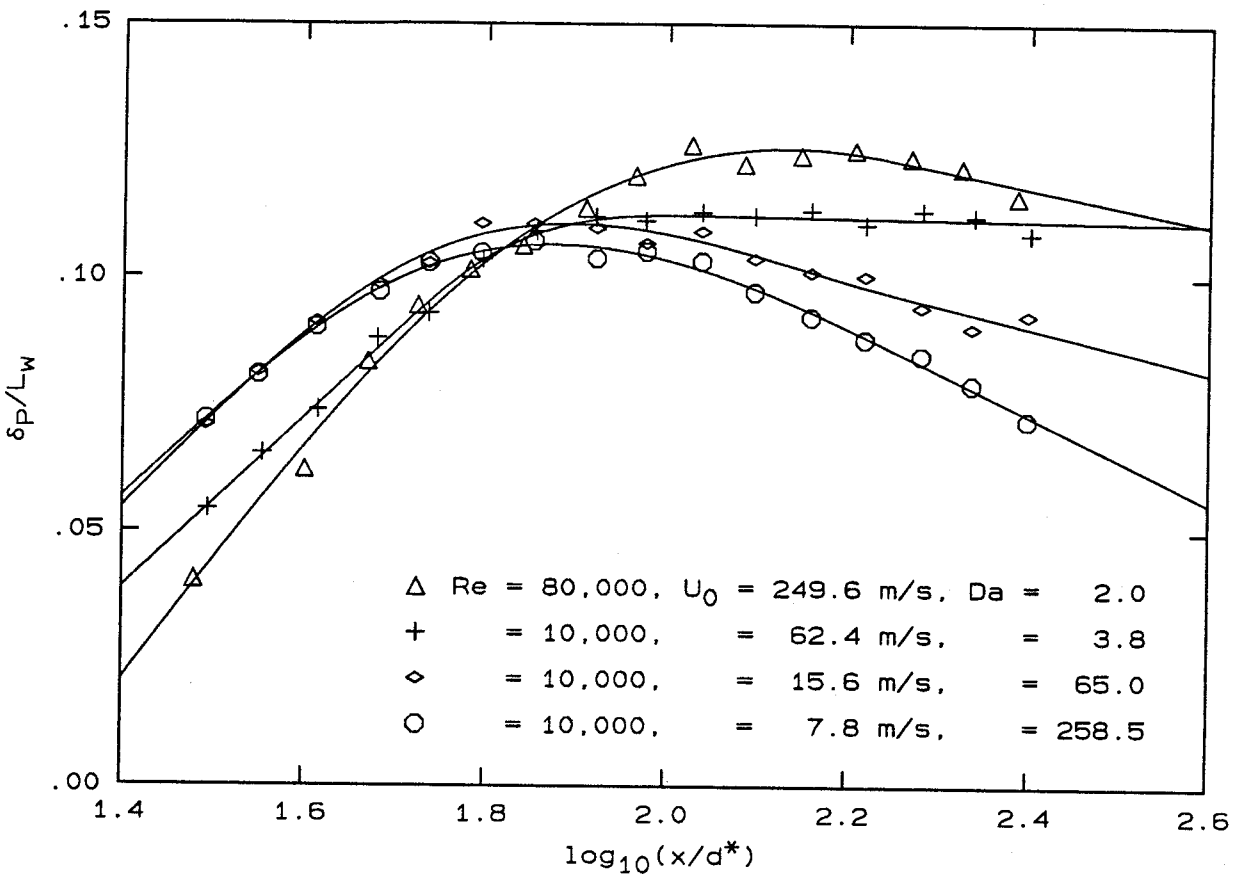

FIG. 4.26 Runs showing the effects of slow chemistry in the ramp region, $\phi = 10$, $\Delta T_f = 6.9\,\mathrm{K}$. Dahmköhler number is given for $x/d^* = 30$.

varying Da. Several runs at different velocities and pressures were performed in which the Dahmköhler number was low but the temperature measurement beyond the flame tip achieved the correct level, showing them to be free of passivation problems. Figure 4.26 shows runs at various velocities and Dahmköhler numbers. The temperatures for the slow chemistry conditions lag behind the fast chemistry runs but eventually achieve the same level beyond the flame tip. This is how slow chemistry was expected to manifest itself. The Dahmköhler numbers are consistent with the limiting value of $Da \simeq 5.2$ discussed above. The lower velocity runs show the effects of buoyancy beyond the flame tip. The high-velocity run is repeatable.

CHAPTER 5

Conclusions

A new high pressure combustion facility has been built to investigate mixing in axisymmetric, gas-phase turbulent jets. The study was aimed at identifying Reynolds number effects on turbulent mixing by examining changes in flame length, which is related to the molecular mixing rate, with increasing Reynolds number. The run parameters were chosen so that the jet remained momentum dominated to the farthest measuring station and that the time lag between molecular mixing and chemical product formation was negligible. The facility uses fluorine and nitric oxide, diluted with nitrogen, to provide a fast, hypergolic chemical reaction with heat release. The average temperature was recorded with a set of long, thin, resistance wire thermometers stretched across the jet centerline at 16 downstream locations ranging from $x/d_0 = 30$ to 240. Runs at several stoichiometric mixture ratios were performed at Reynolds numbers ranging from $10,000 \leq Re \leq 150,000$ to determine the flame length dependence on Reynolds number. The conclusions are summarized below.

1. The time-averaged line integral of temperature performed by the cold wires along the transverse axis of the jet displays a logarithmic dependence on x/d^* within the flame zone. Beyond the flame tip, this integral asymptotes to a constant value, as predicted from the scaling and similarity laws for a momentum-dominated jet.

The following two conclusions represent the major findings of this investigation, namely that flame length L_f is a function of Reynolds number.

2. Runs at several stoichiometric mixture ratios for increasing Reynolds numbers indicate that the normalized flame length L_f/d^* displays a linear dependence on ϕ, and that the slope A of the linear fit decreases from $Re = 10,000$ to 20,000. Dowling & Dimotakis (1990) observed a similar decrease in their concentration measurements of the same magnitude over a similar Reynolds number range. The slope then remains constant with a value of $A = 5.6$ for $20,000 \leq Re \leq 150,000$. This threshold Reynolds number of 20,000 is close to the value of $Re = 25,000$ found by Ricou & Spalding (1961), where their entrainment measurements became independent of Reynolds number.

3. The flame length measurements revealed the existence of a "mixing virtual origin" L_0, defined as the far-field flame length extrapolated to $\phi = 0$. Alternatively stated, L_0 is the flame length that would result in the limit of $\phi \rightarrow 0$ if the flow could be described by its far-field behavior at the nozzle exit. This L_0 has a nonzero value that increases up to $Re = 20,000$ and then decreases up to the highest Reynolds number investigated in the experiments reported here, *i.e.*, $Re = 150,000$.

4. Experiments to determine the parameter range where the jet is momentum-dominated were performed and it was demonstrated that the conclusions above were based on runs that were in the momentum-dominated regime.

5. Experiments to identify the location x_t where the transition to the buoyancy-dominated regime occurs indicate that the nondimensional downstream buoyancy coordinate ξ works reasonably well in describing this point for a variety of run conditions, for $x_t > L_f$. The transition value was found to be $\xi_t \simeq 1$. This value agrees with Becker & Yamazaki (1978) and Toner (1987), who used entrainment measurements to determine the transition location.

6. The chemical reaction in the jet was found to be in the fast chemistry regime for $Da > 5.2$. All of the runs on which the above conclusions were based were shown to be in the fast chemistry regime.

APPENDIX A

Experimental design and run parameters

The High Pressure Combustion Facility (HPCF) was designed to perform jet mixing experiments over a pressure range of 0.1 atm to 15 atm using both conventional fuels and more exotic reactants such as fluorine, nitric oxide, and hydrogen. The lab building is a 4.57 m by 5.79 m (15 ft by 19 ft) extension to the HF Shear Layer Combustion Facility. The list of desired run parameters, shown in Table A.1, determined much of the design of the facility. The following sections give brief descriptions of the major experimental items with some of the motivating factors and a short description of the run parameters and procedures.

A.1 High Pressure Reactant Vessel (HPRV)

The tank specifications, shown in Table A.2, resulted from many constraints. The diameter was determined by the requirement of low recirculation velocity of a confined jet ($U_r \leq 2\%$ of U_{cl} at $x/d_0 = 240$) and the height was set to be one half of the floor to ceiling height. The windows are positioned 10.16 cm (4 in.) above the vessel centerline to maximize the jet axial station that can be viewed. There are 44 internal stainless steel tabs for use in supporting internal hardware. Fluorine is extremely corrosive so the choice of tank materials was either stainless steel or mild steel with a teflon coating. Stainless steel was cost prohibitive so the tank was made of mild steel with an internal coating of 127 μm (.005 in.) thick, pinhole-free PFA teflon, which has a maximum operating temperature of 644 K. The tank is mounted with the base supported 1.22 m (4 ft) above the floor and the top 0.61 m (2 ft) from the ceiling (see Fig. 2.2). This allows the lower head to be dropped down

Table A.1: High Pressure Combustion Facility Target Specifications

ITEM	DESCRIPTION
Reservoir	
• Reactant Gases	H_2, NO, air
• Diluent Gases	N_2, Ar, He
• Temperature Range (w/o liner)	$300\,\mathrm{K} < T < 644\,\mathrm{K}$
• Temperature Range (w/ liner)	$300\,\mathrm{K} < T < 2,500\,\mathrm{K}$
• Concentration Range (molar)	$0 < C_{\mathrm{H_2,NO}} < 8\%$
Jet	
• Reactant Gases	F_2, hydrocarbons
• Diluent Gases	N_2, Ar, He
• Temperature Range (unreacted)	Ambient ($300\,\mathrm{K}$)
• Nozzle Exit Diameter	$2.5\,\mathrm{mm}$
• Maximum Mass Flow Rate	$0.01\,\mathrm{kg/s}$ (N_2)
• Gas Delivery Method	Expulsion Diaphragm
• Concentration Range (molar)	$0 < C_{\mathrm{F_2}} < 40\%$
Overall	
• Maximum Run Time	68 seconds (At $U_0 = 125\,\mathrm{m/s}$)
• Reynolds Number Range	$1,000 < Re < 150,000$ (nominal)
• Pressure Range	$0.1\,\mathrm{atm} < p < 15\,\mathrm{atm}$
• Flame Temperature (F_2/NO)	$3.5\,\mathrm{K} < \Delta T_f < 215\,\mathrm{K}$
• Flame Temperature (Hydrocarbons)	$\Delta T_f \sim 2500\,\mathrm{K}$

Table A.2: High Pressure Reactant Vessel Specifications

Manufacturer:	California Tank and Manufacturing Corporation
Serial No. :	21274
Year Built :	1985
Working Pressure @ Temp:	full vacuum to 15 atm @ 422 K
Hydrostatic Test Pressure:	21.4 atm
Material :	SA-455-75 steel (shell and both caps)
Thickness :	9.525 mm (0.375 in.) (shell and caps)
Overall Length :	183 cm (72 in.) (does not include welding neck flanges)
Nominal O.D. :	107 cm (42 in.)
Caps :	91.44 cm (36 in.) crown radius;
	8.89 cm (3.5 in.) knuckle radius
Internal Capacity :	1.43 m^3 (50.8 ft^3)
Overall Empty Weight:	2,268 kg (5000 lbs) approx.
Openings :	8 ea - 7.62 cm (3 in.) welding neck flanges (cap)
	2 ea - 15.24 cm (6 in.) welding neck flanges (cap)
	8 ea - 7.62 cm (3 in.) welding neck flanges (shell)
	4 ea - 3.81 cm (1.5 in.) welding neck flanges (shell)
	1 ea - 40.64 cm (16 in.) manhole
	3 ea - 25.4 cm (10 in.) diameter windows (shell)
Notes :	Internal 127 μm (0.005 in.) PFA, pinhole-free
	teflon coating applied by Thermech Engineering.

and the upper head to be lifted free of the shell giving full interior access. With this arrangement, the tank windows are located 2.13 m (7 ft) above the floor, a desirable safety feature in case of window blowout and for future laser beam access.

A.2 Fluorine Reactant Tank

The jet gas is contained in a stainless steel reactant tank with an internal volume of $0.042\,\mathrm{m}^3$ ($1.48\,\mathrm{ft}^3$). A teflon expulsion diaphragm separates the jet charge from the inert driver gas. The reactant tank is internally lined with stainless steel screen, both to support the diaphragm over the inlet and exit ports, and to provide a gas path to prevent trapped pockets of gas during evacuation and expulsion. The reactant tank is located underneath the HPRV to minimize the length of the delivery line to the nozzle, resulting in the shortest possible startup times ($\sim 0.8\,\mathrm{sec}$).

The teflon expulsion diaphragms were fabricated at Thermech Engineering of Anaheim from a highly polished, hard-chrome plated male mold made at Caltech's Central Engineering Services. The process involves charging the mold with a static charge, spraying it with a layer of PFA teflon powder, and then baking it in an oven at 700 K until the powder melts and flows to form a smooth layer approximately $76\,\mu\mathrm{m}$ (0.003 in.) thick. The process is repeated until the desired thickness of $203\,\mu\mathrm{m}$ (0.008 in.) is obtained. The diaphragm was periodically inspected after a number of runs and replaced when necessary.

A.3 Gas Delivery and Exhaust

Designing a gas delivery system to handle F_2 and NO gases involved many special design features. Fluorine is extremely reactive while NO, in the absence of water vapor or oxidizers, is fairly inert. Both gases are toxic with potentially lethal concentrations as low as 1 ppm, necessitating a gas-tight environment. The issue of safety required that all exposed surfaces be well cleaned and the gas paths kept leak-tight and free of water vapor. To ensure cleanliness, the F_2 reactant tank was nitric acid pickled, the F_2 mixing vessels were electropolished, and the NO mixing vessels were clear anodized prior to installation. Before any runs were performed, the gas lines, the HPRV, the F_2 reactant tank, and the mixing vessels were cleaned with an M-17 degreaser, purged with dry nitrogen, sealed, and evacuated. The F_2 lines and F_2 reactant tank were then exposed to low concentrations of F_2 for a period of time (typically 2 hours) to build up a fluorine passivation layer on the metal surfaces. The entire system was helium leak-checked with a Matheson helium leak detector (10^{-5} cc/min resolution). To ensure that no atmospheric water vapor enters, the system is always kept at some positive gauge pressure with dry nitrogen. To remove any contaminants or water vapor that could be present in the gas supply, all the nitrogen used in the experiment was passed through Robbins Aviation 13X molecular sieves.

The reactive nature of F_2 limited the choice of materials for the F_2 delivery system. Virtually all of the gas tubing and valves for the F_2 gas system are stainless steel because of its high corrosion resistance. The F_2 mixing vessels are 316L stainless steel with removable flanges sealed with lead gaskets. Although NO is not as reactive as F_2, the gas tubing and valves for the NO delivery system are also stainless steel. The NO mixing vessels are 6061-T6 aluminum with removable flanges sealed with Viton O-rings.

The dynamic pressure of the nozzle for the entire range of experiments varied

from 2 torr to 500 torr. To maximize the resolution of this pressure measurement, three Barocel differential pressure transducers of ranges 10, 100, and 1000 torr were available. The dynamic pressure of the run determined which of the three transducers would be used to obtain the best resolution.

There are three distinct exhaust systems for the facility. The first is a Camflex relief valve installed on the HPRV to relieve any pressure rises that occur during runs at pressures $\geq 1\,\mathrm{atm}$. The exhaust from this valve is plumbed into the downstream catch bag shared with the HF Shear Layer Combustion Facility described in Hall (1991). The bag material is J-22, a vinyl-based polymer that was tested for NaOH and F_2 compatability in the HF Shear Layer Facility. The bag has a capacity of $120\,\mathrm{m}^3$ $(4,238\,\mathrm{ft}^3)$ and is equipped with an internal NaOH and water shower system to neutralize the exhaust products. The second system is a 132-liter (35-gallon) stainless steel barrel filled with NaOH and water. Any unreacted NO in the mixing vessels and by-products left in the HPRV after a run are bubbled through the barrel to neutralize these chemicals. The third is a 208-liter (55-gallon) stainless steel barrel filled with activated charcoal in series with a 132-liter (35-gallon) stainless steel drum filled with NaOH and water. Similarly, the unreacted F_2 in the mixing vessel and reactant tank is passed though the charcoal barrel and bubbled through the NaOH barrel to neutralize the gas (see Fig. 2.1 for a schematic of this system).

Relief of accidental overpressure in the HPRV and the NO mixing vessels is provided by Fike burst diaphragms installed on each vessel. The exhaust from these diaphragms is plumbed into the downstream catch bag. Burst diaphragms are also installed on the F_2 mixing vessels and a relief valve is installed on the F_2 reactant tank, all plumbed to the charcoal/NaOH exhaust system described above.

A.4 Run Parameters

The design of the HPCF was based on a nominal run condition of N_2 at 1 atm, with $U_0 = 60\,\mathrm{m/s}$ and $d_0 = 0.005\,\mathrm{m}$, resulting in a nominal Re of 20,000. The various components were then sized to provide run times sufficiently long to extract reliable statistics, *i.e.*, before recirculation of hot products contaminated the temperature measurements. To determine the statistical reliability of the average temperature measurement, a local large-scale passage time τ_δ can be estimated from Eq. 4.20. This estimate can be used to determine the number of local large-scale passage times sampled during a run at a particular x/d_0 location. At the nominal run conditions given above, for an estimated run time of 10 seconds, this corresponds to 59 τ_δ's at $x/d_0 = 240$.

The local large-scale passage time can be compared to the estimated response time of the cold wires τ_w to determine the minimum temporal resolution requirements. The response time of the wires can be estimated from an energy balance between an elemental length of wire and the gas flowing over the wire, neglecting conduction, radiation, and ohmic heating of the wire. The resulting response time is given by

$$\tau_w = \frac{{d_w}^2 \rho_w c_w}{4\,Nu\,k_g} \quad ,$$

where

d_w = cold wire diameter

ρ_w = cold wire density

c_w = specific heat of the cold wire

Nu = Nusselt number

k_g = thermal conductivity of gas.

Since $Nu \sim \sqrt{Re}$ (*e.g.*, Kramers 1946), the response time of the wire varies inversely with $\sqrt{Re}$.

Table A.3: Time scales for Re = 10,000 experiments, U_0 = 62.4 m/s, d_0 = 2.5 mm, ΔT_f = 6.9 K

x/d_0	U_{cl} (m/s)	τ_δ (msec)	τ_w (msec)	# τ_δ's sampled
29.8	12.98	2.52	5.83	1,984
34.0	11.38	3.29	6.16	1,520
39.4	9.81	4.41	6.56	1,134
46.2	8.37	6.07	7.01	823
52.4	7.38	7.81	7.39	640
68.4	5.66	13.30	8.23	376
80.2	4.82	18.30	8.76	273
91.0	4.25	23.55	9.20	212
104.8	3.69	31.23	9.72	160
120.0	3.22	40.94	10.23	122
138.6	2.79	54.62	10.79	91
159.0	2.43	71.88	11.35	70
183.2	2.11	95.43	11.94	52
208.4	1.86	123.48	12.49	40
240.2	1.61	164.04	13.11	30

After performing runs with a 5 mm exit diameter nozzle, it was apparent that the recirculation problem was worse than estimated and the only solution was to enlarge the HPRV or provide coflow to satisfy the entrainment requirements of the jet. Since neither of these could be simply implemented, the nozzle exit diameter was cut in half to essentially "shrink" the flow and make the HPRV effectively larger in the sense of increasing uncontaminated run times. This set the nominal run condition to N_2 at 1 atm with U_0 = 62.4 m/s and d_0 = 2.5 mm, resulting in a nominal Re of 10,000. With the pressure range of 0.1 atm to 15 atm, this gives a nominal Reynolds number range of $1000 < Re < 150,000$. The actual Reynolds numbers realized for the current experiments (at the nominal exit velocity and diameter) were $10,000 < Re < 150,000$. The lower limit was set by the F_2 passivation problem discussed in Sec. 4.3, while the upper limit was set by the pressure limitations of the facility.

The relevant times for the lowest Reynolds number runs are given in Table A.3.

The wire response times in Table A.3 are conservative because, as shown above, the frequency response of the wires increases with increasing Re. For this Reynolds number, the measurements should become time-resolved for $x/d_0 \geq 52.4$. However, since only mean quantities are required, the temporal resolution is adequate when compared to the number of τ_δ's sampled during a run to give an accurate average temperature measurement at all the x/d_0 positions. For the runs where U_0 was varied, similar calculations were made to confirm the statistical accuracy of the mean temperature measurement.

A.5 Run Procedures

Because of the hazardous nature of the gases used in the experiment, a lengthy set of written procedures are followed for each run, with two people always present. A typical run and cleanup operation requires most of a day. The run procedure is as follows:

1. Wire calibration
2. Evacuation of the HPRV, F_2 reactant tank, and mixing vessels
3. Loading of NO and N_2 into the HPRV to the designated run pressure
4. Loading of F_2 and N_2 into the F_2 reactant tank
5. Wait a period for the gases to homogenize
6. Perform the run with data acquisition
7. Unload the catch bag, HPRV, F_2 reactant tank, and mixing vessels.

APPENDIX B

Calibration and processing techniques

B.1 Cold wire calibration

In order to convert the voltage output of the cold wires into a temperature measurement, calibration is needed. One method is to immerse the wires in a gas of known temperature until equilibrium with the gas is achieved, record the voltage, then change the temperature of the gas and repeat the measurement. The conversion constants can then be computed assuming a linear relation between voltage and temperature.

The temperature change for the calibration is accomplished by an isentropic expansion of the gas inside the HPRV. The method is to overpressure the HPRV the night before a run, and let the gas come to thermal equilibrium overnight. Great care is taken to eliminate thermal gradients in the lab by running recirculating fans continuously. In the morning, the wire voltages are recorded on the computer during the entire calibration process that lasts about seven seconds. This involves beginning the data acquisition about one second before the expansion to obtain the voltage offsets, opening the Camflex valve (typically one second), and waiting about five more seconds for the HPRV to exhaust the gas to atmospheric pressure. In this way, all 18 cold wires are simultaneously exposed to a uniform temperature drop. The temperature drop is computed from the HPRV pressure trace assuming an isentropic expansion of the gas and the calibration constants are determined. Figure B.1 shows a sample calibration of the 18 cold wires. The calibration constants do not vary by more than 1% from day to day and are fairly constant even after many

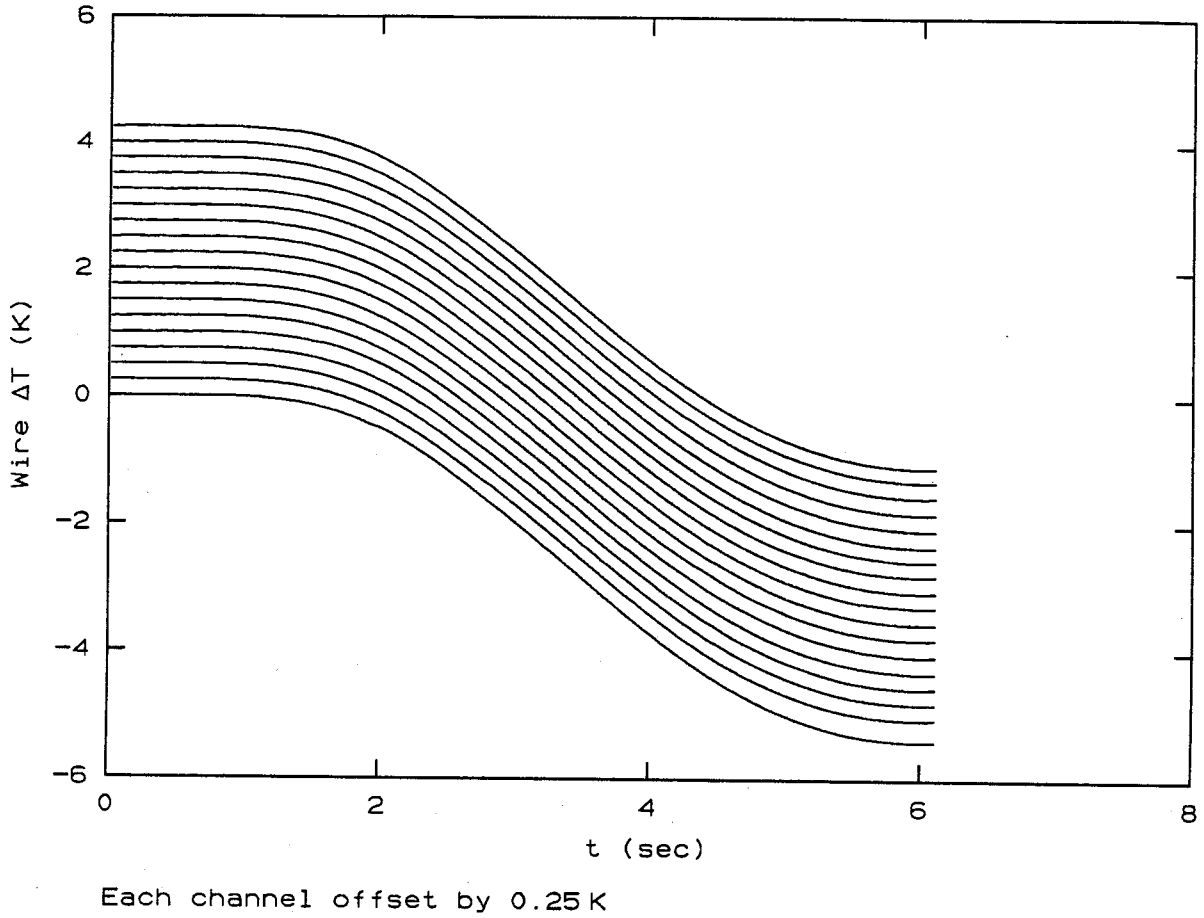

FIG. B.1 Sample cold wire traces from a calibration temperature drop. The lower trace is the reference cold wire at $x/d_0 = 0$, followed by the 16 cold wires from $x/d_0 = 30$ to 240, and finally, the other reference cold wire at $x/d_0 = 240$.

hot runs. Since the calibration is performed using a temperature drop and the wires measure temperature rises during a run, it was necessary to check for hysteresis. The temperature rise in the HPRV during a run is computed from the HPRV pressure trace assuming an isentropic compression and compared to the temperature rise recorded by the reference wire at $x/d_0 = 0$. The two measurements always show excellent agreement.

B.2 Processing techniques

Twenty channels of data were recorded during a run: the 16 cold wires, the two reference cold wires, the HPRV pressure, and the nozzle dynamic pressure.

After a run, the data are processed as follows. The data were transferred to the HYDRA VMS/VAX cluster for processing. A program calculated the jet and reservoir gas mixture properties based on Thompson (1984), and then passed a smoothing filter over the raw data to compress the record. The offset voltage of each channel was removed and the wire voltages were converted to temperature rises using the calibration constants just described. Using the gas mixture properties, the nozzle differential pressure was converted to velocity and the HPRV pressure rise was converted to a temperature rise assuming an isentropic compression.

The temperature rise from the 16 cold wires and two reference wires along with a scaled velocity trace were then plotted as in Fig. 3.2. A suitable averaging region was chosen, beginning at the time where the velocity had reached steady state and ending at the time when the recirculated hot products reached the reference wire at $x/d_0 = 240$. The average temperature rise of each wire was then computed and the average temperature in the HPRV, determined from the HPRV pressure trace, was subtracted from the wire temperatures. Then, the average wire temperatures were normalized by the adiabatic flame temperature rise. The nondimensional product thickness δ_P/L_w, defined by Eq. 3.5, along with the corresponding x/d_0, was written to a data file where the momentum diameter was implemented. The data were then plotted, as shown in Fig. B.2, for example. A least-squares fit was done in the ramp region and a cubic spline was fit to the knee region (the solid curve). The first derivative of the curve fit was then plotted and used to locate the maximum δ_P/L_w. Finally, a 99% of maximum δ_P/L_w was determined and used to define the flame lengths discussed in Ch. 4.

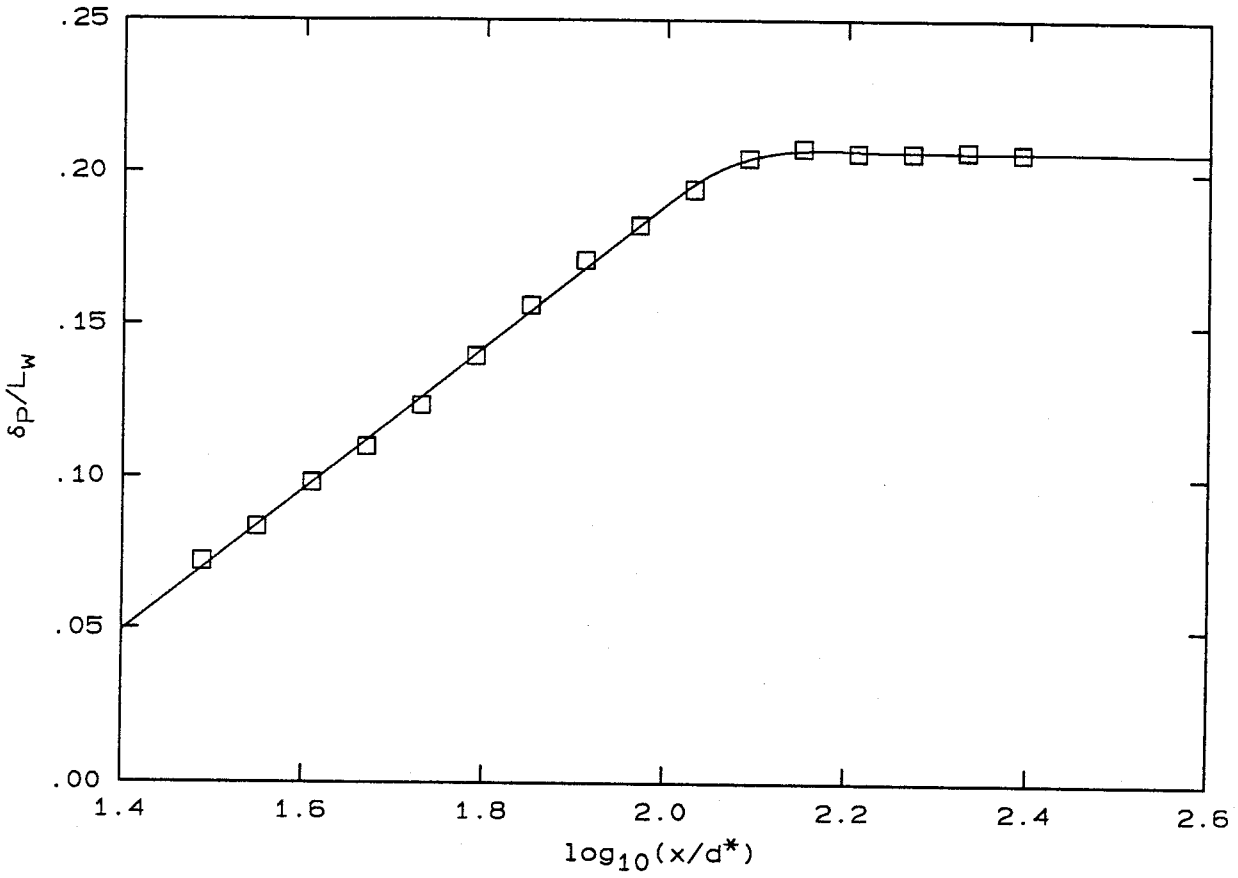

FIG. B.2 Sample plot of normalized product thickness versus $\log_{10}(x/d^*)$.

References

AVERY, J. F. and FAETH, G. M. [1974] "Combustion of a Submerged Gaseous Oxidizer Jet in a Liquid Metal," *15th Annual Combustion Institute*, 501–512.

BAULCH, D. L., DUXBURY, J., GRANT, S. J. and MONTAGUE, D. C. [1981] "Evaluated Kinetic Data for High Temperature Reactions," Vol. 4, *J. Phys. Chem. Ref. Data*, **Vol. 10, Suppl. 1**.

BECKER, H. A., HOTTEL, H. C. and WILLIAMS, G. C. [1967] "The nozzle-fluid concentration field of the round turbulent, free jet," *J. Fluid Mech.* **30**(2), 285-303.

BECKER, H. A. and LIANG, D. [1978] "Visible Lengths of Vertical Free Turbulent Diffusion Flames," *Comb. and Flame* **32**, 115–137.

BECKER, H. A. and YAMAZAKI, S. [1978] "Entrainment, Momentum and Temperature in Vertical Free Turbulent Difusion Flames," *Comb. and Flame* **33**, 123–149.

BIRCH, A. D., BROWN, D. R., DODSON, M. G. and THOMAS, J. R. [1978] "The turbulent concentration field of a methane jet," *J. Fluid Mech.* **88**(3), 431-449.

BREIDENTHAL, R. E. [1981] "Structure in turbulent mixing layers and wakes using a chemical reaction," *J. Fluid Mech.* **109**, 1–24.

BROADWELL, J. E. [1982] "A Model of Turbulent Diffusion Flames and Nitric Oxide Generation. Part I," TRW Document No. 38515-6001-UT-00, EERC Final Report, PO No. 18889.

CHEN, C. J. and RODI, W. [1980] *Vertical Turbulent Buoyant Jets. A Review of Experimental Data* (Pergammon Press, Oxford).

DAHM, W. J. A., DIMOTAKIS, P. E. and BROADWELL, J. E. [1984] "Non-Premixed Turbulent Jet Flames," AIAA 22nd Aerospace Sciences Meeting (Reno, Nevada), AIAA Paper No. 84-0369.

DAHM, W. J. A. and DIMOTAKIS. P. E. [1987] "Measurements of Entrainment and Mixing in Turbulent Jets," *AIAA J.* **25**(9), 1216–1223.

DAHM, W. J. A. and DIMOTAKIS, P. E. [1990] "Large Schmidt number mixing of a conserved scalar in the self-similar far field of turbulent jets," *J. Fluid Mech.* **217**, 299–330.

DELICHATSIOS, M. A. and ORLOFF, L. [1984] "Entrainment Measurements in Turbulent Buoyant Jet Flames and Implications for Modeling," 20^{th} Symposium (International) on Combustion (The Combustion Institute), 367–375.

DIMOTAKIS, P. E. and BROWN, G. L. [1976] "The mixing layer at high Reynolds number: large-structure dynamics and entrainment," *J. Fluid Mech.* **78**(3), 535–560 + 2 plates.

DIMOTAKIS, P. E. [1989] "Turbulent Free Shear Layer Mixing," *AIAA* 27^{th} *Aerospace Sciences Meeting*, 9–12 January 1989 (Reno, Nevada), AIAA–89–0262.

DOWLING, D. R. [1988] *Mixing in Gas Phase Turbulent Jets*, Ph.D. thesis, California Institute of Technology.

DOWLING, D. R. and DIMOTAKIS, P. E. [1990] "Similarity of the concentration field of gas-phase turbulent jets," *J. Fluid Mech.* **218**, 109.

FRIELER, C. E. and DIMOTAKIS, P. E. [1988] "Mixing and Reaction at Low Heat Release in the Non-Homogeneous Shear Layer," *First National Fluid Dynamics Congress*, 24–28 July 1988 (Cincinatti, Ohio), AIAA Paper 88–3626.

HALL, J. L. [1991] *An Experimental Investigation of Structure, Mixing and Combustion in Compressible Turbulent Shear Layers*, Ph.D. thesis, California Institute of Technology .

HAWTHORNE, W. R., WEDDELL, D. S. and HOTTEL, H. C. [1948] "Mixing and combustion in turbulent gas jets," *Third Symposium on Combustion, Flame and Explosion Phenomena*, 266–288.

HERMANSON, J. C. and DIMOTAKIS, P. E. [1989] "Effects of heat release in a turbulent reacting shear layer," *J. Fluid Mech.* **199**, 333–375.

HOTTEL, H. C. [1953] "Burning in Laminar and Turbulent Fuel Jets," 4^{th} (International) Symposium on Combustion (The Williams and Wilkins Co., 1953), 97–113.

KEE, R. J., MILLER, J. A. and JEFFERSON, T. H. [1980] "CHEMKIN: A General Purpose, Problem-independent, Transportable, Fortran Chemical Kinetics Code Package," SANDIA Report SAND80–8003.

KOOCHESFAHANI, M. M. and DIMOTAKIS, P. E. [1986] "Mixing and chemical reactions in a turbulent liquid mixing layer," *J. Fluid Mech.* **170**, 83–112.

KRAMERS, H. [1946] "Heat Transfer from Spheres to Flowing Media," *Physics* **12**, 61–80.

KUO, K. K. [1986] *Principles of Combustion* (John Wiley & Sons).

KUTHE, A. M. [1935] "Investigations of the turbulent mixing regions formed by jets," *J. Appl. Mech.*, Transactions of the ASME, **2**(3), 87–95.

LOCKWOOD, F. C. and MONEIB, H. A. [1980] "Fluctuating Temperature in a Heated Round Free Jet," *Combust. Sci. and Technol.* **22**, 63–81.

MILLER, P. L. and DIMOTAKIS, P. E. [1991] "Reynolds number dependence of scalar fluctuations in a high Schmidt number turbulent jet," *Phys. Fluids A* **3**(5), 1156–1163.

MUNGAL, M. G. [1983] *Experiments on Mixing and Combustion with Low Heat Release in a Turbulent Shear Flow*, Ph.D. thesis, California Institute of Technology.

MUNGAL, M. G. and DIMOTAKIS, P. E. [1984] "Mixing and combustion with low heat release in a turbulent mixing layer," *J. Fluid Mech.* **148**, 349-382.

MUNGAL, M. G, HERMANSON, J. C. and DIMOTAKIS, P. E. [1985] "Reynolds Number Effects on Mixing and Combustion in a Reacting Shear Layer," *AIAA J.* **23**(9), 1418–1423.

RICOU, F. P. and SPALDING, D. B. [1961] "Measurements of entrainment by axisymmetrical turbulent jets," *J. Fluid Mech.* **11**, 21–32.

RUDEN, P. [1933] "Turbulente Ausbreitungsvorgäenge im Freistrahl," Die Naturwissenschaften, Jahrg. **21**, Heft. 21/23, 375–378.

SANDBORN, V. A. [1972] *Resistance Temperature Transducers* (Metrology Press, Fort Collins, Colorado).

THOMPSON, P. A. [1984] *Compressible-Fluid Dynamics* (The Maple Press Company, 82-85, 642).

THRING, M. W. and NEWBY, M. P. [1953] "Combustion length of enclosed turbulent jet flames," 4^{th} (International) Symposium on Combustion (The Williams and Wilkins Co., 1953), p. 97.

TONER, S. J. [1987] *Entrainment, Chemistry, and Structure of Fire Plumes*, Ph.D. thesis, California Institute of Technology.

TOWNSEND, A. A. [1976] *The Structure of Turbulent Shear Flow* (2^{nd} edition, Cambridge University Press).

WHITE, F. M. [1974] *Viscous Fluid Flow* (McGraw-Hill Book Company, New York, p. 509).

WILSON, R. A. M. and DANCKWERTS, P. V. [1964] "Studies in turbulent mixing–II, A hot air jet," *Chem. Eng. Sci.* , **19**, 855–895.

WYGNANSKI, I. and FIEDLER, H. E. [1969] "Some measurements in the self-preserving jet," *J. Fluid Mech.* **38**, 577-612.

ZUKOSKI, E. E., CETEGEN, B. M. and KUBOTA, T. [1984] "Visible Structure of Buoyant Diffusion Flames," 20^{th} *International Symposium on Combustion* (The Combustion Institute), 361–366.